Physical Properties of Electric-Field-induced Conductive state in Nanotube Networks

Hideki Kawai
2017

Contents

1 Introduction

Quantum confinements of electrons in low dimensional structures induce unique physical phenomena, which cannot be observed in conventional bulk materials, such as ballistic transport[1], Coulomb blockade[2] and size-dependent excitonic phenomena[3]. Especially, in one-dimensional materials, physical properties are significantly changed depending on a position of Fermi level due to presence of Van-Hove singularities in density of states. Since 1960s Two-dimensional (quantum wells)[4,5] and Zero-dimensional system (quantum dots)[6] have been extensively studied thank to progresses of fabrication techniques such as molecular beam epitaxy. Regarding one-dimensional materials, conducting polymer, one-dimensionally stacked organic molecules, in-organic chain systems have provided us a field to investigate physical properties of one-dimensional systems, and such materials have been intensively studied since 1970s[7-9]. However, such polymers are often structurally and chemically deformed because of their easiness structural deformation, in-homogeneity and reactivity of edge parts such as termination chemical groups, and that induces uncertainties of boundary conditions to the transverse direction of one-dimensional axis.

On the other hand, in 1991, Iijima has discovered multi-walled carbon nanotubes.[10] Two years later, he found single-walled nanotubes(SWCNTs).[11] At the same time, Tenne et al. have reported synthesis of multi-walled tungsten disulfide nanotubes (WS_2 NTs).[12] SWCNTs and WS_2 NTs are cylindrical materials rolling up two-dimensional graphene and tungsten disulfide sheets. Those nanotubes have high aspect ratio, exhibit excellent mechanical strength[13-15] and possess a chemical stability due to the closed shell structure without any dangling bond. A remarkable point is that cylindrical structure completely define quantum confinement conditions to the direction normal to the axes [16,17], which cannot be possible in cases of other open edge structure materials, and such quantized conditions induce discrete energy states of electrons, thus nanotube systems provide unique electronic structures with motion of the electrons along the axis of nanotubes. In addition, structure of the nanotubes is assigned by chiral index, which determine how to roll up the two-dimensional sheet and define the electronic structure of nanotubes.[16] SWCNTs are known to exhibit metallic and semiconducting properties depending on the chiral index. On the other hands, WS_2 NTs always exhibit semiconducting properties regardless of the chiral

index. Those discoveries of nanotubes give us great opportunities to investigate physical properties of unique one-dimensional systems.

From 1990s to 2000s, many researchers have reported their unique and superior properties of SWCNTs in a single rope state, which originates from their one-dimensional nature.[18-21] On the other hands, practical applications require macroscopic networks of the nanotubes. Thus, fundamental understanding of physical properties of such macroscopic networks is important for practical applications. However, in such networks, there is in-homogeneity in chiralities and alignments of SWCNTs, which prevents quantitative understanding of physical properties and also degrades device performance. For example, in produced SWCNT sample, electrical and thermoelectric properties of SWCNT networks are those averaged among the chirality distributions including metallic and semiconducting types of SWCNTs. This mixture states degrade electrical and thermoelectric performance of SWCNT networks. Therefore, fabrication of networks of nanotubes in a single chirality state is important for fundamental understanding of nanotubes as well as practical application. In addition, carrier transport properties significantly depend on alignment of nanotubes in networks. It is well-known that electrical properties in the nanotube networks are dominated by the condition of tube-tube junctions.[22-26] For example, in conventional SWCNT networks, reported values of carrier mobility are significantly lower than that of a single rope sample, because carriers in the nanotube networks are localized at the tube-tube junction[24,27], thus transport mechanisms in such networks are different from those in single rope states. In order to improve contact properties between the tubes and to realize electronic devices with superior performances, control of alignment in nanotube networks is crucial.

In this context, fabrication of single crystalline SWCNTs where single chirality SWCNTs are densely and periodically well aligned is desired. However, although more than 20 years has passed since discovery of SWCNTs, fabrication of single crystalline SWCNTs has not been reported. As a result, several important basic physical properties of SWCNTs have been still un-veiled yet. For example, determination of lattice constant of single crystalline SWCNTs by X-ray diffraction has not been reported. As a result, calculations of band structure using rigorous lattice constant of SWCNTs has not been done. Superconductivity of SWCNTs in a bulk form has not been reported, and reported superconductivity is limited to the case of single bundle or composite.[28-30] In addition, reported superconducting transition temperatures have

large variation due to distribution of diameter and chirality of SWCNTs in their samples. Therefore, conditions for superconductivity of SWCNTs are still unclear. Single crystalline SWCNTs with uniform diameter and chirality is important to understand superconductivity of SWCNTs. Single crystalline SWCNTs is also required to fabricate electronic devices with excellent performance. In conventional SWCNT networks, reported values of carrier mobility are significantly lower than that of single rope sample due to tube-tube junction[24,27]. In the case of single crystalline SWCNTs, carriers can move without scattering at tube-tube junctions. Therefore, development of technique to fabricate single crystalline SWCNTs is important issue for basic science and practical applications.

In addition to importance of single crystalline SWCNTs, tuning a position of Fermi level is crucial to understand physical properties in one-dimensional materials. In one-dimensional system, it is well-known that carrier transport properties significantly depend on a position of Fermi level due to presence of Van-Hove singularities in density of states. Especially, electrical conductance and thermoelectric properties are significantly enhanced when Fermi level is near Van-Hove singularities.[31-33] Therefore, precise tuning of a position of Fermi level is crucial to precisely understand electrical and thermoelectric properties of nanotubes.

In this dissertation, in chapter 2, for the first step toward realization of single crystalline SWCNTs, I developed a new technique to fabricate aligned assembly where single chirality SWCNTs are highly and densely aligned. I investigated electronic properties of the assembly using electrolyte-gating technique. Transfer characteristics of the assembly showed that carrier mobility of the assembly was higher than that of random networks. On the other hands, temperature dependence resistance measurement indicated that although SWCNTs are highly aligned in the assembly, transport mechanism in the assembly was similar to that in random networks. I discussed the background of the improvement of carrier mobility and result of temperature dependence resistance measurement.

In chapter 2, I investigated electronic properties of aligned assembly of SWCNTs by shifting Fermi level toward valence and conduction band using electrolyte-gating technique. Fermi level tuning technique is also crucial for understanding thermoelectric properties of one-dimensional materials. It is known that thermoelectric properties are significantly enhanced when a position of Fermi level

reached to Van-Hove singularities in density of states. SWCNTs are ideal candidate for one dimensional material and SWCNTs are expected as excellent thermoelectric material. However, previous reports on thermoelectric properties of SWCNTs were mainly in a mixed chirality sample where both semiconducting and metallic type of SWCNTs are contained. In addition, relationships between thermoelectric properties and a position of Fermi level are not fully understood. Therefore, in chapter 3, I investigated relationships between thermoelectric properties of semiconducting, metallic SWCNTs and a position of Fermi level using electrolyte-gating technique. I found that thermoelectric properties depend on the amount of injected carriers. In addition, I found that thermoelectric power factor is optimized by tuning a position of Fermi level. However, the line-shape of Seebeck coefficients indicated that there are residual metallic SWCNTs or semiconducting SWCNTs with different charge neutral points and the presence of those nanotubes could degrade thermoelectric performance of SWCNTs. Therefore, I focused on WS_2 NTs because they always exhibit semiconducting properties regardless of their chirality and have wide band gap (~2 eV). In addition, they can form macroscopic networks due to their relatively strong Van der Waals force. However, there is no report on electronic properties of WS_2 NTs networks as well as thermoelectric properties. Therefore, I investigated electronic properties and thermoelectric properties of WS_2 NT networks using electrolyte-gating technique. I realized N-type and P-type conducting states in WS_2 NT networks, which is difficult to realize using conventional back-gating techniques. I measured thermoelectric properties of WS_2 NTs in the conductive states. I found that thermoelectric properties of WS_2 NTs depend on the amount of injected carriers. I succeeded to interpret the behavior of thermoelectric properties of SWCNTs and WS_2 NTs using simple theoretical models. Finally, I compared thermoelectric properties of SWCNTs and WS_2 NTs with other bulk materials.

Details of history and background of my study regarding fabrication of single crystalline SWCNTs and thermoelectric properties of nanotubes are written in Sec 1.1 and Sec 1.2, respectively.

1.1 Fabrication of single crystalline SWCNTs

SWCNTs are discovered in 1993.[11] SWCNTs have attracted a great interest due to unique physical properties. Electronic structure of SWCNTs depends on their chirality, which determines how a graphene layer is rolled up into a cylinder.[16] For example,

SWCNTs exhibit semiconducting and metallic properties depending on their chirality.[16] Especially, in the early 2000s, ballistic transport have been observed for individual metallic and semiconducting SWCNTs[19-21], which exhibited near room temperature quantum conductance and high current-carrying capability.

In addition to such intrinsic electrical properties, SWCNTs have relatively strong Van der Waals interaction, so that they tend to form bundle and networks[34,35]. This characteristic is advantageous for practical applications because of good scalability of the networks. However, the mixture state of chiralities in conventional SWCNT networks is a bottle-neck for device performance as well as basic understanding of physical properties. For example, conventional field effect transistor using networks of as-grown SWCNTs, which means the samples without further purification, as a channel could not exhibit good performance due to presence of metallic SWCNTs.[36,37] SWCNTs sample with narrow distribution of diameter was also required for structural analysis by X-ray diffraction.[38] These issues motivated many researchers for fabrication of single chirality SWCNTs.

In early 2000s, structure-selective growth of SWCNTs using specific catalyst has been reported.[39] Recently, chemical vapor deposition growth of SWCNTs with a specific chirality in an abundance over 92 percent have been reported.[40] On the other hands, in middle 2000s, high purity chirality separation in liquid phase has been reported. For example, density gradient centrifugations[41,42] and gel chromatography techniques[43,44] have been reported for semiconducting-metallic SWCNTs sorting and single-chirality SWCNTs extraction. The techniques enable us to prepare a film of SWCNTs with high purity of semiconducting or metallic SWCNTs. From the late 2000s to early in the 2010s, electrical properties of a film of separated SWCNTs have been reported. However, electronic properties of a film are quite different from the case of single rope state. For example, thin film transistor using separated SWCNTs have been reported[41,45-47] and the device performance was superior to conventional polycrystalline Si,[47] but carrier mobility of the film was much lower than single rope state. The degradation of carrier mobility comes from scattering of carriers at CNT-CNT junctions. For example, Yanagi et al. has reported that transport mechanism of carriers in SWCNT networks can be interpreted as Variable range hopping and weak localization for semiconducting and metallic SWCNTs film, respectively, which indicate scattering centers at the tube-tube junctions.[48]

To overcome this issue, single crystalline SWCNTs where single chirality SWCNTs

are densely and periodically well aligned is desired in this research community. One of strong method to fabricate single crystalline SWCNTs is vapor phase epitaxy. Many researcher have reported a fabrication of aligned array of SWCNTs by chemical vapor deposition utilizing specific substrate.[36,37,49] However, synthesized array contain various chiralities of SWCNTs. Therefore, it is difficult to fabricate single crystalline SWCNTs with single chirality SWCNTs using chemical vapor deposition.

Another approach is crystallization. For example, fullerene can be dissolved in organic solvent and we can prepare their single crystals. On the other hands, SWCNTs can be dissolved in solution using surfactants. Adsorption of surfactants on the surface of SWCNTs depends on their chirality and we can extract high purity single chirality SWCNTs by gel chromatography utilizing this dependency. Single chirality SWCNTs is crucial to fabricate single crystalline SWCNTs. However, in a situation where surfactants are surrounding SWCNTs, crystallization in liquid phase is difficult. Some groups have reported fabrication of aligned array of SWCNTs including our studies. However, degree of alignment in reported data was not sufficient. Therefore, development of a new technique to fabricate an aligned array of single chirality SWCNTs is crucial for fabrication of crystalline SWCNTs.

Single crystalline SWCNTs is also important for understanding of superconductivity of SWCNTs. In middle 2000s, superconductivity of carbon materials have attracted much attentions due to discovery of superconductivity in B-doped diamond[50], Ca-intercalated graphite[51] and Cs doped fullerene[52] with high transition temperature. In the case of SWCNTs, in the early 2000s, superconducting transition in resistance of single SWCNT bundle has been reported.[28,29,53] Lortza et al has reported superconductivity of CNT-zeolite composite.[30] However, experimental reports are limited to the case of single bundle or composite where the sample has diameter and chirality distribution. Theoretical work has showed that strength of electron-phonon coupling depends on diameter of SWCNTs[54-56], thus transition temperature may also depends on diameter. In addition, it has been reported that misalignment of lattices between neighboring SWCNTs leads difficulty of conserving momentum for an electron hopping from one nanotube to the other.[57] Therefore, alignment between neighboring SWCNTs and narrow chirality distribution, especially, single chiral state is expected to be crucial for realization of superconductivity in macroscopic scale. In addition, according to BCS theory transition temperature increases as density of states at Fermi level increases. It is known that carrier doping is also crucial for realizing high-T_c

superconductivity in any materials. For example, Ca-intercalated graphite[51], Cs doped fullerene[52] and B-doped diamond[50] have been reported. In the case of SWCNTs tuning the Fermi level to Van-Hove singularities can lead to high transition temperature due to the presence of an extremely large density of states.[55,58-60] Therefore, tuning of Fermi level of SWCNTs would be also crucial for realization of superconductivity. Superconductivity in SWCNTs is still under discussion. Realization of alignment of SWCNTs with a single chirality state and Fermi level tuning of the aligned system will give a new insight to discussions of superconductivity in SWCNTs.

In chapter2, our purpose is, as a first step for fabrication of single crystalline SWCNTs, development of technique to fabricate aligned array of single chirality SWCNTs and investigate its electronic properties. First, we developed a technique to produce assembly where individual SWCNTs are highly aligned to specific direction. The alignment of SWCNTs in the assembly was optically characterized. Electrical transport properties of the assembly and random network sample were compared. Finally, we measured temperature dependence resistance of the assembly under carrier injected state.

1.2 Thermoelectric properties of nanotube networks

Thermoelectric devices attract a lot of attentions because they can convert waste heat to electrical power. The conversion efficiency of a thermoelectric generator or cooler is directly related to the dimensionless materials figure of merit *ZT*.

$$ZT = \frac{S^2 \sigma T}{\kappa} \qquad (1.1)$$

Where T is the temperature, S is the Seebeck coefficient or themopower, σ is the electrical conductivity, and κ is the thermal conductivity (which includes both the electronic and lattice contribution). The *ZT* values have been used to characterize the thermoelectric performance of materials. Over the following 3 decades, 1960-1990, only incremental gains were achieved for increasing *ZT*, and finally the $(Bi_{1-x}Sb_x)_2(Se_{1-y}Te_y)_3$ alloy family was the one of the best commercial materials, with $ZT \approx 1$. Thermoelectric industry has been limited to niche applications such as power generator in space mission, generator on human body, compact cooler, where cost and

energy efficiency are not as important as energy availability.

A difficulty for enhancement of the efficiency is presence of trade off of the parameters in ZT. In order to enhance ZT, a large S value, a large σ, and a small κ are needed. However, these materials parameters are in a trade-off each other. For example, increase of the S for simple materials also leads to simultaneous decrease of σ. Also increase in σ leads to increase of κ because of the Wiedemann-Franz law. In 1990s, to overcome this limitation, a new direction of researches appeared on the basis of two ideas in thermoelectric materials.

The one is to introduce effective phonon-scattering centers to bulk materials, which is the so-called phonon-galass/electron-crystal materials such as the partially filled skutterudites based on alloys of $CoSb_3$. In recent years, ZT in this approach is reaching 1.7 at 800 K.[61] The other is to use low-dimensional materials systems. The strategy of this approach is to utilize quantum confinement effects to enhance of S and control S and σ independently, and to utilize surface scatterings to scatter phonons more effectively than electrons. For example, in the early 2000s, quantum-dot super-lattice composed of PbSe and PbTe layers achieved both increase the power factor and to decrease the thermal conductivity at the same time, and exhibited $ZT \approx 1.6$ and 3.5 at 300 K and 570 K, respectively.[62] This system is suitable for thin film thermoelectric cooling devices and may be utilized in future.

In 1993, Hicks and Dresselhaus have proposed that one-dimensional conductor can exhibit large ZT value due to quantum confinement effect and surface scattering effect.[63] Their calculation showed that quantum wire with diameter of 1 nm exhibits $ZT \approx 6$ at optimal chemical potential.[63] In 2008, it has been experimentally reported that Si nanowire with diameter of approximately 10-20 nm exhibit $ZT \approx 1$ at 200 K[64], which is two order of magnitude higher than that of their bulk form. Therefore, one-dimensional systems such as nanowire or nanotube are promising candidates for high-performance thermoelectric materials.

SWCNTs are well known as one-dimensional conductor. Especially, it has been expected that Van-Hove singularity peaks in their density of states significantly enhance their thermoelectric performance. In the case of metallic type solids, Seebeck coefficient can be approximately expressed as $S \propto g(E_F)/n$, where E_F is the Fermi level and n is carrier density given by the integral under the $g(E)$ curve from $E = 0$ to $E = E_F$.[65]

The sharper a function of energy $g(E)$ is, the higher the ratio $g(E_F)/n$, provided that E_F falls near a maximum in $g(E)$. It leads to a strong enhancement in Seebeck coefficient as well as ZT. Therefore, SWCNTs has attracted many attention for high performance thermoelectric materials in recent years.[31,32,66-68] In 2000s, thermoelectric properties of SWCNTs have been reported mainly for mat samples.[69-72] The mat samples have chirality distribution, thus the thermoelectric properties are those averaged over various chiralities of SWCNTs in the sample, such as semiconducting and metallic SWCNTs.

Thermoelectric properties of SWCNTs is expected to depends on their chirality.[31,32] In addition, Seebeck coefficients of SWCNTs are sensitive to a position of Fermi level near Van-Hove singularity peaks.[31,32] However, relationships between thermoelectric properties, their chirality, and a position of Fermi level of the SWCNTs have not been well understood.

In 2014, I investigated thermoelectric properties of high purity semiconducting SWCNT networks as a function of carrier concentration using electrolyte gating technique.[73,74] In the electrolyte gating technique electric double layer forms on the surface of materials, which behave as capacitor with thickness of approximately 1 nm.[75,76] The capacitor can accumulate carriers with concentration of 10^{14} cm^{-2} and one can continuously control the carrier concentration by changing applied voltage.[75,76] In addition, the electric double layer can form on the whole surface of all nanotubes, thus one can control Fermi level of all nanotubes consisting of macroscopic nanotube networks. Using this technique I revealed the relationship between thermoelectric properties of SWCNT networks and a position of Fermi level.[73,74] I found that thermoelectric properties significantly depends on Fermi level. I also found that power factor becomes maximum when Fermi level is tuned. However, behavior of Seebeck coefficients is not consistent with theoretical calculation. The results indicated that although we prepared high purity semiconducting SWCNTs, there is possibility of degradation of thermoelectric performance due to presence of residual metallic SWCNTs or semiconducting SWCNTs with different charge neutral positions. Therefore, I focused on WS_2 NTs as another nanotube.

WS_2 NTs are cylindrical nanotubes with a rolled structure consisting of two-dimensional WS_2 sheet.[12] WS_2 NTs always exhibit semiconducting characteristics regardless of how their sheet is rolled. In addition, it has been showed by calculation

that thermoelectric properties of WS_2 NTs is enhanced due to presence of Van-Hove sigularity.[66] WS_2 NTs has no dangling bond, which is advantageous for Fermi level tuning by electric field as in the case of SWCNTs. However there are no previous reports on thermoelectric properties, much less electronic properties of WS_2 NT networks. The lacking comes from difficulty in electrical measurements due to insulating nature of WS_2 NT networks in non-doped state. In the WS_2 NT networks, making conducting pass between electrodes using conventional back gating field effect transistor configuration was difficult. However, in 2016, I found that conductive state in WS_2 NT networks can be realized using electrolyte-gating technique.[77] Electrolyte gating field effect transistor using WS_2 NT networks as a channel exhibited good field effect mobility, which is comparable to that of conventional polycrystalline silicon device.[77] In addition, I found that thermoelectric measurement of WS_2 NT networks can be performed in the conductive state using electrolyte-gating technique.[78] Power factor of the WS_2 NT networks in the conductive state was comparable to single crystalline WS_2.[78] The results indicate that electrolyte-gating technique can make WS_2 NT networks good candidate for electronics and thermoelectronic applications.

The purpose in chapter 3 is to reveal relationships between thermoelectric properties of nanotube networks and a position of Fermi level. First, we introduce thermoelectric measurement of semiconducting SWCNTs using electrolyte-gating technique. I found that thermoelectric properties of SWCNTs depend on the amount of injected careers, and that power factor became maximum when Fermi level was tuned. However, the behavior of Seebeck coefficients was not consistent with theoretical calculations, which indicated presence of residual metallic SWCNTs or semiconducting SWCNTs with different charge neutral positions. Those unexpected SWCNTs may degrade thermoelectric performance of SWCNTs. Second, as another one-dimensional material, I investigated thermoelectric properties of WS_2 NTs. I discussed the effectiveness of electrolyte-gating technique for thermoelectric measurement of WS_2 NT networks by comparing with conventional back-gating technique. Finally, I discussed differences between thermoelectric properties of SWCNTs and WS_2 NTs, and their potentials as thermoelectric devices by comparing other bulk materials.

2 Fabrication of aligned assembly of SWCNTs in single-chiral state and its electronic propertes

2.1 Introduction

Formation of a well-ordered structure is an important requirement for anisotropic nano-materials, such as liquid crystals[79] and gold nano-rods[80], to ensure their optimal performance in devices. SWCNTs are one-dimensional materials with diameters of approximately 1 nm. They have intrinsically high mobility[19,20] and mechanical flexibility[81-83], and they have been utilized in various electronic applications, such as flexible electronics[84-88], electrochromic devices[89], and thermoelectric devices.[73,74,90] Additionally, arrays in which SWCNTs are highly aligned are used in electronics. Such arrays are produced on substrates by chemical vapor deposition processes.[36,37,49] However, the individual SWCNTs within the arrays have different diameters and electrical structures. Such variability prevents the direct use of the as-grown samples without additional purification processes.[91,92] For example, in transistor applications, it is crucial to remove metallic SWCNTs. Therefore, in such synthesis approaches, it is very difficult to prepare an aligned array of SWCNTs with a single-chiral state.

Recently, various purification techniques for SWCNTs have enabled us to prepare high-purity metallic, semiconducting SWCNTs or SWCNTs with single chiral states.[41-44,93-]In these purification processes, the SWCNTs were mono dispersed with surfactants[41-44] and DNA[93-95], and the SWCNTs with different electronic structures are differentiated during centrifugation and chromatography processes. Many devices fabricated using such purified SWCNTs have been reported; however, purified SWCNTs are often used in their random networks, in which the SWCNTs are randomly oriented and distributed during network formation from the mono-dispersed states.[84-87,96] In such situations, the tube-tube contact functions as a scattering center, and induces the localization of conducting carriers.[27,48] Therefore, development of techniques to produce assemblies in which the purified SWCNTs are highly aligned has been an important goal for the realization of high-performance transistors as well as basic science. Several studies have reported aligned arrays of purified SWCNTs utilizing external field[97-100],spin-coating[101], liquid-air interfaces[102,103,], surface modifications of the substrate[104,105], hydrophobic film[106], the coffee ring phenomenon[45].

We have reported self-assembled string-like assembly produced via temperature control of SWCNTs solution.[107] However, in our technique, relatively high temperature process may suppress degree of alignment of the string-like assembly.

Purpose in this chapter is to fabricate aligned array of SWCNTs and investigate its electronic properties. First, we developed technique for preparing one-dimensional assemblies of SWCNTs in which the SWCNTs are highly and densely aligned. The assemblies were produced using surfactant crystals as templates upon which the SWCNTs were self-assembled. To characterize the alignment of SWCNTs in the assembly we performed polarized Raman measurement and scanning electron microscopy measurement. We also discussed mechanisms of the self assembled process in this technique. Second, to compare the electrical properties of the assembly and random networks, we performed transfer characteristics measurements and capacitance measurements. Field effect mobility of the SWCNTs assembly are evaluated and compared with that of random SWCNT networks. Effective carrier density and effective carrier mobility are key parameter to understand electronic properties of material, thus we tried to measure a carrier density of SWCNT networks under carrier injected state by Hall effect measurement. Third, we performed 4-turminal resistance measurement of the metallic, semiconducting, and (6,5) enriched SWCNT thin film to understand how carrier injection using electrolyte-gating technique affects transport mechanism of SWCNT networks. We found that all of the SWCNTs networks exhibit variable range hopping conduction. Especially, increase of resistance at low temperature in metallic SWCNTs film was the most suppressed in the all type of the SWCNT film. Finally, we performed resistance measurements of metallic SWCNTs assembly. Temperature dependence of the resistance of the assembly was analyzed using variable range hopping model. Parameters of VRH model in the assembly were compared with that of random SWCNT networks.

2.2 Crystal template method

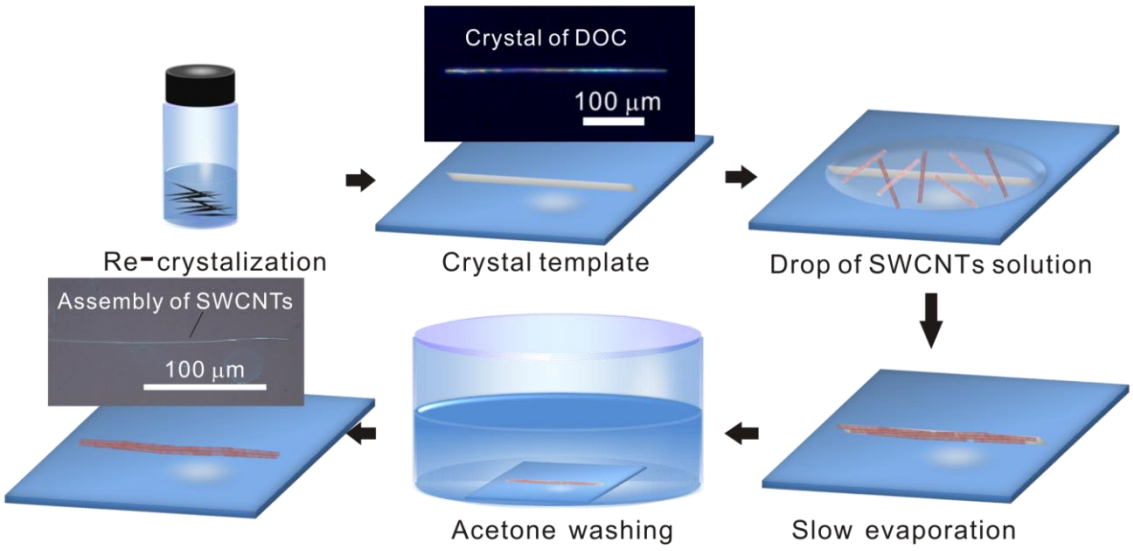

Fig. 2.1 Schematic of the crystal template method.
(Copyright 2014 AIP Publishing LLC)

Fig. 2.1 shows a schematic of the procedures used in our technique. First, we prepared high-purity semiconducting, metallic SWCNTs with diameter of 1.4 nm and (6,5) SWCNTs by density gradient filtration methods[41,42] and gel chromatography[43,44], respectively. Details of density gradient filtration methods and gel chromatography are written in section 5.2.1 and 5.2.2, respectively. Optical absorption spectrum and Raman spectrum of chirality-sorted SWCNTs are written in sec 5.2.4. The suspended surfactants were exchanged with 1 % (w/w) sodium deoxycholate (DOC, Wako Co.). Then, we prepared the needle-like crystals of DOC by re-crystallization (Details are written in section 5.6.1). The needle-like crystals of DOC, which were 100 μm to 1 mm in length and 1 μm to 2 μm in width, were placed on a substrate (SiO_2 (100 nm)/Si), and the liquid of the purified SWCNTs solution was dispensed onto the crystal at 15 - 20 °C. Subsequently, the SWCNTs self-assembled upon the surface of the crystals during the evaporation of the solvents as shown in Fig. 2.1. After the evaporation step, the surfactant crystal was removed by soaking it in an acetone solution for 1 – 3 days, leaving only the needle-like assembly in which the SWCNTs were highly and densely aligned on the substrates (see Fig. 2.1). Additional details of procedure and confirmation of removal the surfactants are shown in section 5.6.2. and 5.6.3., respectively.

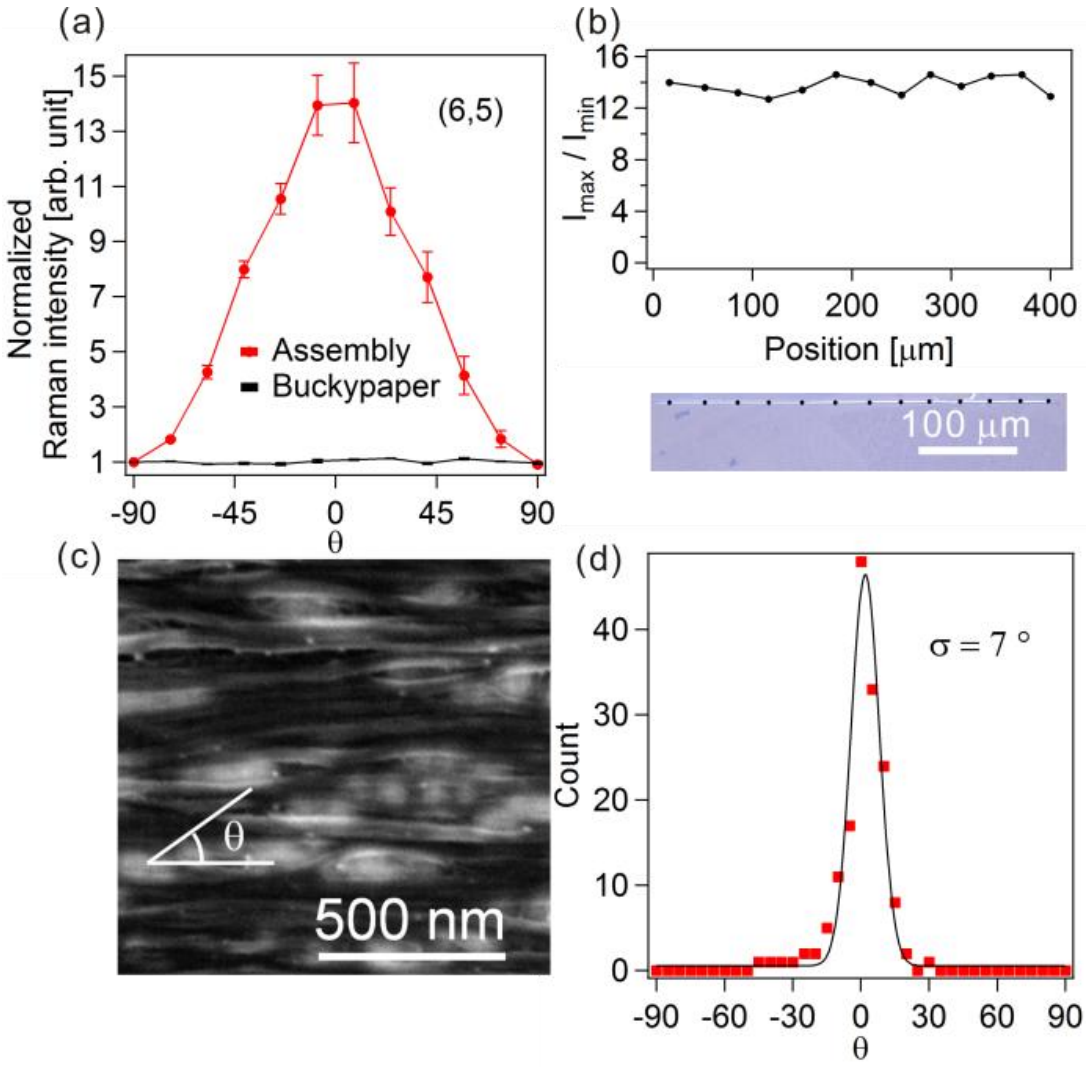

Fig. 2.2 (a) The normalized G-band intensities as a function of the angle θ between the axis of crystal template and the polarization vector of the incident laser light are shown. The red line represents the assembly made from (6,5) SWCNTs via the crystal template method; The black line is a buckypaper film composed of SWCNTs. (b) Distribution of the I_{max} /I_{min} value in the whole area of the assembly. (c) Scanning electron microscopy image of the assembly of aligned (6,5) SWCNTs. (d) Distribution of the SWCNT bundle orientations obtained from Fig. 2.2 (c). (Copyright 2014 AIP Publishing LLC)

First, we discuss the characteristics of the needle-like assembly of (6,5) SWCNTs, which was purified using a gel chromatography method from CoMoCAT samples (Aldrich Co.). The alignment ratio of the assembly of SWCNTs obtained through the above procedure was determined by polarized Raman microscopy as shown in Fig. 2.2.

Raman spectra were measured with an excitation wavelength of 561.3 nm, and the laser spot had a diameter of ~1 μm, which is smaller than the width of the assembly. Fig. 2.2 (a) shows the normalized G-band intensity of the assembly of (6,5) SWCNTs as a function of angle θ between the polarization direction of the incident laser light and the main axis of the assembly (Raman spectrum of the assembly are shown in sec 5.6.4). As a reference, the polarization dependence in random networks (such as buckypaper of SWCNTs) is also shown. The intensity of the G-band in the assembly reached the maximum intensity (I_{max}) when the polarization of the incident radiation was parallel to the axis (θ = 0 °) and reached the minimum intensity (I_{min}) when the polarization was normal to the axis. This behavior was fully reproducible in the same location. The I_{max} /I_{min} was approximately 14 and corresponding nematic order parameter[108] was 0.81, which are higher than those of previously reported aligned arrays of SWCNTs[103,109], including our previous work.[107] This result clearly indicates that the SWCNTs were highly aligned along the axis of the assembly.

We also investigated the distribution of alignment of SWCNTs within the assembly. Fig. 2.2 (b) shows a micrograph of the assembly with a length of approximately 400 μm and the I_{max} /I_{min} measured at intervals of approximately 30 μm on the assembly. The distribution of the I_{max} /I_{min} value ranged from 12 to 16, indicating that the SWCNTs were uniformly aligned. We estimated the angle distribution σ of the SWCNTs in the assembly from the following equation:

$$\frac{I_{max}}{I_{min}} = \frac{\int_{-\frac{\pi}{2}}^{\frac{\pi}{2}} (I^s_{max}\cos^2\theta + I^s_{min}\sin^2\theta)\exp\left\{-(\frac{\theta}{2\sigma})^2\right\}d\theta}{\int_{-\frac{\pi}{2}}^{\frac{\pi}{2}} (I^s_{max}\sin^2\theta + I^s_{min}\cos^2\theta)\exp\left\{-(\frac{\theta}{2\sigma})^2\right\}d\theta} \qquad (2.1)$$

Here, I^s_{max} and I^s_{min} are the maximum and minimum values in a single rope of SWCNTs. When we use the reported ideal I^s_{max} / I^s_{min} value from 20 and 10 in a single rope or bundle of SWCNTs[49,110], the standard deviation, σ, which corresponds to the angle-distribution of SWCNTs from the axis of the assembly, was estimated to be from complete alignment to 7 ° - 10 °. The results indicate that approximately 70 % of the SWCNTs were aligned parallel to the axis of the assembly within 7 ° - 10 °.

To further investigate the structural information of the SWCNTs within the assembly, we performed scanning electron microscopy (SEM) measurements. Fig. 2.2 (c) is an SEM image of an assembly of (6,5) SWCNTs, indicating that the SWCNTs

were highly and densely aligned. From the SEM image, we estimated the angle distribution of SWCNT bundles as shown in Fig. 2.2 (d). Here, the angles between the directions of each bundle and the axis of the assembly, which were estimated from depicting several straight lines along the observed bundles, were evaluated and counted. The σ value was evaluated to be approximately 7 ° as shown in the figure, which is in agreement with the results of polarized Raman microscopy.

A crystal template method is applicable for other SWCNTs samples. For examples (Fig. 2.3), we succeeded to prepare aligned assemblies of semiconducting and metallic SWCNTs with average diameters of 1.4 nm, which were purified through typical density-gradient centrifugation processes from SWCNTs samples produced by the Arc discharge method (Arc SO, Meijo nano CO.). Polarized Raman microscopy measurements and SEM images are shown in Fig. 2.3. The I_{max}/I_{min} values of both assemblies were approximately 13 (mean value of I_{max}/I_{min} was 10, see section 5.6.5), the SEM images clearly show that densely aligned SWCNT bundles were formed in both samples. These results indicate that our crystal template method can be applicable to various types of SWCNTs.

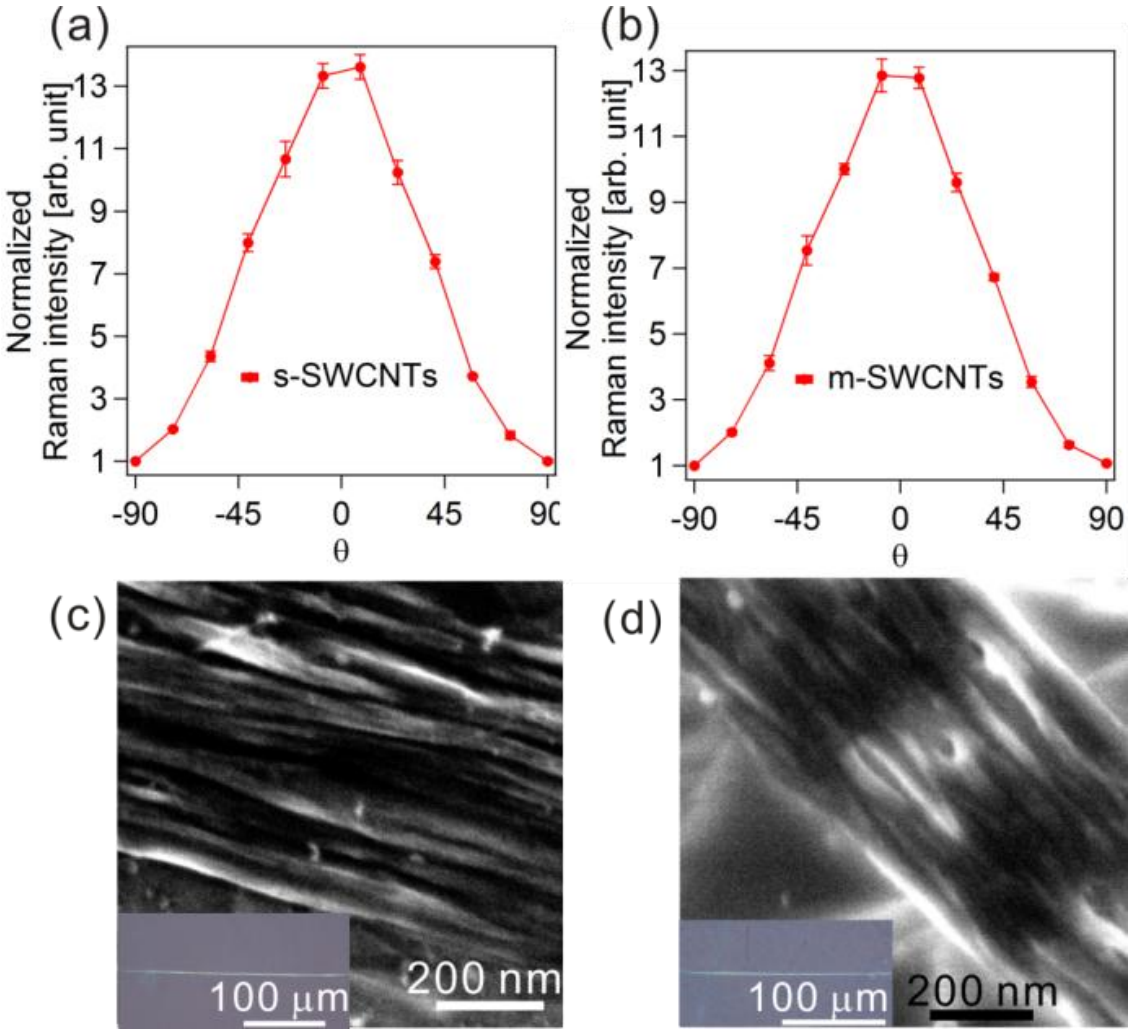

Fig. 2.3 Polarized Raman microscopy measurements and scanning electron microscopy images of the assembly are shown. (a) and (c) are semiconducting SWCNTs (s-SWCNTs); (b) and (d) are metallic SWCNTs (m-SWCNTs) with diameters of 1.4 nm. (Copyright 2014 AIP Publishing LLC)

Finally we briefly discuss probable mechanisms for the self-assembled processes in this technique. As shown in the result of Scanning Auger Mapping (Fig. 5.24 in section 5.6.3), Carbon signals were very week on the region other than the assembly, which suggests that the surface of the crystal of surfactant was more preferable for SWCNT adsorption than the surface of the substrate (SiO_2 (100 nm)/Si). Thus we assume the following scenario of the self-assembled processes: During the vaporization processes of the solution in which SWCNTs were mono-dispersed, SWCNTs were dominantly assembled on the surface of crystals and aligned according to the needle like shape of the crystals.

2.3 Transfer characteristics of SWCNTs assembly

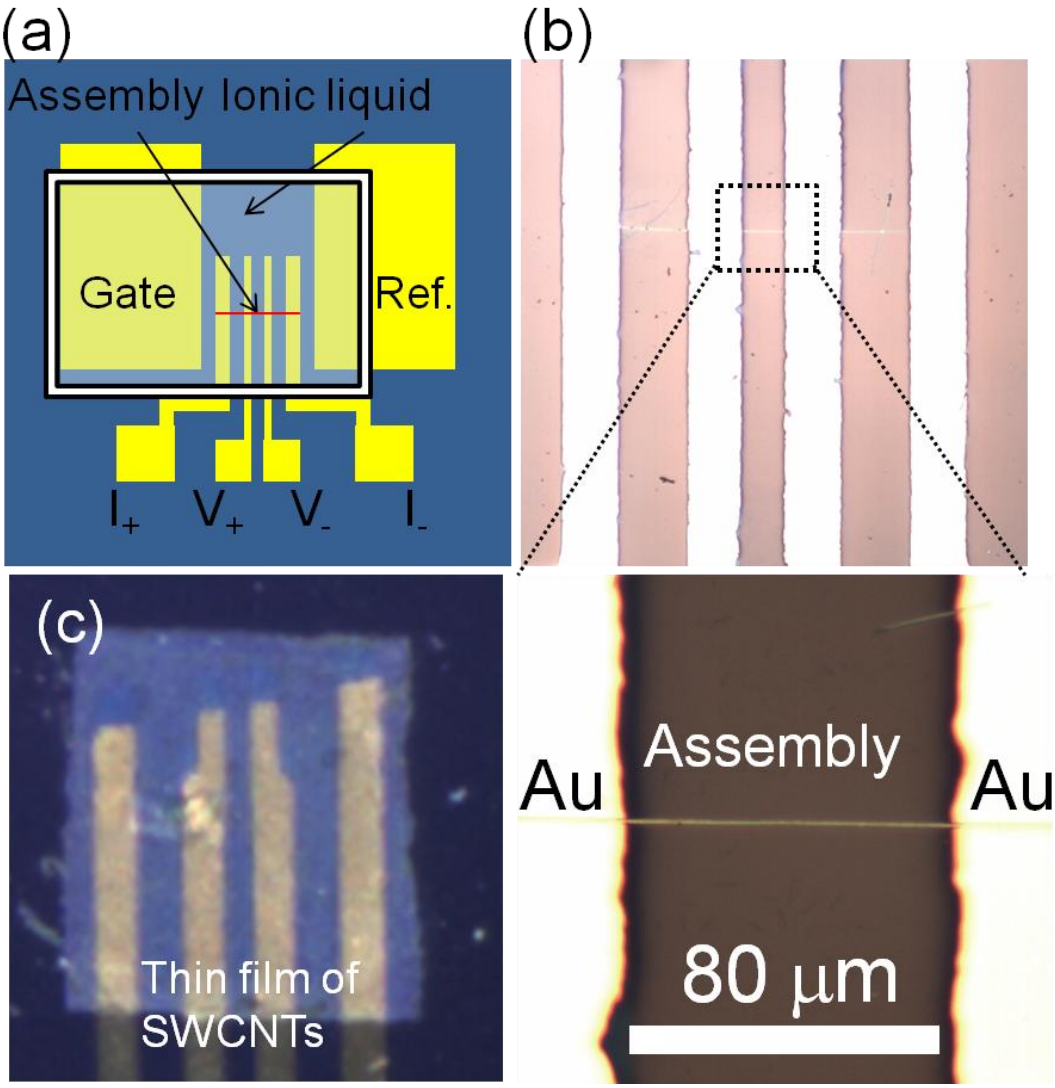

Fig. 2.4 (a) Schematic illustration of experimental setup for field effect transistor and electrical transport measurement. (b) Photograph of the device of assembly. (c) Photograph of thin film of SWCNTs.

To investigate electrical properties of the assembly, we measured transfer characteristics of the assembly of semiconducting and metallic SWCNTs with average diameters of 1.4 nm. A schematic of the device structure is shown in Fig. 2.4 (a); Au (100 nm) / Ti (5 nm) electrodes were attached to the assembly. The distance between I_+ - I_- and V_+ - V_- are 400 μm and 80 μm, respectively. The V_+ and V_- terminals correspond to drain and source electrode. An ionic liquid (N,N,N-trimethyl-N-propylammonium

bis (trifluoromethanesulfonyl) imide (TMPA-TFSI, Kanto-Kagaku Co.) was used for carrier injections through electric double layers. Details of this technique and operating principle of the device are written in sec 5.4.1 and 5.4.2, respectively. This measurement was performed under the vacuum, 10^{-3} Pa, at room temperature. Fig. 2.4 (b) shows a photograph of the Au pattern we used and channel of the assembly is shown in bottom. For comparison we prepared thin film of SWCNTs as shown in Fig. 2.4 (c) where SWCNTs are randomly distributed (details of preparation of the film are written in sec 5.2.3).

Fig. 2.5 shows the transfer characteristics of the assembly and thin film of SWCNTs as a function of channel voltage. In the case of semiconducting SWCNTs assembly the on/off ratio was 1.30×10^5 at source-drain voltage, $V_D = 0.3$ V as shown in Fig. 2.5 (a), which reflects characteristics of semiconductor (electric structure of SWCNTs is demonstrated in section 5.1). The on state conductivity of the assembly was 2.31×10^3 Sm^{-1}. Cao *et al.* reported production of film in which SWCNTs are highly aligned (the alignment ratio I_{max}/I_{min} of approximately 10 with density of approximately 1000 tubes / μm) using Langmuir-Schaefer method.[109] The on state conductivity of their assemblies was evaluated to be 8.14×10^3 Sm^{-1} from the reported structural information.[109] Thus, the on-state conductivity of our assembly is comparable to the best reported assemblies of aligned array of semiconducting SWCNTs.

For comparison of device performance we measured transfer characteristics of thin film of semiconducting SWCNTs where SWCNTs are randomly distributed. The on/ off ratio was 1.09×10^3 at $V_D = 0.2$ V as shown in Fig. 2.5 (b). Capacitance of semiconducting SWCNTs was measured using impedance analyzer (details of capacitance measurement are written in section 5.7) and maximum field effect mobility was evaluated to be 11.2 $cm^2/V \cdot S$ (hole region) for the assembly and 6.2 $cm^2/V \cdot S$ (hole region) for thin film, respectively. The value of field effect mobility of the assembly was approximately 2 times larger than that of thin film of SWCNTs. We also measured transfer characteristics of assembly and thin film of metallic SWCNTs. The on off ratio was 8.25 and 1.86 for the assembly and thin film. Evaluated field effect mobility was 54.5 $cm^2/V \cdot S$ (electron region) for the assembly and 2.8 $cm^2/V \cdot S$ (electron region) for thin film, respectively. The value of mobility in the assembly was approximately 20 times larger than that of random networks. Those results show that the field effect performance was improved in the SWCNTs assembly.

Although we observed improvement of device performance in our semiconducting and metallic assembly, the value of improved mobility was lower than that of single bundle of semiconducting SWCNTs (200 $cm^2/V \cdot S$) where sorted SWCNTs in solution process were used as sample. The reason of the lower value of our assembly may come from presence of tube-tube junctions along tube axis because averaged length of single SWCNTs in our assembly is approximately 1 μm but channel length is approximately 100 μm.

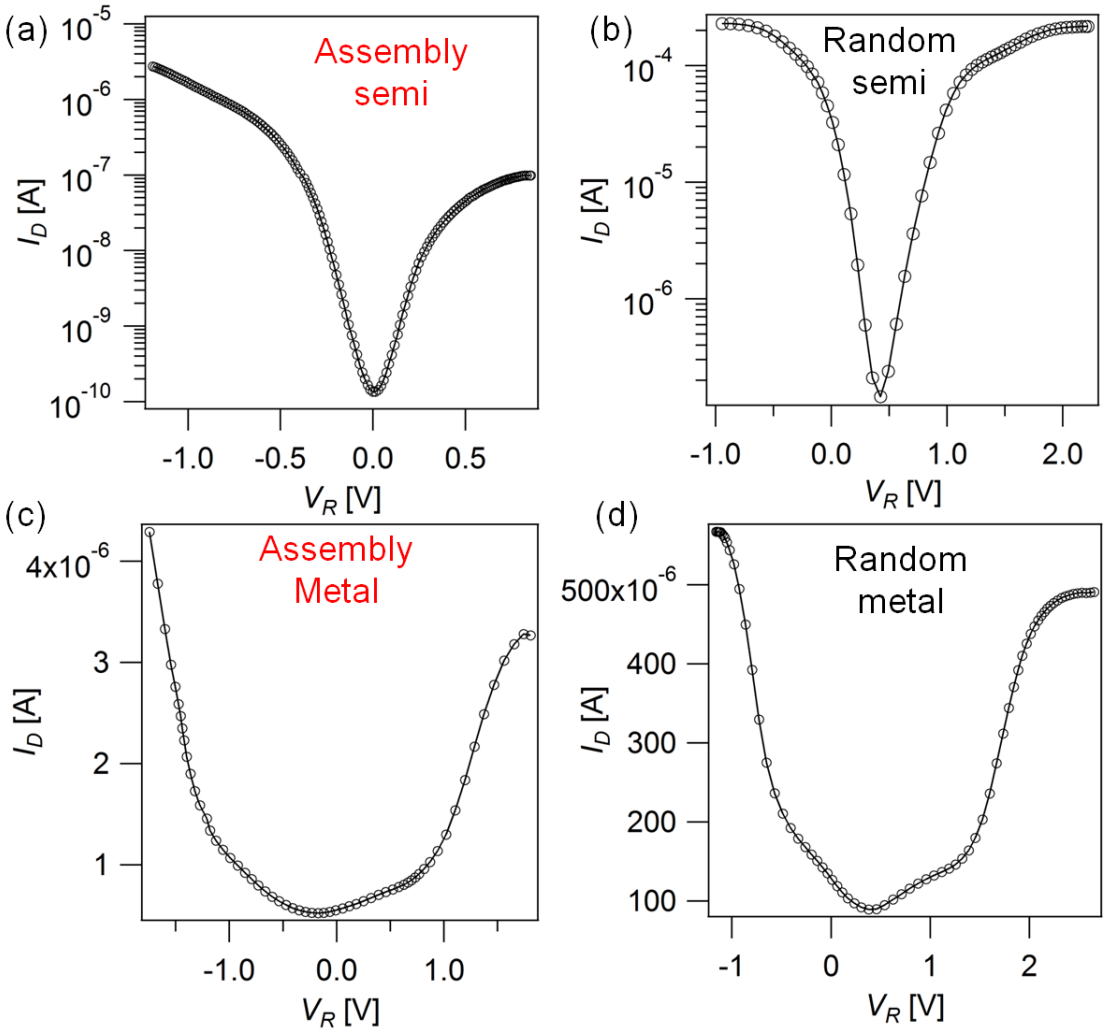

Fig. 2.5 Transfer characteristics of assembly and random network SWCNTs. (a) and (b) show the results of semiconducting SWCNTs for assembly and thin film SWCNTs, respectively. The results of metallic SWCNTs are also shown in (c) and (d). The applied voltage was swept from positive to negative direction in the all experiment.

2.4 Hall effect measurement

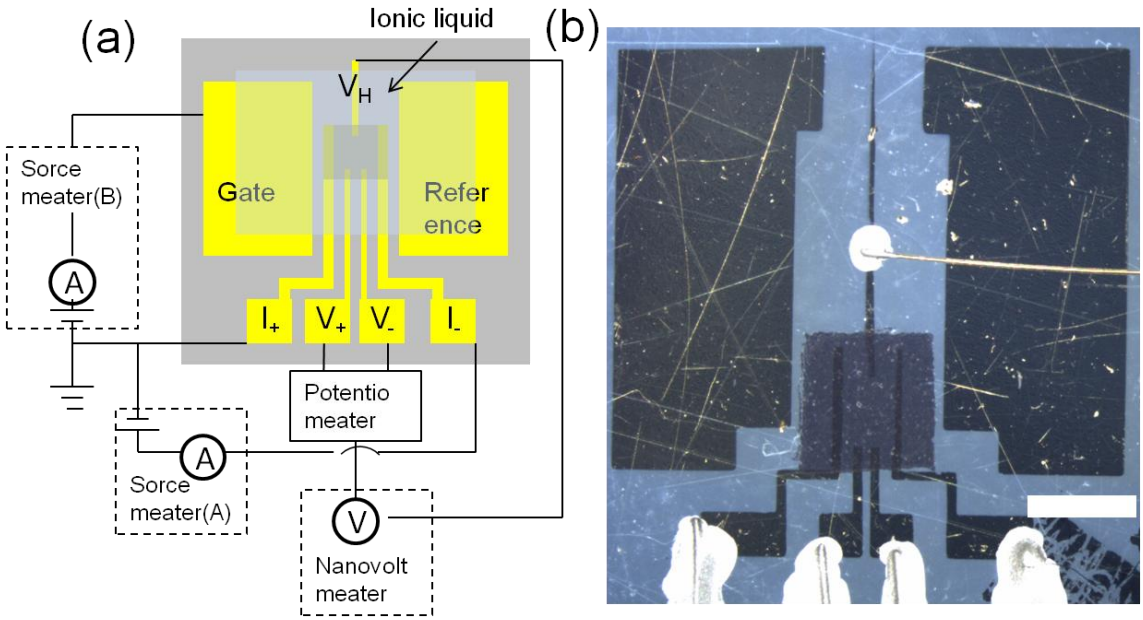

Fig. 2.6 (a) Schematic illustration of experimental setup for field effect transistor and Hall effect measurement. (b) Photograph of the device. Scale bar is 1mm.

Although we evaluated carrier density and field effect mobility from the results of transfer characteristics and capacitance measurement, direct measurement of such parameter is important. Therefore we performed Hall effect measurement to investigate effective carrier density and mobility in SWCNT networks. Fig. 2.6 shows device configuration of Hall effect measurement. Au (100 nm) electrodes were attached to the polyethylene terephthalate substrate as shown in Fig. 2.6 (b). Hall voltage was measured using the V_+, V_- and V_H. We used potentiometer to correct the effect of mismatch between the position of V_+, V_-, and V_H along the current direction. The Hall effect measurement was performed at 200 K in order to freeze ions in the ionic liquid. Magnetic field was swept from 9 T to -9 T. The film thickness was 1.0 μm and 0.8 μm for semiconducting and metallic SWCNT networks, respectively.

Fig. 2.7 (a) and (e) show conductivity as a function of reference voltage for semiconducting and metallic SWCNT networks, respectively. Ambipolar behavior was clearly observed in both types of SWCNTs. The on off ratio was 7.2×10^2 and 4.27 for semiconducting and metallic SWCNT networks, respectively. The results indicate that majority carrier was changed by electrolyte gating technique. Fig. 2.7 (b) – (e) and (f) –

(h) show Hall voltage as a function of times under carrier injection by electrolyte gating technique. Magnetic field is plotted on right axis. In the case of nondoped state where conductivity was minimum in Fig. 2.7 (a) and (e), the Hall voltage did not depend on the magnetic field in both semiconducting and metallic SWCNT networks as shown in Fig. 2.7 (b) and (f). However, in the case of doped state, the Hall voltage clearly depends on the magnetic field as shown in Fig. 2.7 (c), (d) and (g), (h). In the N-doped state, the Hall voltage behaved as expected in equation (5.41) (See section 5.5.2) and carrier concentration was evaluated to be 2.1×10^{22} cm^{-3} and 1.4×10^{22} cm^{-3} for semiconducting and metallic SWCNT networks, respectively. However, in the P-doped state, the Hall voltage disagreed with that expected in equation (5.41) (See section 5.5.2) in both semiconducting and metallic SWCNT networks. Therefore, we could not evaluate the carrier concentration from this data. In the case of N-doped state the carrier concentration evaluated from Hall effect measurement was two order of magnitude larger than that by capacitance measurement (See Fig. 5.30. in section 5.7.3). Therefore the behavior of the Hall effect in the nanotube networks is still under discussion.

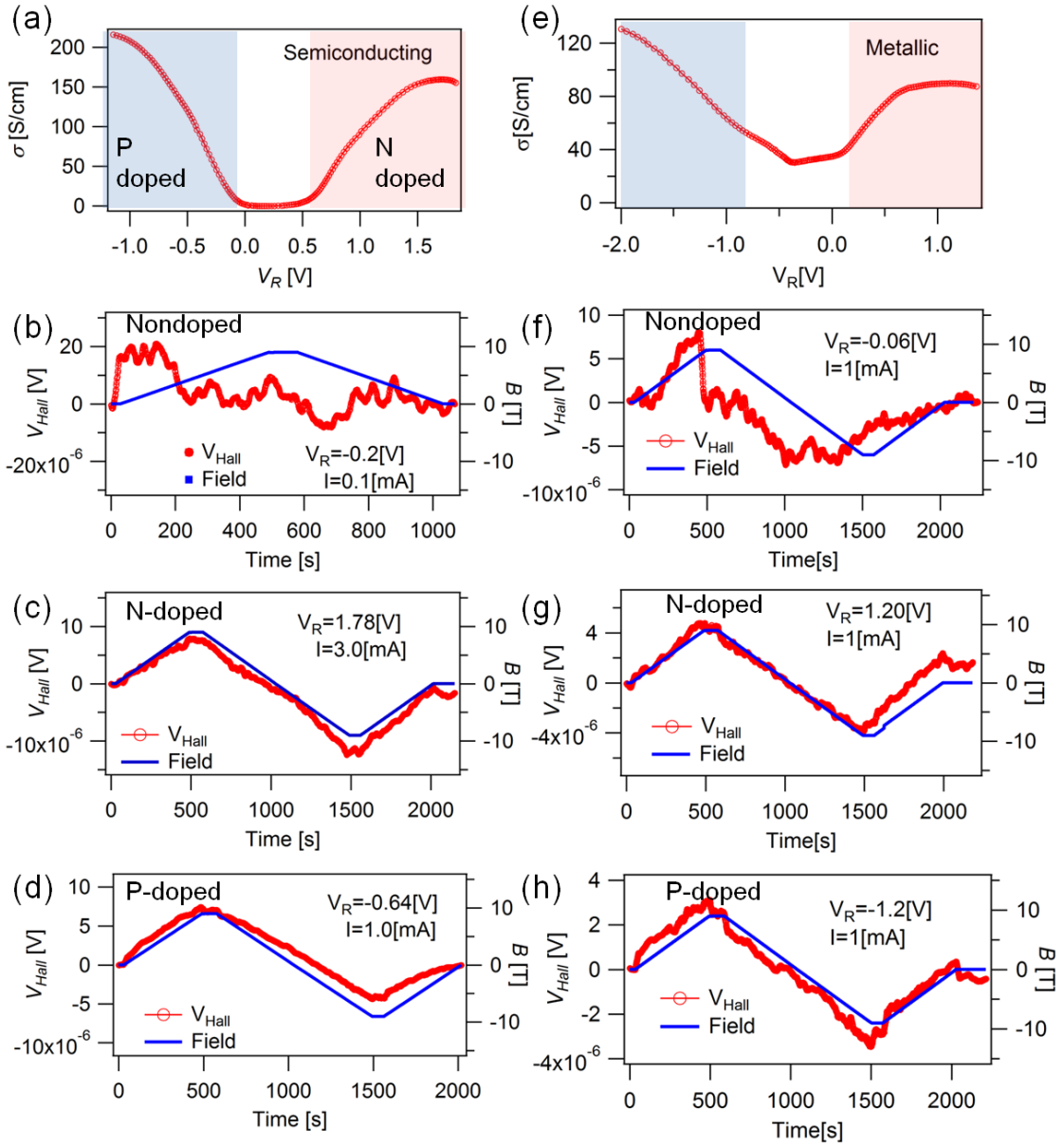

Fig. 2.7 (a) and (b) show conductivity of semiconducting and metallic SWCNT networks, respectively. Red and Blue line indicate N-doped and P-doped region, respectively. (b) and (f) show time dependence of Hall voltage in nondoped state. (c) and (g) show that of N-doped state. (d) and (h) shows that of P-doped state. Red and blue lines show Hall voltage and magnetic field, respectively. The applied voltage and current are also shown in the Figures.

2.5 Electrical transport measurement

To understand effect of carrier injection on transport mechanism of SWCNTs

networks we performed 4-terminal resistance measurement of the metallic, semiconducting, and (6,5) enriched SWCNT thin film. Fig. 2.8 (a), (b) and (c) shows transfer characteristics of semiconducting, metallic and (6,5) enriched SWCNTs networks using electrolyte gating technique. The drain current was plotted as a function of reference voltage. Ambipolar behavior was clearly observed in the all type of SWCNT networks. In Fig. 2.8 (d), (e) and (f) we show normalized resistance of SWCNT networks as a function of temperature under carrier injection. In both doped and nondoped state the normalized resistance increased as the temperature decreased in the all type of SWCNTs. This behavior is consistent with previous reports where resistivity of SWCNT networks was controlled by chemical doing.[27]

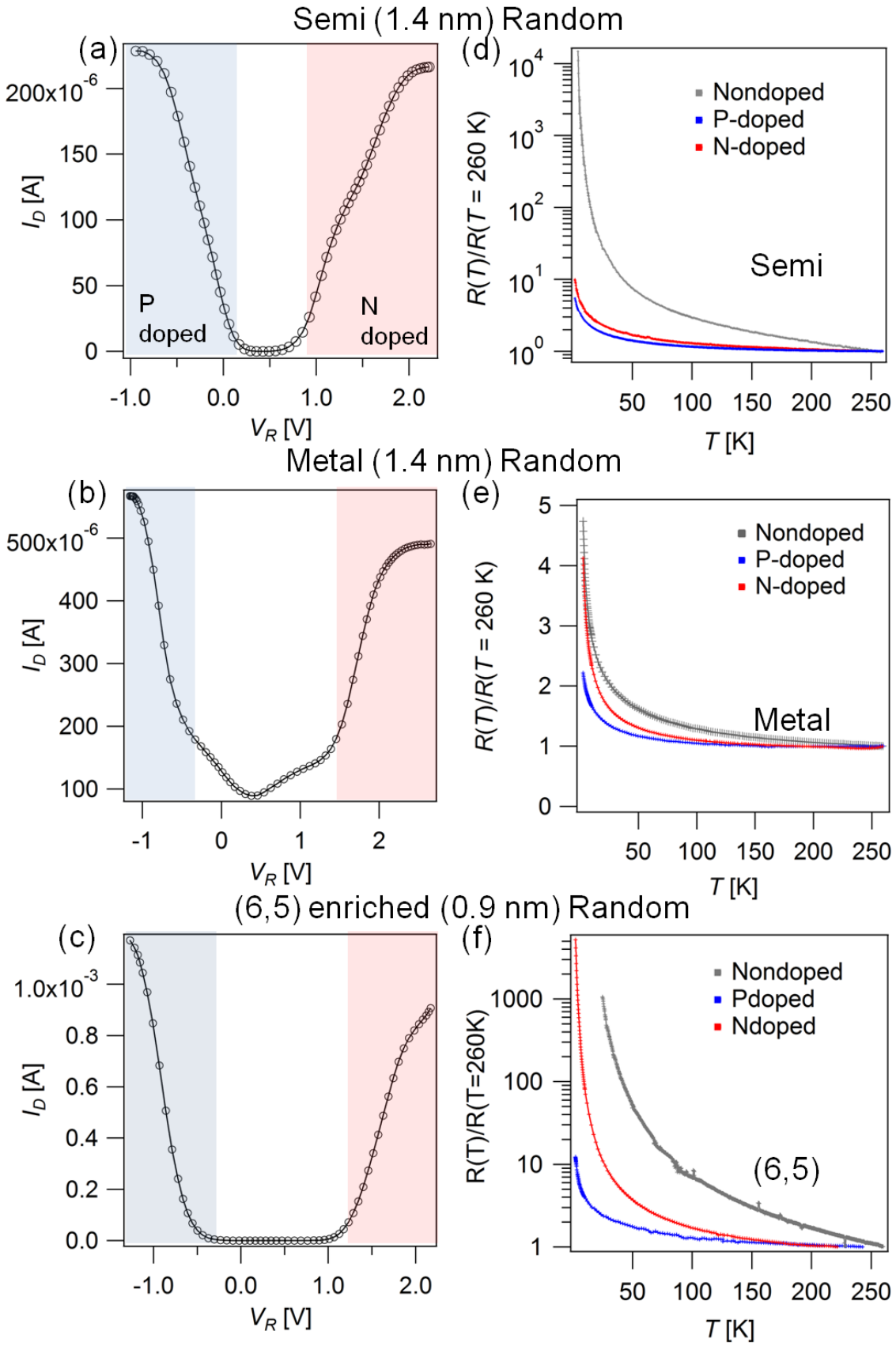
Semi (1.4 nm) Random
(a)
200x10-6
150
100
50
0
ID [A]
P
doped
N
doped
-1.0
0.0
1.0
2.0
VR [V]
(d)
10^4
10^3
10^2
10^1
10^0
R(T)/R(T = 260 K)
Nondoped
P-doped
N-doped
Semi
50
100
150
200
250
T [K]
Metal (1.4 nm) Random
(b)
500x10-6
400
300
200
100
ID [A]
-1
0
1
2
VR [V]
(e)
5
4
3
2
1
0
R(T)/R(T = 260 K)
Nondoped
P-doped
N-doped
Metal
50
100
150
200
250
T [K]
(6,5) enriched (0.9 nm) Random
(c)
1.0x10-3
0.8
0.6
0.4
0.2
0.0
ID [A]
-1.0
0.0
1.0
2.0
VR [V]
(f)
1000
100
10
1
R(T)/R(T=260K)
Nondoped
Pdoped
Ndoped
(6,5)
50
100
150
200
250
T [K]

Fig. 2.8 Transport characteristic of (a) semiconducting, (b) metallic and (6,5) enriched SWCNT networks using electrolyte gating technique. Temperature dependence of resistance of the SWCNTs networks are shown in (d), (e) and (f). The resistance was measured down to 2 K and normalized at 260 K. Red and blue lines represent N-doped and P-doped state, respectively. Grey represents nondoped state where electrolyte gating was not performed.

Table 2.1 Relationship between type of SWCNTs, injected carrier, and normalized resistance at low temperature

Doped carrier	Semi	Metallic	(6,5)
Non-doped	$\frac{R(4.6K)}{R(260K)} = 14796$	$\frac{R(3K)}{R(260K)} = 4.6$	$\frac{R(25K)}{R(260K)} = 1062.0$
N-doped	$\frac{R(3K)}{R(260K)} = 7.4$	$\frac{R(3K)}{R(260K)} = 4.0$	$\frac{R(3K)}{R(260K)} = 2685.7$
P-doped	$\frac{R(3K)}{R(260K)} = 4.5$	$\frac{R(3K)}{R(260K)} = 2.1$	$\frac{R(3K)}{R(260K)} = 9.9$

In Table 2.1 we summarized the relationship between type of SWCNTs, injected carrier, and normalized resistance at low temperature. The increase of resistance of metallic SWCNTs at low temperature was the lowest in the three types of SWCNTs. The increase of resistance of SWCNT networks come from localization of carriers due to tube-tube junctions. Therefore the results can be interpreted that localization of carriers in metallic SWCNT networks is the most suppressed in the three types of SWCNTs. On the other hands, metallic conduction has been observed in single bundle of SWCNTs.[111] Metallic SWCNTs is the most favorable to realize such metallic conduction in the three type of SWCNTs. Therefore, we expected the metallic conduction in aligned assembly of metallic SWCNTs. We prepared the assembly of metallic SWCNTs for temperature dependence resistance measurement to understand transport mechanism in the assembly.

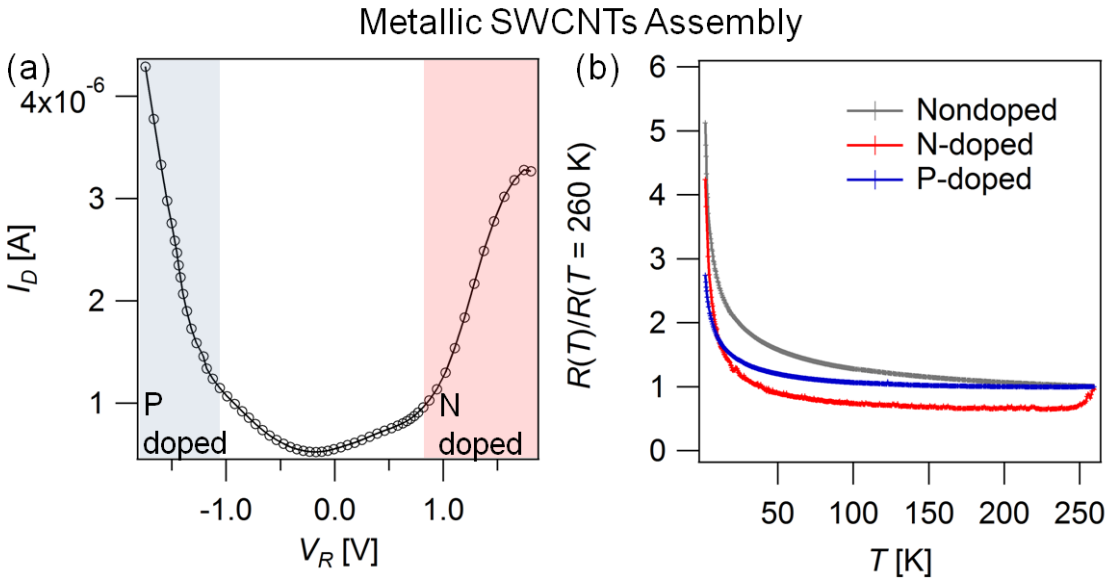

Fig. 2.9 (a) Transfer characteristics of assembly of metallic SWCNTs. Red and blue lines represent N and P-doped state respectively. (b) Normalized resistance as a function of temperature. Grey line represents nondoped state, red and blue lines represent N-doped and P-doped state, respectively. Resistance was normalized at 260 K.

Fig. 2.9 (a) shows transfer characteristics of the assembly of metallic SWCNTs. Fig. 2.9 (b) shows normalized resistance as a function of temperature. The resistance increased as temperature decreased. The transport mechanism of the assembly and random networks of metallic SWCNTs are analyzed using a variable range hopping model based on the following equation[112,113]:

$$R(T) = R_0 \exp\left[\left(\frac{T_0}{T}\right)^{\frac{1}{d+1}}\right] \tag{2.2}$$

$$T_0 = \frac{\beta_d}{k_B D(\mu) a^d} \quad \text{for } d = 2 \text{ or } 3. \tag{2.3}$$

T_0 is a characteristic temperature used in the VRH model, a is a localization radius of states, β_d is a constant and $D(\mu)$ is a density of states at Fermi level. Here, d has a value of either 2 or 3 in Mott-VRH, or 1 in ES-VRH. Details of VRH model are written in sec 5.5.1. Temperature dependence of resistance of the assembly and thin film are compared as shown in Fig. 2.10 (a) and (d), respectively. Fig. 2.10 (b) and (e) show logarithmic derivative method where $W = -\mathrm{d}(\ln R / \ln T)$ is plotted as a function of $\ln T$ to linearize $R = R_0 \exp(T_0 / T)^x$, evaluating the number of x directly from the slope. For

example, in the case of the assembly the slope was -0.22 for N-doped state, which is classified in d =3 in Mott-VRH. In this manner we classified the hopping dimension of the assembly and thin film of metallic SWCNTs. In Fig. 2.10 (c) and (f) we plotted ln$R$ against $T^{-1/(1+d)}$ with deduced d. The ln$R$ lineally behaved against $T^{-1/(1+d)}$ in both the assembly and thin film, which indicates that our data were well fitted by VRH model. We evaluated the T_0 from the slope as shown in Fig. 2.10 (c) and (f). The hopping dimension and T_0 are summarized in Table 2.2 (we also analyzed the case of semiconducting and (6,5) enriched SWCNT networks in section 5.8). Although T_0 of assembly is different from random networks, behavior of resistance can be fitted by VRH model with d = 3 regardless of alignment and carrier doping. This result indicates that alignment conditions of SWCNTs in this study have little effects on transport mechanisms in the assembly.

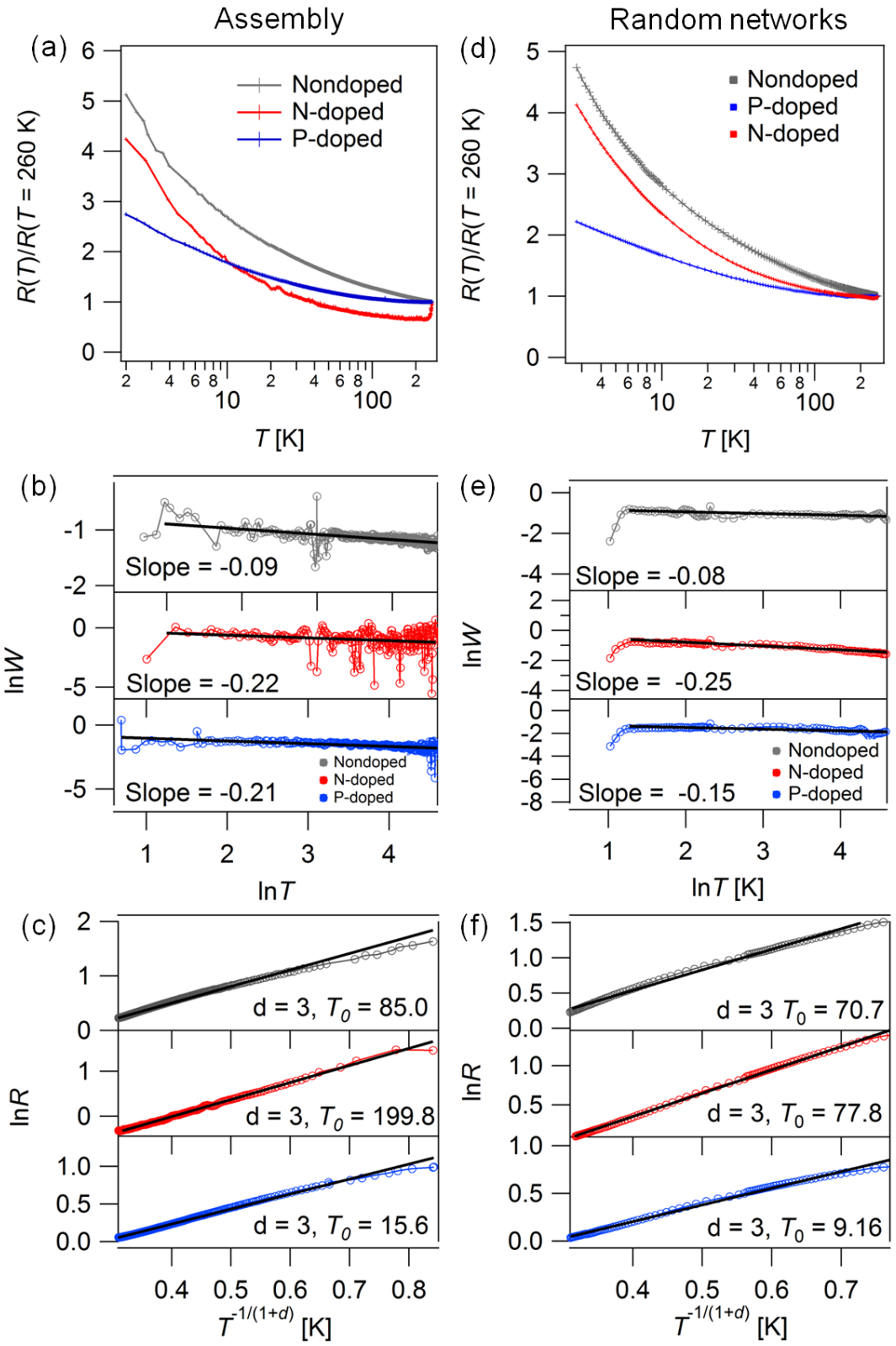

Fig. 2.10 Analysis of transport mechanism of the assembly and thin film using VRH model. (a) and (d) show temperature dependence of resistance for the assembly and

thin film, respectively. (b) and (e) show ln W versus ln T. Grey line shows nondoped state, red line and blue line show N-doped and P-doped state, respectively. (c) and (f) shows ln$R$ versus $T^{-1/(1+d)}$. Black lines show their linear fitting.

Table 2.2 Relationship between doped carrier, hopping dimension, and T_0.

Doped carrier	Assembly	Random
Non-doped	$d=3, T_0=85.0$	$d=3, T_0=70.7$
N-doped	$d=3, T_0=199.8$	$d=3, T_0=77.8$
P-doped	$d=3, T_0=15.6$	$d=3, T_0=9.1$

In this study, we found that field effect mobility was improved in aligned assembly compared with random networks in section 2.3 but transport mechanism was almost no changed. Here, we briefly discuss the background of this result. In the case of aligned assembly of SWCNTs, the number of tube-tube junctions between electrodes may be reduced compared with random networks. Therefore, carrier mobility can increase in aligned assembly. However, although SWCNTs are well aligned, careers must pass tube-tube junctions and they thermally hop from tube to tube at junction point. Therefore, transport mechanism was unchanged even if SWCNTs are highly aligned in the assembly of this study.

2.6 Summary

In summary, we developed a new method to prepare an assembly of aligned SWCNTs using a crystal template method. Polarized micro-Raman measurements showed that the SWCNTs were highly aligned parallel to the crystal axis. SEM images clearly showed that approximately 70 % of the SWCNTs were aligned parallel to the crystal axis within 7 ° and in good agreement with the polarized micro-Raman measurement. The crystal template method was applicable for various SWCNTs samples, such as highly purified metallic, semiconducting and (6,5) SWCNTs. Field effect mobility of semiconducting SWCNTs assembly was 2 times larger than that of thin film and that of the metallic SWCNTs assembly was 20 times larger than that of thin film. Those results illustrate the high density and good alignment of SWCNTs in both semiconducting and metallic SWCNTs. Temperature dependence of resistance of metallic SWCNTs assembly was compared with that of random networks. Analysis using VRH model showed that alignment of SWCNTs has little effect on transport mechanism.

2.7 Outlook

In this study, we found that tube-tube junctions between electrodes are dominant in transport mechanism in aligned assembly and the behavior of resistance of the assembly was well fitted by variable range hopping. Fischer et al. has reported metallic conduction in single bundle of SWCNTs.[111] To realize such metallic conduction, it is necessary to remove tube-tube junctions between electrodes, or to control the junctions. Fabrication of aligned assembly using long SWCNTs or using electrodes with short length can realize such situation. Therefore, investigation of electronic properties of assembly in such situation will be important for realization of metallic conduction as well as superior device performance.

3 Thermoelectric property of nanotube networks

3.1 Introduction

Thermo-power of one-dimensional materials significantly depends on a position of Fermi level due to presence of Van-Hove singularities in density of states. Since discovery of CNTs in 1991[10], cylindrical materials such as SWCNTs and WS_2 NTs have attracted a lot of attentions due to their unique physical properties. In general, their one-dimensional structure is advantageous in thermoelectric applications, as reported by Hicks and Dresselhause.[63] For example, a figure of merit, *ZT*, can be significantly enhanced as the diameter of a one-dimensional system decreases.[63] In addition, materials with cylindrical structure have been expected to have superior *ZT* value due to reduction of thermal conductivity.[67,68]

SWCNTs are one-dimensional rolled graphitic materials[11], and because of their low-dimensionality, their thermoelectric properties have attracted a lot of interest and have been investigated.[69,72,114,115] Recently, a very large Seebeck coefficient has been observed in the semiconducting types of SWCNT networks[115], and tuning of their thermoelectric properties, especially p-type and n-type control, is currently of great interest. As previously mentioned, Seebeck coefficients of SWCNTs significantly depends on Fermi level, thus determination of the Seebeck coefficients as a function of the Fermi level is very important for correct tuning of thermoelectric properties.

On the other hands, WS_2 NTs are cylindrical nanotubes with a rolled structure consisting of two-dimensional WS_2 sheets.[12] Quantized conditions along the circumferential direction of the nanotubes, owing to their chiral structure and Van-Hove singularities that reflect their one-dimensional nature, result in an electronic structure that is distinct from that of two dimensional sheets and exhibits unique physical properties; thus, the physical properties of WS_2 NTs have attracted substantial attention.[17,66,116] As a result, since the discovery of WS_2 NTs in 1992,[12] various physical properties, such as electrical,[117,118] optical,[119] and mechanical properties,[120,121] have been reported for the nanotubes in their single rope form. However, relatively strong van der Waals forces between WS_2 NTs make them bundle

together and, as a result, WS_2 NTs tend to form macroscopic networks.[122,123] Such networks provide strong advantages in the fabrication of devices with good scalability. Previously, investigations of the electrical properties of WS_2 NTs have been limited to the single roped state because of the insulating properties of WS_2 NT networks.[117-119] However, in 2016, Sugahara et al. succeeded in introducing carrier injections into thin films, specifically, the random networks of WS_2 NTs, and demonstrated their ambipolar field effect transistor characteristics by using the electrolyte gating method.[77] This technique has paved the way for investigating the electrical properties of the macroscopic networks of WS_2 NTs.

This type of electrolyte gating method has recently been revealed to be applicable to the control of various physical properties in nanotube networks. For example, controlling the shift in Fermi level using electrolyte-gating technique has resulted in modifications of the electrical and optical properties of SWCNTs, such as conductance[88,124,125], optical absorption[89], and electro-luminescense[126]. Therefore, in this chapter, we investigated the thermoelectric properties of SWCNTs and WS_2 NT networks using electrolyte gating approaches.

In chapter 3, our purpose is to reveal relationship between thermoelectric properties of nanotube networks and a position of Fermi level. First, we introduce thermoelectric measurement of SWCNTs using electrolyte-gating technique. We discuss problems of thermoelectric properties of SWCNTs. Second, as another one-dimensional material, we investigated thermoelectric properties of WS_2 NTs. We discussed the effectiveness of electrolyte-gating technique for thermoelectric measurement of WS_2 NT networks by comparing the results with those obtained in a conventional back-gating technique. Finally, we discussed differences between thermoelectric properties of SWCNTs and WS_2 NTs, and potential of thermoelectric performance of those nanotubes by comparing other bulk and one-dimensional materials.

3.2 Thermoelectric properties of SWCNTs

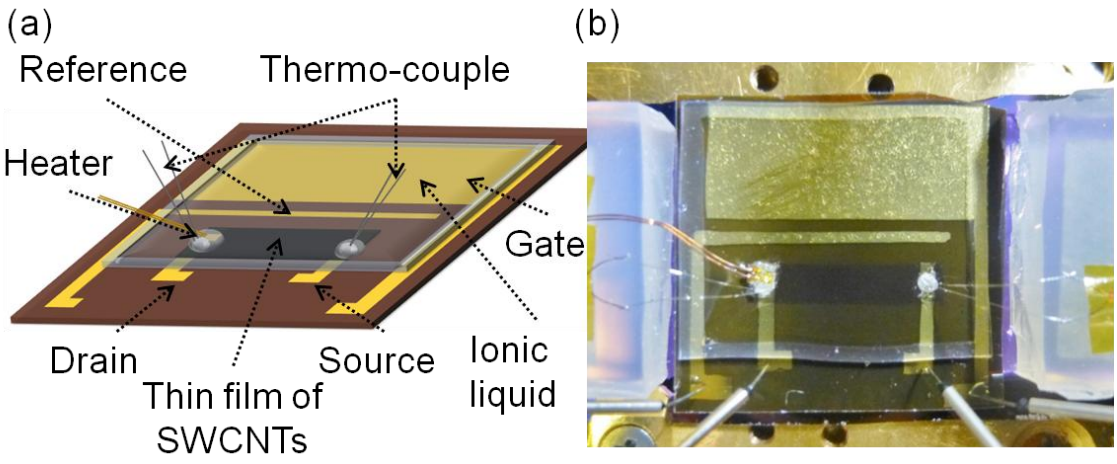

Fig. 3.1 (a) Schematic illustration of the experimental setup for controlling the Seebeck coefficient of SWCNTs through an electric double layer using an ionic liquid. (b) Photograph of the device.

First, we introduce thermoelectric measurement of SWCNTs using electrolyte-gating technique. Fig. 3.1 (a) presents a schematic illustration of the experimental setup for controlling the Seebeck effect through EDLT and photograph of the device was shown in Fig. 3.1 (b). A thin film of high-purity semiconducting and metallic SWCNTs with a diameter of 1.4 nm, which were prepared using typical density gradient techniques,[127-129] was used as the channel between the gold source and drain electrodes. A parylene layer (thickness of approximately 10 μm, parylene HT, Parylene Japan) was formed on the surface of the polyimide substrate for thermal isolation because of its extremely low thermal conductivity, and the device was formed upon the parylene layer. N,N,N-trimethyl-N-propylammonium bis (trifluoromethane sulfonyl) imide (TMPA-TFSI, Kanto Kagaku Co.) was used as the ionic liquid. Thermocouples were directly attached to the SWCNT film using silver paste, and these thermocouples were covered with insulating pastes (GC-P100, Sumitomo 3M Co.) to avoid electro-chemical reactions. One end of the film was heated with a small heater attached to the film, and the actual voltage applied to the sample was measured as the channel voltage from the reference electrode. All of the measurements were performed under vacuum.

Fig. 3.2 shows Seebeck coefficients of semiconducting and metallic SWCNT networks as a function of reference voltages. As shown in the top of the figure, transfer characteristics exhibited ambipolar behavior in both semiconducting and metallic SWCNT networks. As shown in the middle of the figure, Seebeck coefficients were

controlled from N-type to P-type by shifting gate voltage, which consistent with transfer characteristics. There were peaks in the Seebeck coefficient in semiconducting and metallic SWCNT networks, and maximum values of the Seebeck coefficient were approximately 120 and 20 [μV/K] for semiconducting and metallic SWCNTs, respectively. Power factors are shown in the bottom of the figure. The maximum power factor of metallic SWCNT networks was 5 times lower than that of semiconducting SWCNT networks. Therefore, thermoelectric properties are significantly sensitive to their chirality and the amount of injected carriers.

In the case of semiconducting SWCNTs, there are peaks in Seebeck coefficients for both electron and hole injected regions. The width between the electron and hole peaks was approximately 500 mV, which is known to corresponds to shift of Fermi level (500 meV) when Fermi level is located within band gap. Hayashi et al. have reported that the peak width of semiconducting SWCNTs increase from approximately 50 meV to 500 meV when metallic SWCNTs (0.01%) are contained.[130] Therefore, relatively wide peak width in our semiconducting SWCNTs indicate that the presence of residual metallic SWCNTs or semiconducting SWCNTs with different charge neutral points. Those SWCNTs may degrade thermoelectric performance. Therefore we focused on WS_2 NTs as semiconducting nanotubes with wide band gap.

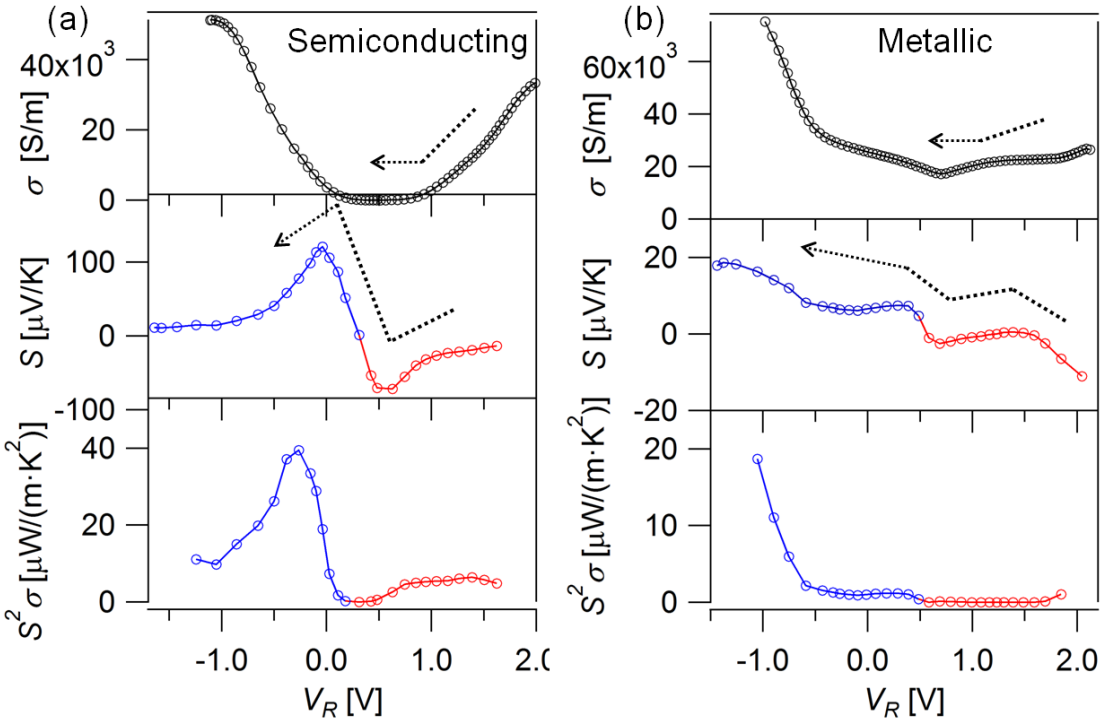

Fig. 3.2 Thermoelectric properties of (a) semiconducting and (b) metallic SWCNT networks. Conductivity, Seebeck coefficient, and power factor as a function of reference

voltage are shown in top, middle, and bottom of the figure, respectively. Red and blue symbol represent electron and hole region, respectively. (Copyright 2014 American Chemical Society)

3.3 Thermoelectric properties of WS_2 NT networks

Fig. 3.3 presents a schematic illustration of the experimental set up for controlling the thermoelectric properties of the WS_2 NT film through electrolyte gating approaches. For thermal isolation of the film, a parylene layer (thickness of approximately 10 μm, parylene HT, Parylene Japan), which formed on the surface of polyimide substrate, was used. Au electrodes (100 nm thickness) were thermally deposited, as illustrated in Fig. 3.3. The channel length was 400 μm, which was crucial for introducing a clear temperature gradient. The film thickness was approximately 1.2 μm in all experiments in this study (details of preparation and optical characterization of the film are written in sec 5.3.1 and 5.3.2, respectively). Thermo-couples (Alumel and Chromel) were attached with silver paste to measure the temperature at both the ends of the film. A heater was attached on the back side of the substrate, as illustrated in Fig. 3.3, to create a temperature gradient. We used N,N,N-trimethyl-N-propylammonium bis (trifluoromethane sulfonyl) imide (TMPA-TFSI, Kanto Kagaku Co.) as the ionic liquid. To avoid electrochemical reactions between the silver paste and the ionic liquid, we coated the silver paste with epoxy adhesive. The generated thermoelectric voltages were measured using source and drain electrodes. The actual voltage applied on the channel was evaluated as the reference voltage, V_R. All of the experiments were performed in vacuum. Preparation of the device is also written in section 5.9.1.

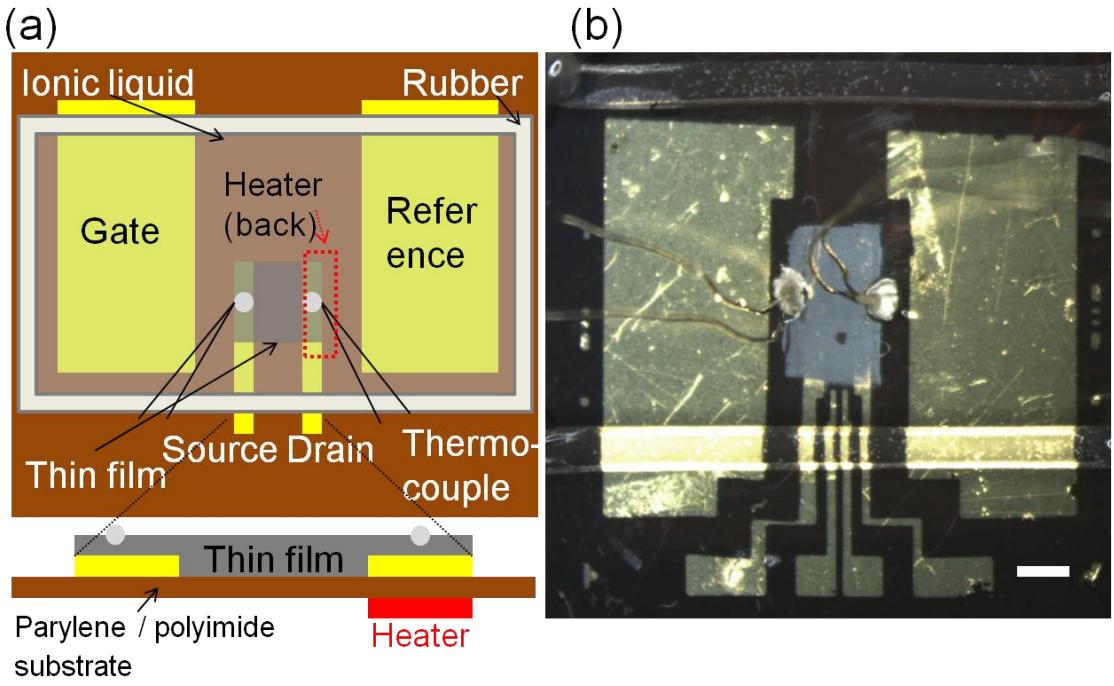

Fig. 3.3 (a) Schematic illustration of experimental set up for field effect transistor and Seebeck coefficient measurement using electrolyte gating techniques. (b) Photograph of the device. Scale bar is 1mm. (Copyright 2017 The Japan Society of Applied Physics)

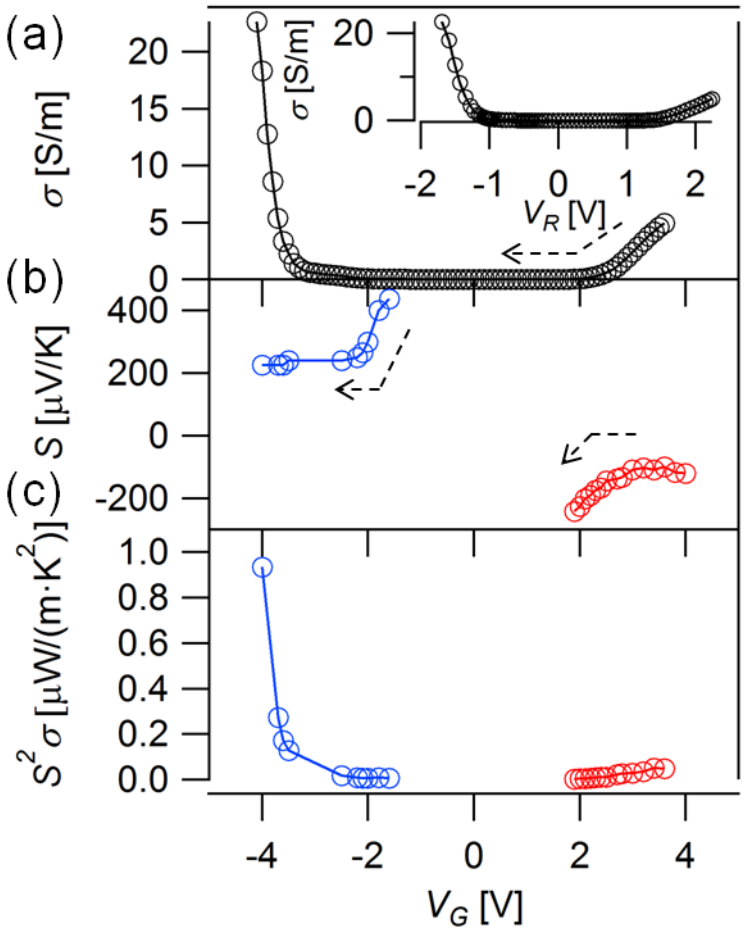

Fig. 3.4 The V_G dependence of (a) conductivity, (b) Seebeck coefficient and (c) power factor at room temperature. Inset in (a) shows the V_R dependence of conductivity. The V_G was swept from the positive to the negative direction in all experiments. Red and blue colors indicate N-type and P-type, respectively. (© 2017 The Japan Society of Applied Physics)

Fig. 3.4 (a) shows the transport characteristics of the film. The conductivities of the film, σ, are plotted as a function of the gate voltage, V_G. The data clearly indicates ambipolar behavior similar to that previously reported[77] and suggested that the electron and hole could be injected through the formation of an electric double layer by electrolyte gating. The on-state conductivities for hole and electron reached 2.2×10^1 *S*/m and 3.3 *S*/m, respectively. The reported value for the on-state conductivity of individual WS_2 NTs was 1.0×10^3 *S*/m,[118] a value two orders of magnitude higher than that presented in our results. Tube-tube junctions may have been the cause of the decreased conductivity in the WS_2 NT film compared with the single roped state.

To discuss electronic characteristics of WS_2 NTs used here, we plot the conductivity of the film as a function of reference voltage V_R as shown in the inset of Fig. 3.4 (a). We evaluated the width of V_R in an off-state (see also Fig. 5.17 in section 5.4.3), and the width was evaluated to be 2.57 ± 0.07 V. We also measured a capacitance of the WS_2 NT networks as a function of reference voltage (see Fig. 5.29 in section 5.7.4). There was dip structure in the capacitance as shown in Fig. 5.29 (c) reflecting the semiconducting band-gap.[131-133] The dip width was evaluated to be approximately 2.5 V, which was similar to the off-state width estimated from the transfer characteristics. Braga et al. have reported that in the case of thin flake WS_2, the band-gap was estimated to be 1.4 eV from the off-state width observed in transfer characteristics.[134] The value well coincides with the band gap of WS_2 bulk crystal (1.3 ~ 1.35 eV). The number of layer in our sample is similar to that reported in the thin flake WS_2 (around 50 layers, details are written in sec 5.3.3), thus the band gap of WS_2 NT networks should be similar to that of WS_2 bulk crystal. However, the observed width of off-state and the capacitance dip was rather large, around 2.5 V. Such increase of the width is often caused by the presence of trap states within the band gap of semiconductor.[135,136]) In the case of transitionmetal dichalcogenides, trap states are generated within the bandgap because of structural defects, such as absence of chalcogen or metal atoms and dislocations of these atoms.[137] The rather large off-state width indicates the presence of numerous trap states in our WS_2 NT networks. Therefore, the rather large off-state width indicates the presence of a large number of trap states in our WS_2 NT networks.

Fig. 3.4 (b) shows the Seebeck coefficient as a function of the gate voltage. Before the gate-controlled thermoelectric measurement, we confirmed the linear relation between the thermoelectric voltage and the temperature gradient (see Fig. 5.34 in section 5.9.2). Both the positive and negative Seebeck coefficients clearly reflected the ambipolar behavior of the WS_2 NT networks. In the V_G region from -1.6 V to 1.9 V, the Seebeck coefficient could not be correctly evaluated due to the limitation of our measurement setups. However, in the V_G region more positive than 1.9 V or more negatives than -1.6 V, the Seebeck coefficient could be evaluated. The Seebeck coefficients tended to decrease as the $|V_G|$ increased. This behavior was consistent with the result in the polycrystals of WS_2 thin flakes,[138] whose Seebeck coefficients were controlled by Indium intercalation. We calculated the power factor $S^2\sigma$ as shown in Fig. 3.4 (c). In both P-type and N-type regions, the power factor increased as the $|V_G|$ increased, thus indicating the importance of carrier injections to achieve better

thermoelectric performance.

We found that the electrolyte gating approach was crucial to reveal the thermoelectric properties of WS_2 NT networks. Here we discuss the results using a back-gating technique in which we used SiO_2 (100 nm) as a gate dielectric. Fig. 3.5 presents relationships between the Seebeck coefficient and the conductivities of the WS_2 NT networks as a function of V_G in the electrolyte gating technique, and the conductivities in the back-gating technique. The Seebeck coefficients became measurable in the region where the conductivity became on-state in both P-type and N-type regions in the electrolyte gating technique. However, in the case of the back-gating technique, the conductivity did not become on-state and thermoelectric properties could not be measured. Levi et al. have reported that the single rope of WS_2 NTs became on-state by the back-gating technique;[118] however, in our thick film sample with a thickness of approximately 1 μm, the conductivity of WS_2 NT networks could not become on-state by this approach. We assume the following backgrounds. In the case of the back-gating technique, the surface roughness and thickness in the thick film would prevent uniform carrier injection into the nanotubes consisting the networks, as a result, the conducting channel could not be formed between the source and drain electrodes by this approach. However, in the case of the electrolyte gating, the electric double layer would be formed on the surface of all the nanotubes in the film, and carriers would be injected to them. As a result, the channel became on-state, and the thermoelectric properties became measurable.

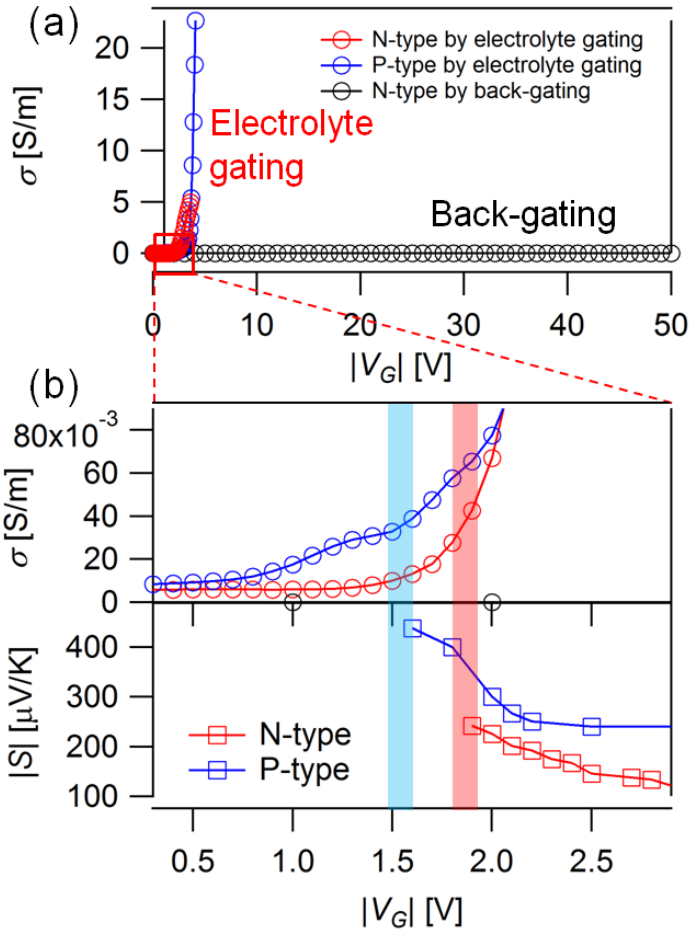

Fig. 3.5 (a) Comparison of the back-gating and electrolyte gating methods in the WS_2 NT networks. Red and blue circles represent the $|V_G|$ dependence of electron and hole conductivities, respectively, using the electrolyte gating technique. Black circles represent the $|V_G|$ dependence of electron conductivity using the back-gating technique. (b) shows the details of the conductivity and Seebeck coefficients in the low $|V_G|$ region of (a). Red and blue colors indicate the N-type and P-type, respectively. Red and blue vertical lines indicate the $|V_G|$ values where the Seebeck coefficients became measurable. (Copyright 2017 The Japan Society of Applied Physics)

3.4 Comparison of thermoelectric properties of SWCNT and WS_2 NTs networks

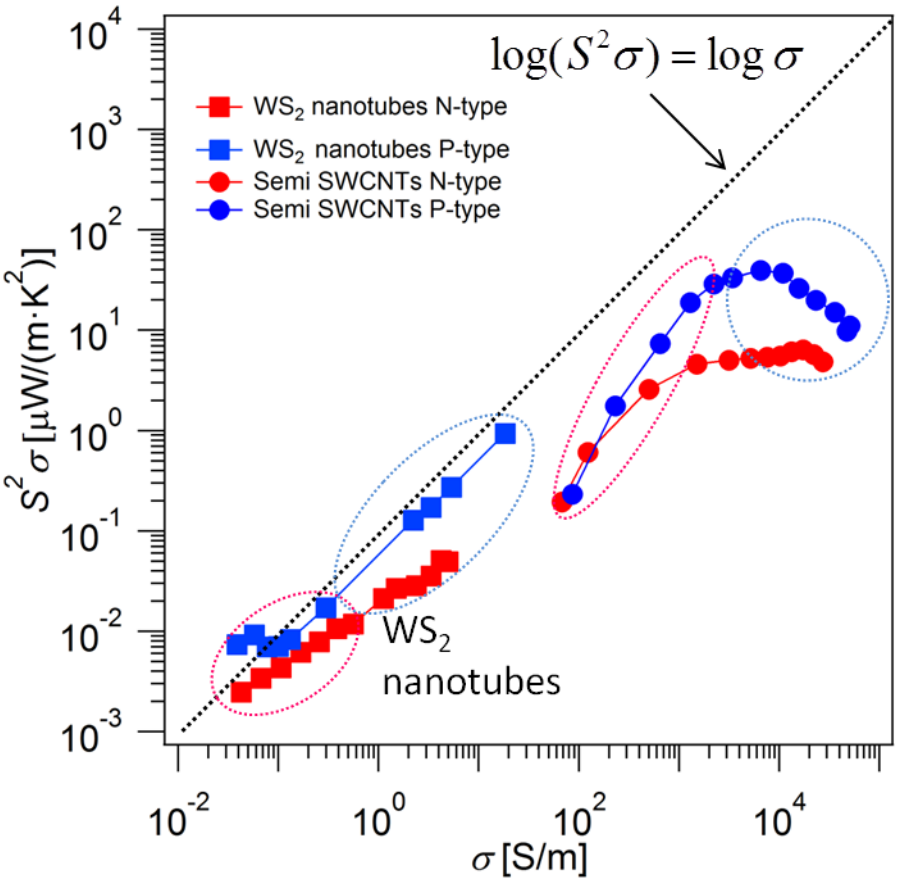

Fig. 3.6 Comparison of power factor of SWCNTs and WS_2 NTs. Red and blue symbols represent N and P type doping, respectively.

Here, we discuss differences between thermoelectric properties of SWCNTs and WS_2 NTs. In Fig. 3.6 we show power factors of semiconducting SWCNTs and WS_2 NTs as a function of their conductivities. In the case of WS_2 NTs, $\log(S^2 \cdot \sigma)$ linearly increased against $\log \sigma$. On the other hands, $\log(S^2 \cdot \sigma)$ has peak in semiconducting SWCNTs. To discuss the background of these behaviors, we used following simple models where conductivity depends on Fermi level as,

$$\sigma \approx \exp(\alpha E_F) \tag{3.1}$$

$$\sigma \approx E_F^n \tag{3.2}$$

Equation (3.1) corresponds to a situation where Fermi level is located within band gap. In the case of equation (3.2), Fermi level is located in conduction or valence bands. If conductivity depends only on density of states, which means that relaxation time does not depend on the location of Fermi level, on the basis of a free electron model, the n of equation (3.2) can be written as,

$$n = \begin{cases} \frac{1}{2} & \text{for 1D,} \\ 0 & \text{for 2D,} \\ -\frac{1}{2} & \text{for 3D} \end{cases} \tag{3.3}$$

Using those equations and Mott formula, we can derive a power factor as

$$\log(S^2\sigma) = A + \log\sigma \tag{3.4}$$

$$\log(S^2\sigma) = B + \frac{n-2}{n}\log\sigma \tag{3.5}$$

Here, A and B are constant values. Equation (3.4) and (3.5) corresponds to the case of equation (3.1) and (3.2), respectively. In the case of semiconducting SWCNTs, in a region marked by a pink dashed line in Fig. 3.6, the behavior of power factor corresponding to equation (3.4), which can be interpreted that Fermi level is located within band gap. In a blue dashed line region, the behavior corresponds to equation (3.5) with n = 1/2, which can be interpreted that Fermi level is located in valence or conduction band. This interpretation is consistent with the results of transfer characteristics of semiconducting SWCNTs. In the case of WS_2 NTs, a pink dashed line region corresponds to equation (3.4). However, although transfer characteristics of WS_2 NTs showed that in a blue dashed region, Fermi level is inside conduction and valence band, thus in this region, the power factor will behave like the equation (3,5), but the behavior corresponds to equation (3.4). This discrepancy suggests that even if Fermi level is among the band gap and located inside valence and conduction band, higher conduction and valence bands affects the conductivity of WS_2 NTs.

3.5 Summary

In summary, we investigated thermoelectric properties of SWCNTs and WS_2 NT networks. By using an electrolyte gating approach, we achieved ambipolar transfer characteristics in the SWCNTs and WS_2 NT networks channel, and evaluated the thermoelectric properties, Seebeck coefficients and power factors of the nanotube networks. The power factor was significantly improved by carrier injections. In addition, we succeeded to interpret thermoelectric properties of SWCNTs and WS_2 NTs by assuming simple models in conductivity.

3.6 Outlook

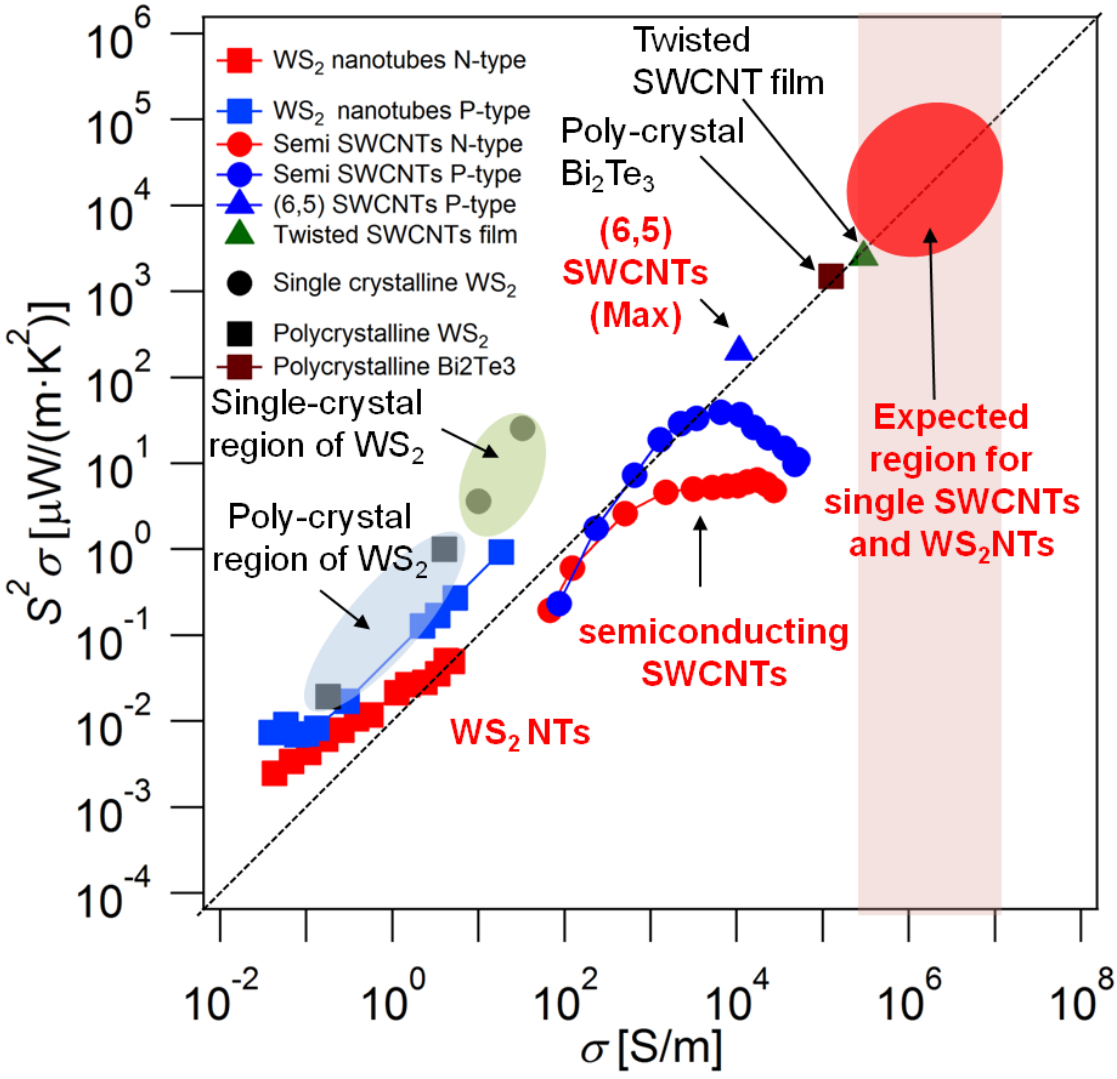

Fig. 3.7 The $S^2\sigma$ values of the SWCNTs (Red and blue circle), WS_2 NTs (Red and blue square), single crystalline WS_2[139,140] (Green region), polycrystalline WS_2 flakes[138,141] (Blue region), polycrystalline Bi_2Te_3[142] (Brown square) and twisted SWCNT film[143](Green triangle) as a function of σ. Red and blue symbol represent N-type and P-type of powerfactor, respectively. The red region represents expected region for single SWCNTs and WS_2 NTs.

In Fig. 3.7, we show comparison of power factors of SWCNTs and WS_2 NTs with other materials. The power factors of WS_2 NTs are comparable to polycrystalline WS_2, [138,141] but lower than single crystalline WS_2 sample.[139,140] The power factors of semiconducting SWCNTs are better than WS_2 NTs. The power factors of (6,5) SWCNTs are better than those of semiconducting SWCNTs but lower than those of conventional Bi_2Te_3[142]. Recently, it has been reported that twisted SWCNTs film exhibits excellent

power factors, which are higher than Bi_2Te_3.[143] This increase of power factor can be interpreted as increase of conductivity of sample. In cases of single tube forms of SWCNTs and WS_2 NTs, their conductivities have been reported to be approximately 10^7 S/m for SWCNTs[144] and 10^5 ~ 10^7 S/m for WS_2 NTs [118], respectively. These conductivities are located in a region surrounded by pink lines in Fig. 3.7. Origins of the difference between conductivity of single nanotube and networks are tube-tube contact resistances and packing densities of nanotubes in the networks. Therefore, single crystalline nanotube where nanotubes are highly and densely aligned can increase power factor to a red region in Fig. 3.7. Fabrication and investigation of thermoelectric properties of single crystalline nanotubes are important future works.

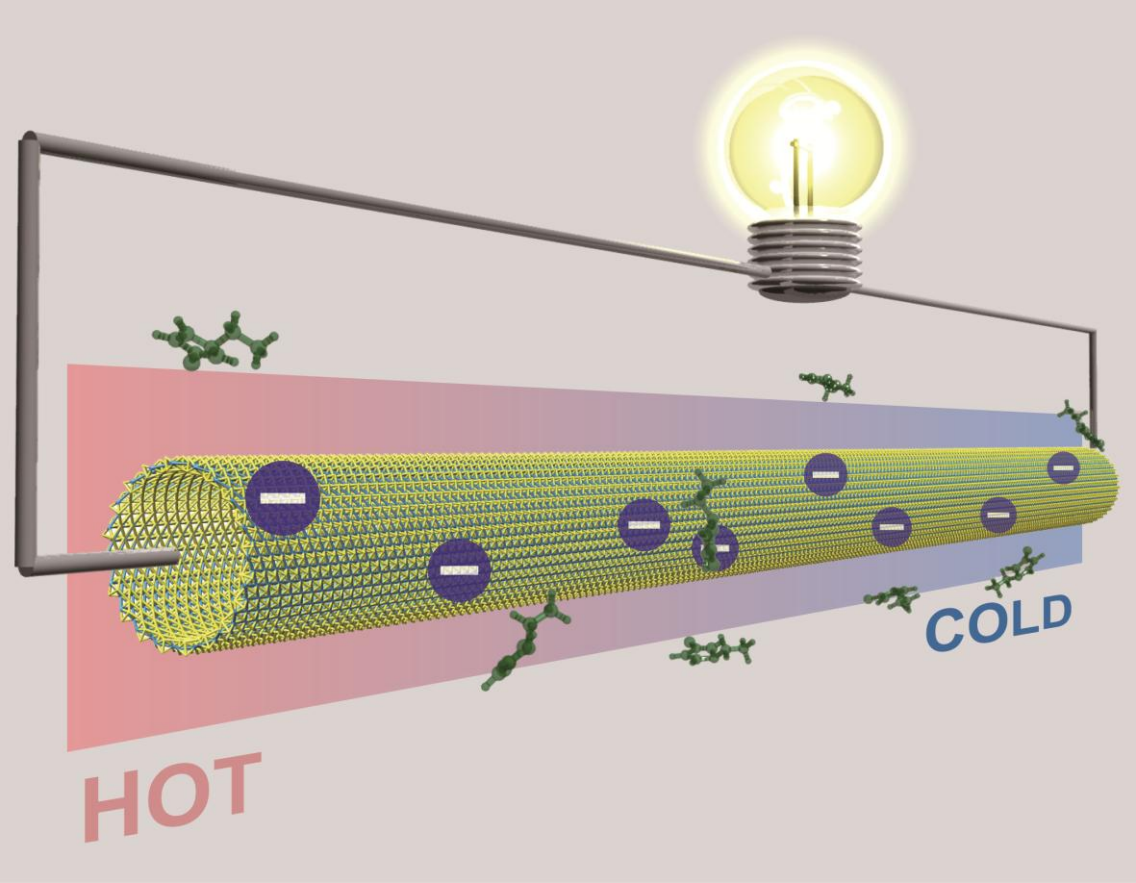

H. Kawai, M. Sugahara, R. Okada, Y. Maniwa, Y. Yomogida, K. Yanagi,
Applied Physics Express, 10, 015001(2017).

Selected as spot light

4 Conclusion and Outlook

In this chapter, I summarize my studies on physical properties of nanotube networks. Summary of my works and future outlook of fabrication of single crystalline SWCNTs and thermoelectric properties of nanotube networks are written in Section 4.1 and Section 4.2, respectively. Finally, I emphasize new findings in my works in Section 4.3.

4.1 Electrical propertied of SWCNTs assembly

Fabrication of aligned SWCNTs array and single crystalline samples with narrow chirality distribution are an important issue for practical application and basic research of SWCNTs. I succeeded to fabricate well aligned SWCNTs assemblies using chirality sorted SWCNTs and the degree of alignment of SWCNTs in the assembly was comparable to the best reported assemblies of aligned array of semiconducting SWCNTs. I observed improvement of device performance of our assembly, but further improvements such as improvement of quality of SWCNTs and using short channel electrodes would be required for realization of metallic conduction and superior device performance.

There are still approaches for fabrication of superior device using as-grown SWCNTs by chemical vapor deposition. Recently, advancement in this approach is reported. In 2013, Jin et al. has reported highly aligned array of as-grown SWCNTs where metallic SWCNTs were completely removed using thermocapillary-enabled purification technique.[145] Device fabricated using this technique exhibited high field effect mobility (>1000 $cm^2/V \cdot S$) with high on /off ratio (>10000), which is best performance in reported data.[145,146] Although their array of SWCNTs is composed only by semiconducting SWCNTs, there is still chirality distribution in the sample. Array of SWCNTs with narrow chirality distribution and high density can improve transistor performance via precise control of current conduction, threshold voltage and hysteresis. Therefore, fabrication of single crystalline SWCNTs with single-chiral state is still ultimate goal in this research community.

Production of single crystalline SWCNTs is also, we assume, required for realization of superconductivity in SWCNTs. In this study, we could not observe a superconductivity of SWCNTs assembly. But, it is reported that the highest transition temperature of SWCNTs is 15 K [29], and it was observed in small diameter SWCNTs. In addition, the transition temperature may be enhanced by applying pressure (e.g. up to

30 – 40 K as in alkali metal doped fullerene) and tuning of the Fermi level[59,60]. Therefore, we believe that superconductivity will be realized if we prepare single crystalline SWCNTs where their diameter, pressure and Fermi level are well controlled.

In 2014, chirality-selective synthesis utilizing specific catalysts was reported. Those technique produce high purity single chirality SWCNTs (> 92 %)[40]. Almost the same time, single-chirality production using specific CNT-cap was reported[147]. In principle, this bottom-up approach can produce only one kind of chirality SWCNTs. Remaining challenge is a mass production of the single-chirality SWCNTs for practical applications. I believe that mass production of single-chirality SWCNTs may someday be realized, and my study here will play a important role for the realization of single crystalline SWCNTs.

4.2 Thermoelectric properties of nanotube networks

One-dimensional materials such as SWCNTs and WS_2 NTs are promising candidates for superior thermoelectric material, but relationships between thermoelectric properties, their chirality, and Fermi level have not been well revealed. I revealed that thermoelectric properties significantly depend on their chirality and Fermi level using electrolyte-gating technique. I also revealed that maximum Seebeck coefficient of metallic SWCNTs was 5 times lower than that of semiconducting SWCNTs. Those results indicate that although we prepared high purity semiconducting SWCNTs sample, there are residual metallic SWCNTs or semiconducting SWCNTs with different charge neutral points. Those SWCNTs may degrade thermoelectric performance of semiconducting SWCNTs. Therefore, I focused on WS_2 NTs as another one-dimensional materials and I investigated its thermoelectric properties. I succeeded to make the WS_2 NT networks conductive states by electrolyte gating methods, and their Seebeck coefficients were firstly evaluated. Finally, we showed that SWCNTs and WS_2 NTs have good potentials for high performance thermoelectric devices, which exceed conventional Bi_2Te_3. Improvement of tube-tube contact and density is important, and, ultimately, preparation of single crystals of nanotubes is required to achieve the highest thermoelectric performance of SWCNT and WS_2 NT.

As another one-dimensional materials, thermoelectric properties of InAs nanowire[148] and Bi_2Te_3 nanowire[149] have been reported. But those nanowires have equal or lower thermoelectric properties compared to their bulk materials, which may be due to the limited ability to control the amount of doping and the carrier concentrations in those nanowires.[149,150] SWCNTs and WS_2 NTs have no dangling bonds, thus their carrier concentration can be tuned by application of electric fields as I showed in this dissertation. In addition, from the point of views for various practical energy conversion applications, nanowire or nanotubes should be aligned because the aligned system can make good electrical contacts between neighboring nanotubes and nanowires and also can improve the packing density. Therefore, preparation of aligned system is an important issue for future work. In the case of SWCNTs, there are many reports on aligned SWCNTs arrays including our work[146]. Recently, He et al. have reported a wafer scale film of aligned SWCNTs[151], which will also be suitable for thermoelectric device fabrication of SWCNTs.

Several new materials with improved *ZT* (e.g. skutterudites and PbTe) have been developed, but progress for commercializing is slow. One of the problems may be mis-matching between the thermoelectric materials and external components in thermoelectric device. Commercially available materials have a thickness from typically 300 μm to several millimeters in order to make good matching of electrical and thermal power impedances to external components.[152] Reduction of material thickness has been proved to be difficult, and how to reduce the thickness is a technically challenging subject. I believe that SWCNTs and WS_2 NTs can solve this problem, thus, I think that nanotube networks have a lot of advantages for commercialization.

4.3 New findings in my works

In this dissertation, as a first step toward the fabrication of single crystals of SWCNTs, I developed a technique to fabricate aligned assemblies of SWCNTs and investigated their electrical properties. In addition, I investigated thermoelectric properties of SWCNTs and WS_2 NTs networks. I found that thermoelectric properties of SWCNT networks are sensitive to their chirality and a position of Fermi level. Particularly, I emphasize that I succeeded to realize a conductive state in WS_2 NT networks and the conductive state can be induced by electrolyte-gating technique. As a result, I succeeded to evaluate the thermoelectric properties of WS_2 NT networks. I showed potentials of SWCNTs and WS_2 NT for superior thermoelectric devices. Future work is

to improve tube-tube junction and densities in the networks and, I think, as a final goal, to fabricate single crystals of the nanotube. SWCNTs and WS_2 NTs can be mono-dispersed into solutions, thus, techniques to make aligned arrays of SWCNTs such as filtration technique[151] can be also applicable on WS_2 NTs. I believe that my works can pave a way for investigation of electronic, thermoelectric properties of nanotube networks, and showed potentials of the nanotube networks for superior thermoelectric devices.

5 Details of theoretical backgrounds and experiments

5.1 Electronic structure of SWCNTs

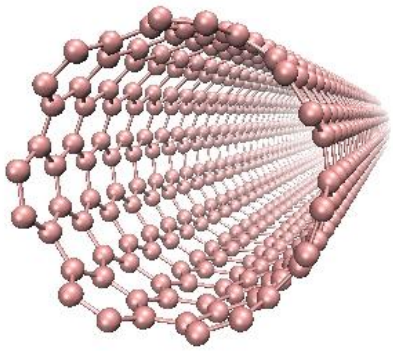

Fig. 5.1 A schematic illustration of SWCNTs[16]

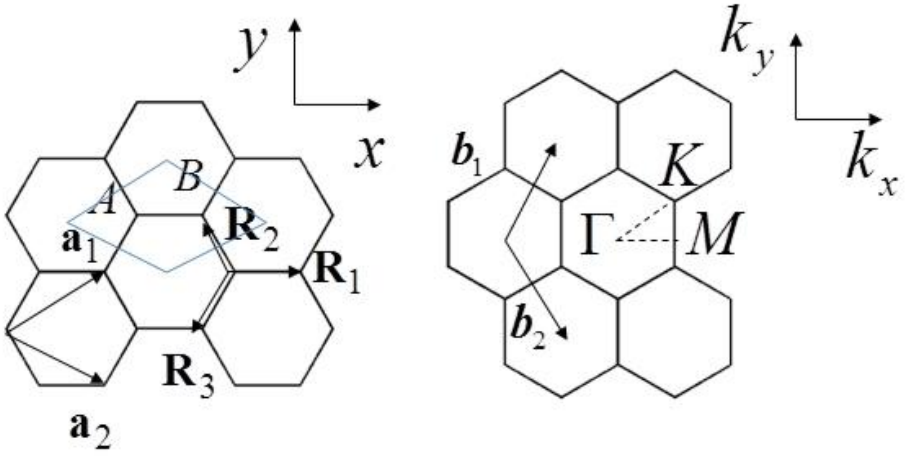

Fig. 5.2 (a) Unit call of graphene. $\mathbf{a}_1$, $\mathbf{a}_2$ and $\boldsymbol{R}_1$, $\boldsymbol{R}_2$, $\boldsymbol{R}_3$, are lattice vector and nearest neighbor vector. (b) Reciprocal lattice vector of graphene. The grey area represents first Brillouin zone.[16]

SWCNTs have a cylindrical structure rolling up graphene sheet as shown in Fig. 5.1. Electronic structure of SWCNT can be derived from that of graphene. In Fig. 5.2 the unit cell and Brillouin zone of graphene are shown. $\mathbf{a}_1$, $\mathbf{a}_2$ and $\mathbf{b}_1$, $\mathbf{b}_2$ are lattice vectors

and reciprocal lattice vectors of the hexagonal lattice, respectively.

$$\mathbf{a}_1 = \left(\frac{\sqrt{3}}{2}a, \frac{a}{2}\right), \quad \mathbf{a}_2 = \left(\frac{\sqrt{3}}{2}a, -\frac{a}{2}\right) \tag{5.1}$$

$$\mathbf{b}_1 = \left(\frac{2\pi}{\sqrt{3}a}, \frac{2\pi}{a}\right), \quad \mathbf{b}_2 = \left(\frac{2\pi}{\sqrt{3}a}, -\frac{2\pi}{a}\right) \tag{5.2}$$

Where $a = |\mathbf{a}_1| = |\mathbf{a}_2| = 2.46\text{Å}$ is the lattice constant. To dispersion relations of π band of graphene, we consider linear combination of Bloch wave function of the A and B sites,

$$\Psi_\pi(\mathbf{k},\mathbf{r}) = \sum_{i=A,B} C_i \Phi_i(\mathbf{k},\mathbf{r}) \tag{5.3}$$

$$\Phi_i(\mathbf{k},\mathbf{r}) = \frac{1}{\sqrt{N}} \sum_{R}^{N} e^{i\mathbf{kR}} \phi_i(\mathbf{r}-\mathbf{R}) \tag{5.4}$$

Where $\Phi_i(\mathbf{k},\mathbf{r})$ is Bloch wave function, $\phi_i(\mathbf{r}-\mathbf{R})$ is atomic wave function, N is the number of unit cell in the crystal. The Schrodinger equation is

$$H_{crystal}\Psi_\pi = E_{2g}(\mathbf{k})\Psi_\pi \tag{5.5}$$

To get eigenvalue of the Ψ_π, we calculate transfer integral matrix and overlap integral matrix given by

$$H_{XX'} = \frac{1}{N}\sum_{R,R'} e^{ik(R-R')} < \phi_X(r-R') | H_{crystal} | \phi_{X'}(r-R) > \tag{5.6}$$

$$S_{XX'} = \frac{1}{N}\sum_{R,R'} e^{ik(R-R')} < \phi_X(r-R') | \phi_{X'}(r-R) > \tag{5.7}$$

In the case of H_{AA}

$$H_{AA} = \frac{1}{N}\sum_{R,R'} e^{ik(R-R')} < \phi_A(r-R') | H_{crystal} | \phi_A(r-R) > \tag{5.8}$$

The integral in (5.7) is large when $R = R'$ so that we take only

$$H_{AA} = \frac{1}{N} < \phi_A(r-R') | H_{crystal} | \phi_A(r-R') >= \varepsilon_{2p} \tag{5.9}$$

ε_{2p} is energy of $2p_z$-orbital of carbon. In the case of H_{AB}, we can take a nearest neighbor R_1, R_2, R_3,

$$\begin{aligned} H_{AB} &= \frac{1}{N}\sum_{R'=R_1,R_2,R_3} e^{ikR'} < \phi_A(r-R') | H_{crystal} | \phi_B(r-R) > \\ &= t(e^{ikR_1} + e^{ikR_2} + e^{ikR_3}) = tf(k) \end{aligned} \tag{5.10}$$

Where

$$t = < \phi_A(r-R') | H_{crystal} | \phi_B(r-R) > \tag{5.11}$$

$$R_1 = \left(\frac{a}{\sqrt{3}}, 0\right), \quad R_2 = \left(-\frac{a}{2\sqrt{3}}, \frac{a}{2}\right), \quad R_3 = \left(-\frac{a}{2\sqrt{3}}, -\frac{a}{2}\right) \tag{5.12}$$

Substituting (5.12) to (5.10), we obtain

$$f(k) = e^{ik_x a/\sqrt{3}} + 2e^{-ik_x a/2\sqrt{3}} \cos\left(\frac{k_y a}{2}\right) \tag{5.13}$$

Using a relationship

$$\begin{aligned} H_{AA} &= H_{BB} \\ H_{AB} &= H_{BA}^{*} \\ S_{AA} &= S_{BB} = 1 \\ S_{AB} &= S_{BA}^{*} = sf(k) \\ s &= <\phi_A(r-R') \mid \phi_B(r-R)> \end{aligned} \tag{5.14}$$

the transfer integral matrix and overlap matrix are

$$H = \begin{pmatrix} \varepsilon_{2p} & tf(k) \\ tf(k)^{*} & \varepsilon_{2p} \end{pmatrix}, \quad S = \begin{pmatrix} 1 & sf(k) \\ sf(k)^{*} & 1 \end{pmatrix} \tag{5.15}$$

Solving the secular equation det $(H - ES) = 0$, the eigenvalues $E_{2g}(\mathbf{k})$ are obtain as a function of $w(\mathbf{k})$,

$$E_{2g}(\mathbf{k}) = \frac{\varepsilon_{2p} \pm tw(\mathbf{k})}{1 \pm sw(\mathbf{k})} \tag{5.16}$$

$$w(\mathbf{k}) = \sqrt{1 + 4\cos\frac{\sqrt{3}k_x a}{2}\cos\frac{k_y a}{2} + 4\cos^2\frac{k_y a}{2}} \tag{5.17}$$

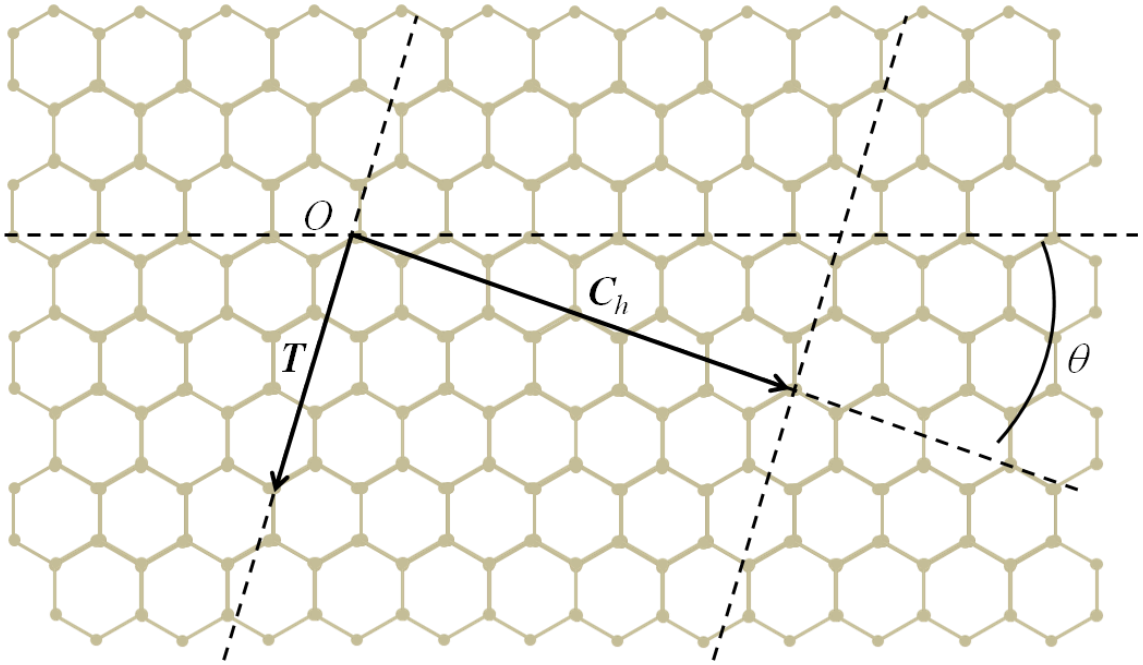

Fig. 5.3 The unit cell of unrolled carbon nanotubes. C_h and T are chral vector and translational vector and θ is chral angle.

Here we consider a unite cell of SWCNT as shown in Fig. 5.3. C_h and T are called chiral

vector and translational vector, respectively,

$$C_h = n\mathbf{a_1} + m\mathbf{a_2} \equiv (n,m) \tag{5.18}$$

$$T = t_1\mathbf{a_1} + t_2\mathbf{a_2} \equiv (t_1,t_2)$$

$$t_1 = \frac{2m+n}{d_R}, t_2 = -\frac{2n+m}{d_R} \tag{5.19}$$

Integer m and n are called chiral index, which determine the structure of SWCNTs. The reciprocal lattice vector corresponding to C_h and T_h are given by

$$\mathbf{K}_1 = \frac{1}{N}(-t_2\mathbf{b_1} + t_1\mathbf{b}_2)$$

$$\mathbf{K}_2 = \frac{1}{N}(-t_2\mathbf{b_1} + t_1\mathbf{b}_2), \tag{5.20}$$

The length of the vectors is

$$|\mathbf{K}_1| = \frac{2}{d}, |\mathbf{K}_2| = \frac{2\pi}{T}, \tag{5.21}$$

The energy is quantized along K_1 direction due to presence of periodic boundary condition along circumference direction of SWCNTs. Wave vector is discretized along K_1 direction and the interval is $|\mathbf{K}_1|$. Therefore, the dispersion relation of SWCNT is expressed by

$$E_\mu(k) = E_{2g}(k\frac{\mathbf{K}_2}{|\mathbf{K}_2|} + \mu\mathbf{K}_1),$$

$$(\mu = 0,\cdots,N-1, -\frac{\pi}{T} < k < \frac{\pi}{T}) \tag{5.22}$$

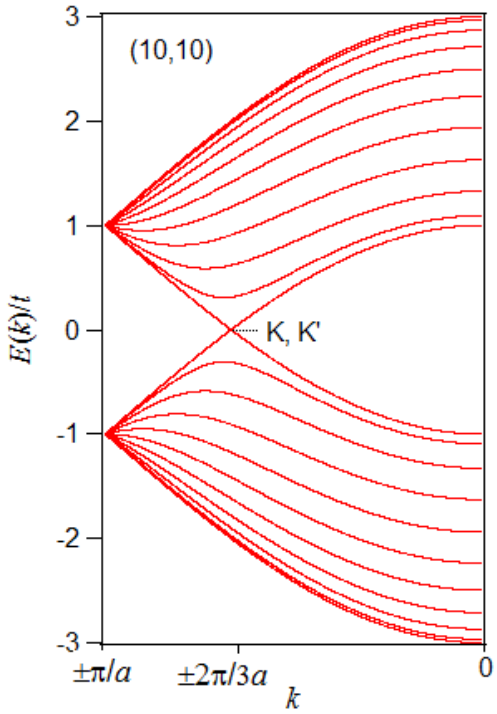

Fig. 5.4 Dispersion relation of (10,10) SWCNTs

In Fig. 5.4 dispersion relation of (10,10) SWCNTs are shown. In the situation where the $\mathbf{K}_2$ vector across the K point, the energy dispersion is closed at K point, which called metallic type of SWCNT. A condition of chiral index in order to form a metallic type of SWCNT is given by

$$n - m = 3s \ (s \text{ is integer}) \tag{5.23}$$

A density of states of SWCNT is given by

$$D(E) = \frac{T}{2\pi N} \sum_{\pm} \sum_{\mu=1}^{N} \int \frac{1}{\left| \frac{dE_{\mu}^{\pm}}{dk} \right|} \delta(E_{\mu}^{\pm}(k) - E) dE \tag{5.24}$$

The density of states of metallic and semiconducting type of SWCNT are shown in Fig. 5.5. There are sharp peaks, which called Van Hove singularity.

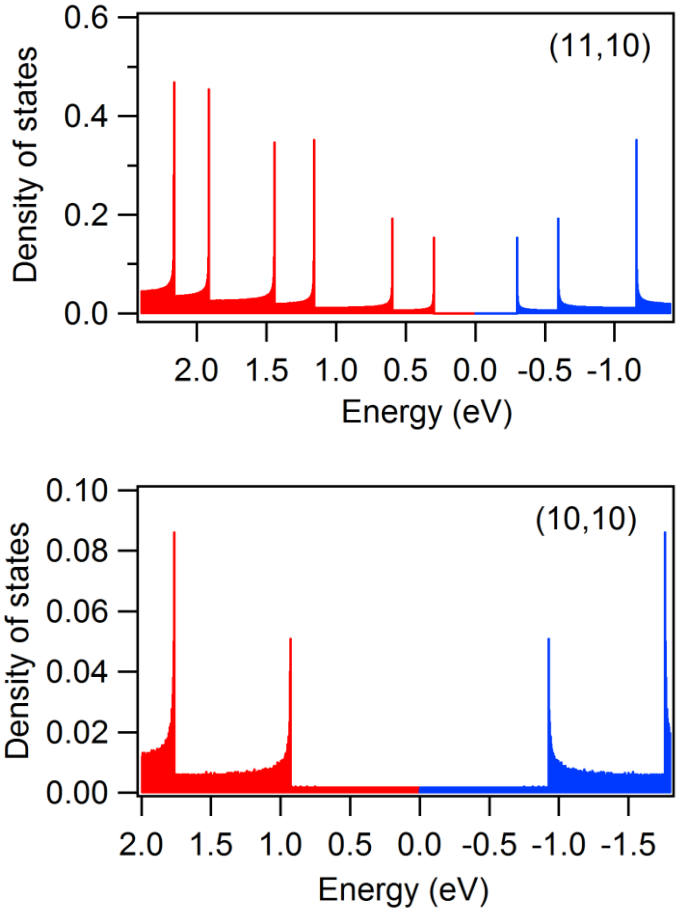

Fig. 5.5 The density of state of SWCNTs.

5.2 Preparation of SWCNT samples

5.2.1 Separation of SWCNTs by density gradient sorting

Semiconducting and metallic SWCNTs with diameters of 1.4 nm were prepared from standard density-gradient sorting processes from SWCNTs samples produced by Arc discharge method (Arc SO, Meijo nano Co.). We dissolved pristine sample in 2 % (w/w) Sodium Deoxy cholate (DOC, Wako Co.) solution. To prepare well suspended SWCNTs, the solution was homogenized with tip-type homogenizer (Branson Sonifier 250 D, 17 W) for 8 hours and ultracentrifuged for 2~3 hours at 36,000 rpm (P40ST, Hitachi Koki Co.), then supernatants were collected. Density gradient were created in seal tube (HITACHI Koki Co., 40 ml) using iodixanol and surfactants as shown in Fig. 5.6 (a). The seal tube was ultracentrifuged for 9 hours at 50,000 rpm. After centrifugation there were metallic and semiconducting SWCNTs layers in density gradient solution

as shown in Fig. 5.6 (b).

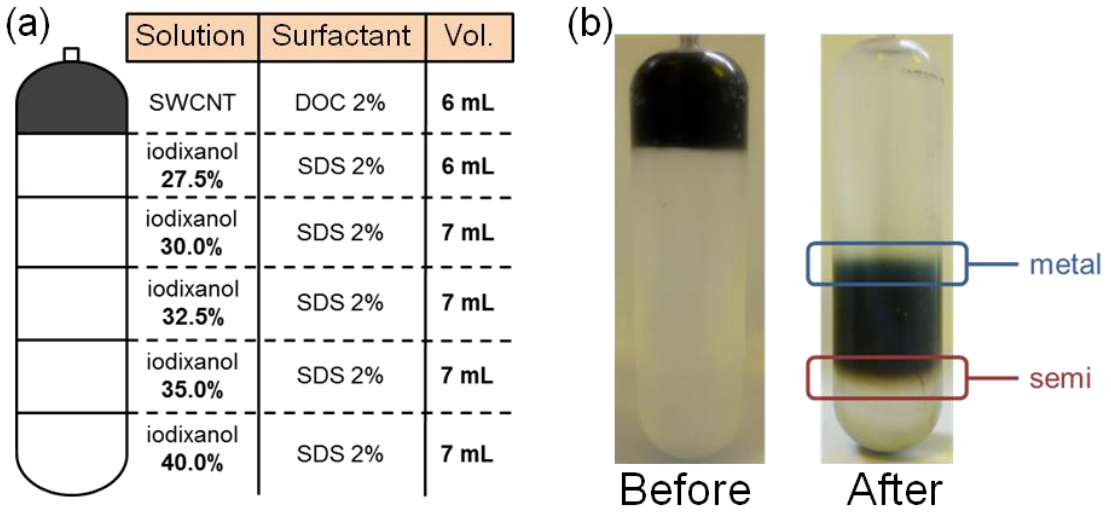

Fig. 5.6 (a) A Schematic illustration of density gradient in seal tube. (b) Photograph of seal tube filled with SWCNTs solution and density gradient solution.

5.2.2 Separation of SWCNTs by gel chromatography

Fig. 5.7 shows schematic procedure of (6,5) extraction from CoMoCAT (Ardrich Co.) by gel chromatograph. (a) a gel (Sephacryl S-200 HR, GE Healthcare) were put in to a column. (b) the gel contain ethanol to avoid drying, thus the ethanol were exchanged by water. (c) the water was replaced by 2wt% SDS solution. (d) CoMoCAT suspended in 2wt% SDS solution were loaded on the gel and pushed into bottom of the column using N_2 gas. In this procedure, semiconducting SWCNTs are strongly absorbed into the gel. (e) To remove the metallic SWCNTs, 2.5 wt% SDS solution were applied on the gel and pushed into the bottom. (f) Finally, (6,5) SWCNTs were collected by applying 5.0 wt% SDS on the gel.

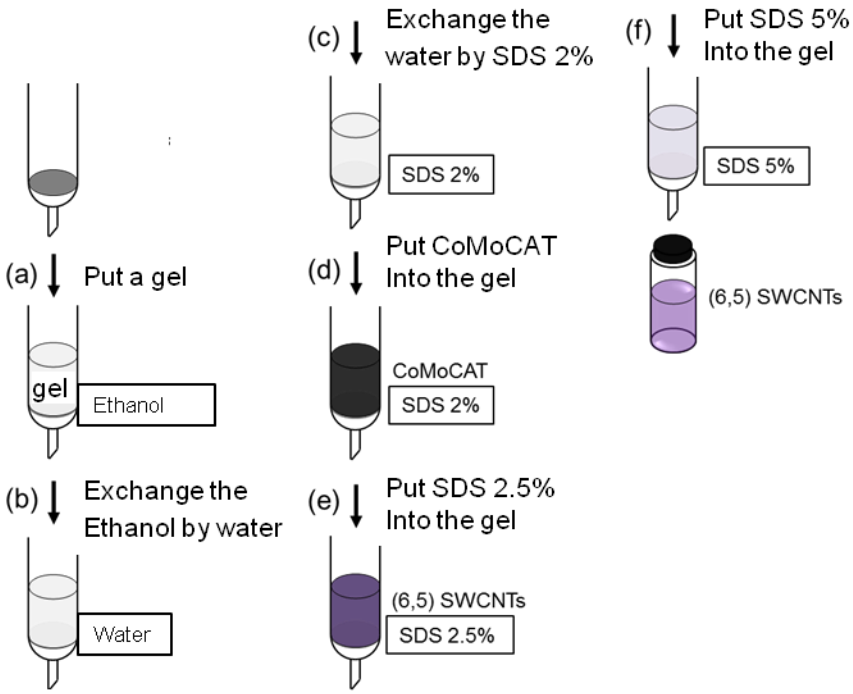

Fig. 5.7 Experimental procedure of gel chromatography.

5.2.3 Preparation of thin film of SWCNTs

SWCNTs dispersed in solution with surfactant or some regents were purified through vacuum filtering processes as shown in Fig. 5.8 (a). First, (i) the solution was mixed with methanol in a vial to make the SWCNTs bundled, then (ii) the solution was filtered through vacuum filtration using membrane filter (PTFE, pore size = 0.2 μm). After the SWCNTs were trapped on the membrane filter, we usually add hot water to remove residual surfactant in the filter. Then (iii) the filter was put into the vial and dispersed with ethanol using bus-type sonication. We performed the procedure (i) – (iii) three times. After finish the procedure we did same procedure three times again using toluene as solvent of SWCNTs. In this procedure we must not use hot water after SWCNTs were trapped in the membrane filter because toluene is hydrophobic. After we finished the procedure using toluene, SWCNTs were mixed methanol again and filtered using membrane filter (nitrocellulose, pore size = 0.2 μm). The filter is shown in Fig. 5.8 (b).

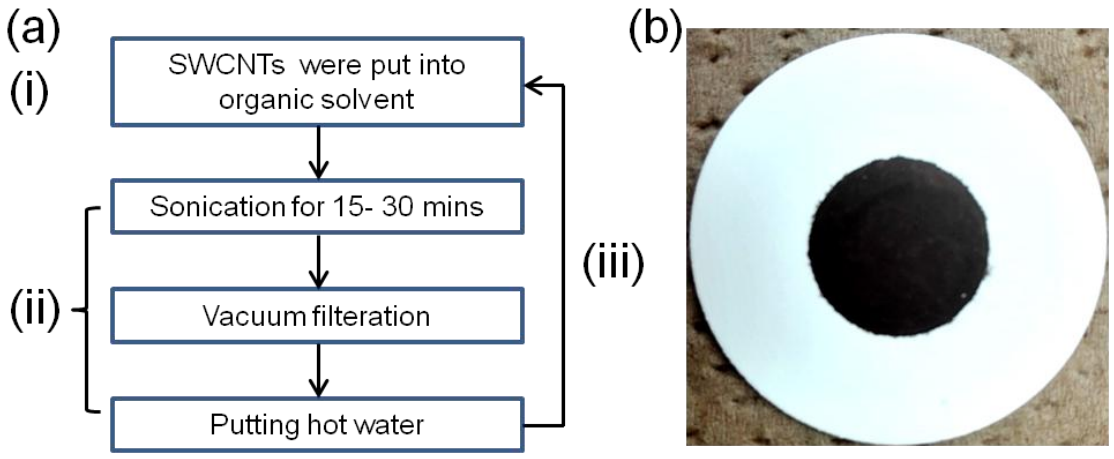

Fig. 5.8 (a) A procedure of film preparation. (b) SWCNTs trapped on the membrane filter.

5.2.4 Optical characterization of SWCNT

Fig. 5.9 (a) shows absorption spectrum of semiconducting and metallic SWCNTs with average diameter of 1.4 nm dispersed in solution with surfactants. There are peaks around 1000 nm and 700 nm for semiconducting and metallic SWCNTs, which corresponds to E_{22} transition of semiconducting SWCNTs and E_{11} transition of metallic SWCNTs. Fig. 5.9 (b) shows absorption spectrum of (6,5) enriched SWCNTs. The peak around 570 nm and 990 nm corresponds E_{22} and E_{11} transition of (6,5) SWCNTs. Fig. 5.10 shows Raman spectrum of (a) ArcSO and (b) (6,5) SWCNTs. Inset shows RBM spectrum and the peak position was 162.8 cm^{-1} for ArcSO and 313.5 cm^{-1} for (6,5) SWCNTs. In the case of SWCNTs the peak position of RBM is known to inversely proportional to the diameter d [nm],

$$\omega_{peak} = \left(\frac{248}{d} \right) \ [\mathrm{cm}^{-1}] \qquad (5.25)$$

In the case of our sample, the diameter was evaluated to be 1.52 nm for ArcSO and 0.79 nm for (6,5) SWCNTs. The peak around 1600 cm^{-1} shows G-band of the SWCNTs and the peak is also seen in the case of graphite. But in the case of CNT this peak split into two peaks, which are called G_+ at 1590 cm^{-1} and G_- mode at 1570 cm^{-1}. The peak around 1350 cm^{-1} is called D band, which originates from vacancy of carbon atoms. The peak ratio of G_+ / D is often used to evaluate the purity of CNT sample.

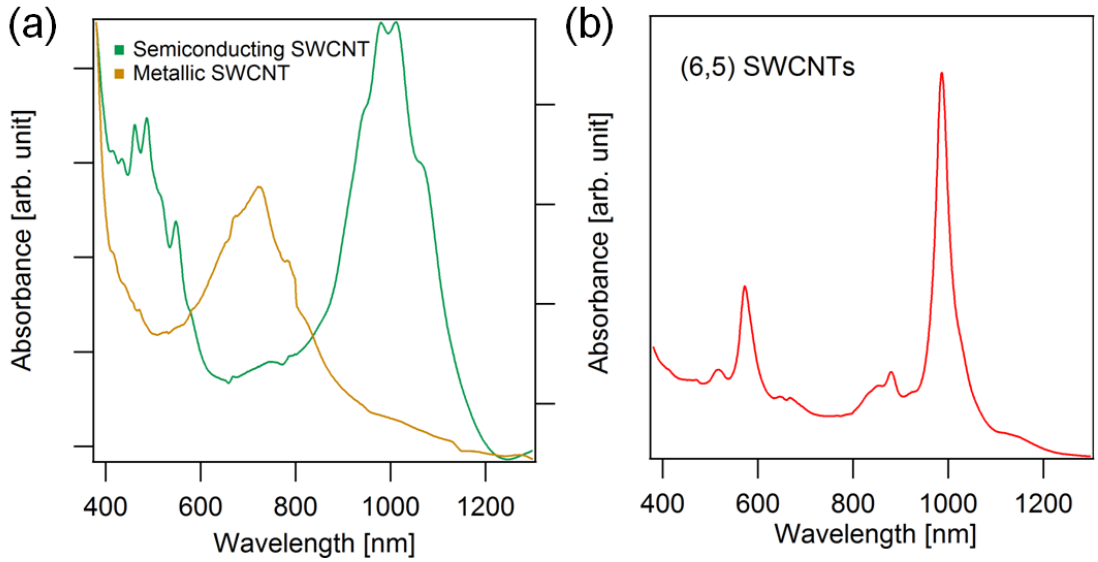

Fig. 5.9 (a) Optical absorption spectrum of semiconducting and metallic SWCNTs. Green line and yellow line represents semiconducting and metallic SWCNTs. (b) Optical absorption spectrum of (6,5) enriched SWCNTs.

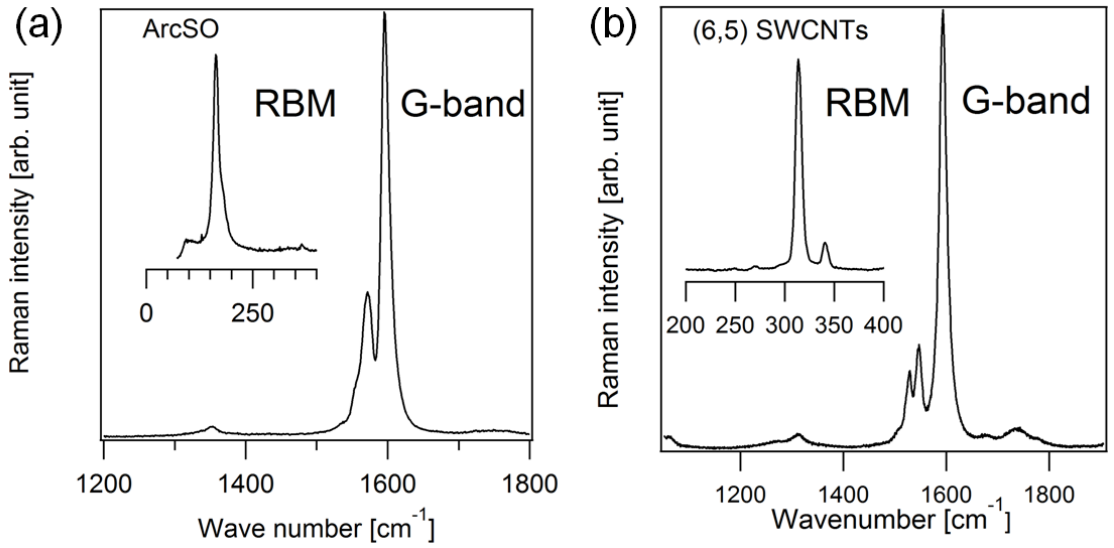

Fig. 5.10 Raman spectrum of (a) ArcSO and (b) (6,5) enriched SWCNTs. The Excitation wavelength was 488 nm.

5.3 Preparation of WS_2 NT sample

5.3.1 Preparation of WS_2 NT film

To prepare well suspended WS_2 NTs, powder of WS_2 NTs were dispersed in CHP (1-Cyclohexyl-2-pyrrolidone) using bus-type sonication, then solvent was exchanged to

toluene and we performed vacuum filtration using a membrane filter (PTFE, pore size = 10.0 μm) to prepare WS_2 NTs film. The thin film of WS_2 NTs on membrane filter is shown in Fig. 5.11 (a). Freestanding buckypaper is shown in Fig. 5.11 (b).

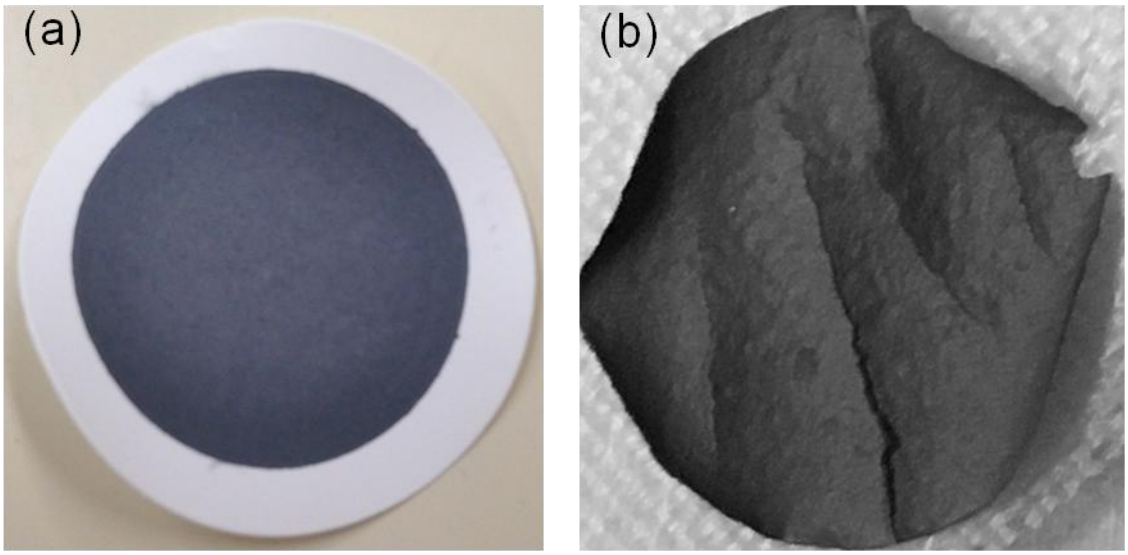

Fig. 5.11 (a) Thin film of WS_2 NTs on membrane filter.
(b) Freestanding buckypaper of WS_2 NTs.

5.3.2 Optical characterization of WS_2 NTs

Fig. 5.12 shows Raman spectra of WS_2 NTs. There are peaks at 351 cm^{-1} and 420 cm^{-1}, which comes from vibrational modes of WS_2 sheet. Fig. 5.13 shows optical absorption spectra of WS_2 NTs. There are peaks at 1.9 and 2.3 eV, which corresponds A and B transitions of WS_2 sheet, respectively.

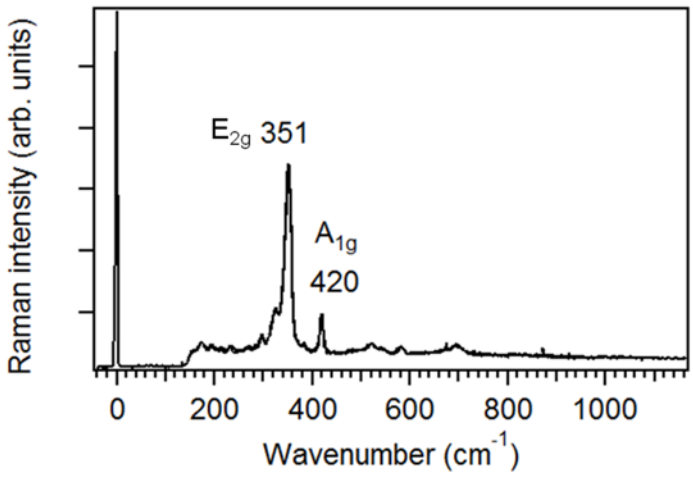

Fig. 5.12 Raman spectra of WS_2 NTs. The peaks at 351 cm^{-1} and 420 cm^{-1} comes from

E_{2g} and A_{1g} modes of WS_2 sheet, respectively.

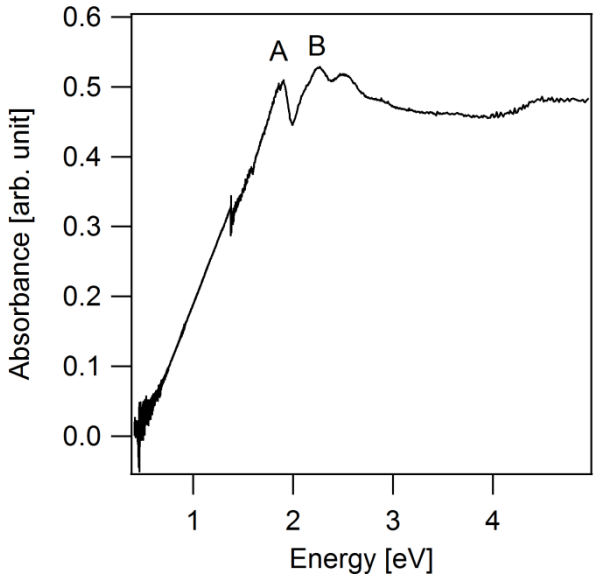

Fig. 5.13 An absorption spectrum of WS_2 NTs.

5.3.3 Characterization of WS_2 NTs by TEM

Fig. 5.14 (a) and (b) show a transmission electron microscope (TEM) image of the WS_2 NTs we used. The value of d_{outer} / d_{inner} was estimated to be 2.45 from Fig. 5.14 (b). Fig. 5.14 (c) shows a histogram of the d_{outer} of WS_2 NTs. The mean d_{outer} was found to be 135 nm and approximately 63 % of samples are distributed within 50 – 150 nm. Using the value of d_{outer} / d_{inner} and mean d_{outer}, the mean thickness of layers was estimated to be approximately 40 nm, which corresponds to approximately 40 layers.

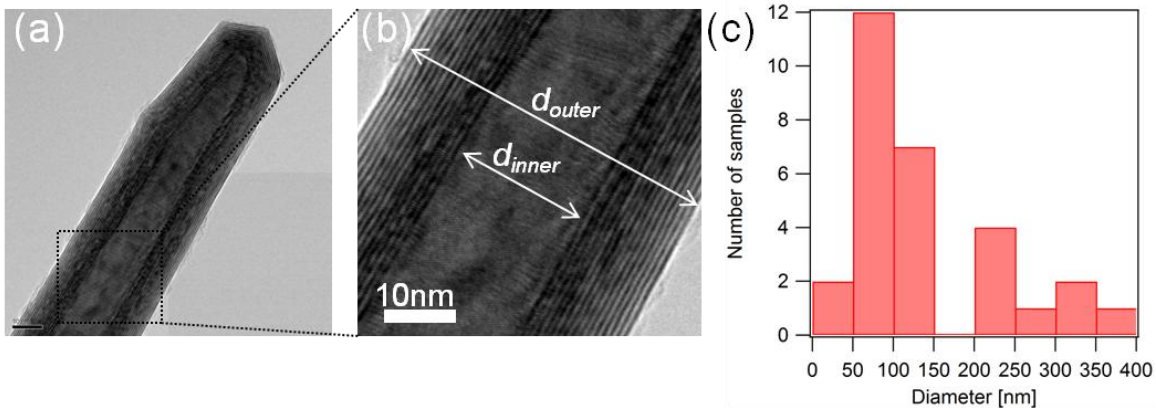

Fig. 5.14 (a), (b) Transmission electron microscope images of the WS_2 NTs. (c) Histogram of the diameter of WS_2 NTs evaluated from 30 samples. (Copyright 2017 The Japan Society of Applied Physics)

5.4 Electrolyte gating

5.4.1 Principle of electric double layer

As shown in Fig. 5.15, in a case that there are two electrodes in a electrolyte solution, when a voltage is applied between the two electrodes the ions move along the electric field to screen the field, and then the ions form a layer on the surface of the electrodes. The layer is called electric double layer. According to a parallel plate capacitor model, the capacitance can be written as:

$$C = \frac{\varepsilon_0 \varepsilon_r A}{d} \tag{5.26}$$

Where ε_0 and ε_r are the vacuum and relative permittivities, respectively. A is the area of the prates and d is distance between the two plates. For example, capacitance of a 300 nm thickness of SiO_2 is ~ 10 nF/cm^2. In the case of electric double layer, the capacitance is ~ 10 μF/cm^2, which is three orders of magnitude greater than conventional SiO_2. This originates from the thickness of the electric double layer, which is sub-nanometer scale.

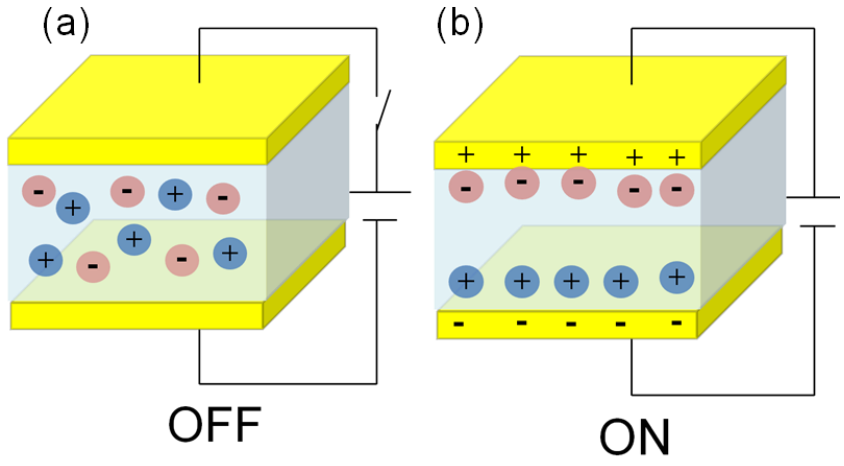

Fig. 5.15 A schematic illustration of electric double layer. Red and blue ball represents anion and cation, respectively. (a) and (b) show on-state and off-state of the power.

5.4.2 Field effect transistor

Here, we illustrate a principle of field effect transistor using electrolyte as gate material. Fig. 5.16 shows schematic illustration of field effect transistor. Configuration is similar to a parallel plate capacitor as discussed previous section. A source and drain electrodes are attached to both ends of the channel material and a gate voltage is applied from the gate electrode to the channel. A souce-drain voltage is applied from

the source to the drain electrode. In the case of N-type semiconductor, when electrons are injected in the channel material, drain current become on-state above threshold voltage as illustrated in the bottom of Fig. 5.16 (a). Fig. 5.16 (c) shows a schematic illustration of potential drops in the ionic liquid as a function of distance from the gate electrode to the channel. There are potential drops at the surface of the gate electrode and the channel due to presence of electric double layer formations on both surfaces. Actual voltages applied to the channel were evaluated from the reference voltage V_R.

Recently, control of carrier concentration by electric double layer has attracted a lot of attentions. For example, low voltage operation of FET[76], phase transition in bulk system[153], electric field induced superconductivity[154,155], and control of transition temperature of superconductivity[156] were realized using electric double layer techniques. An advantage of this type of technique is controllability and reversibility of the amount of carriers. Therefore, one can investigate physical properties of materials as a function of the amount of injected carriers. This technique enables us to obtain comprehensive understanding of physical properties of materials such as electronic properties and thermoelectric properties.

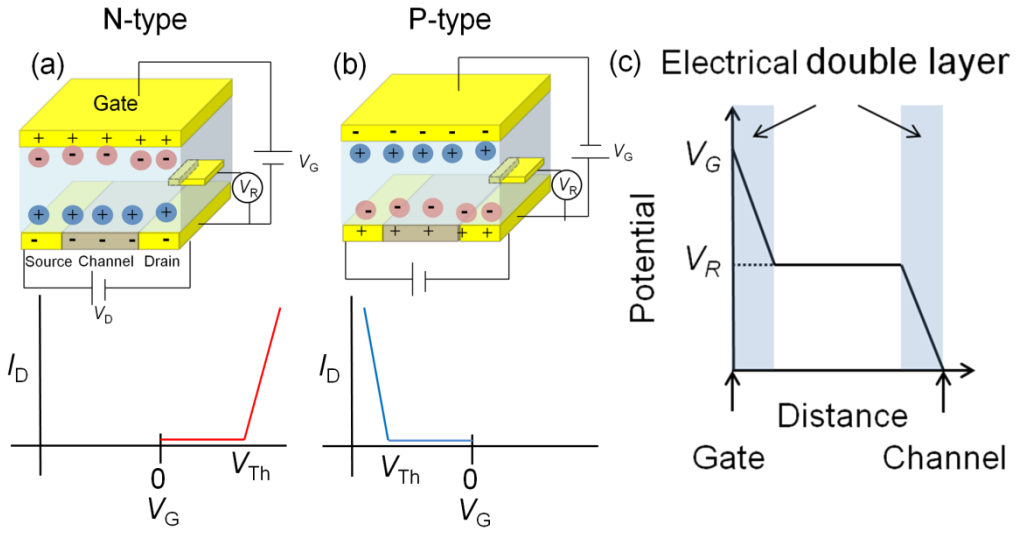

Fig. 5.16 Schematic illustration of field effect transistor using electrolyte as gate material. (c) shows schematic illustration of relationship between potential drop and distance.

5.4.3 Determination of threshold voltages in transfer characteristics of WS_2 NTs

Fig. 5.17 shows transfer characteristics of WS_2 NT networks using electrolyte gating

technique. The I_{sd} and V_R represent drain current and reference voltage, respectively. To determine the threshold voltage, we extrapolated the I_{sd} - V_R curve to zero as shown in Fig. 5.17 (a). Taking into account the hysteresis in the transfer curve, we averaged the value of threshold voltage using value of forward and backward. The width of threshold voltage between electron and hole region was estimated to be 2.57 ± 0.07 V using 3 devices as shown in Fig. 5.17 (a)-(c).

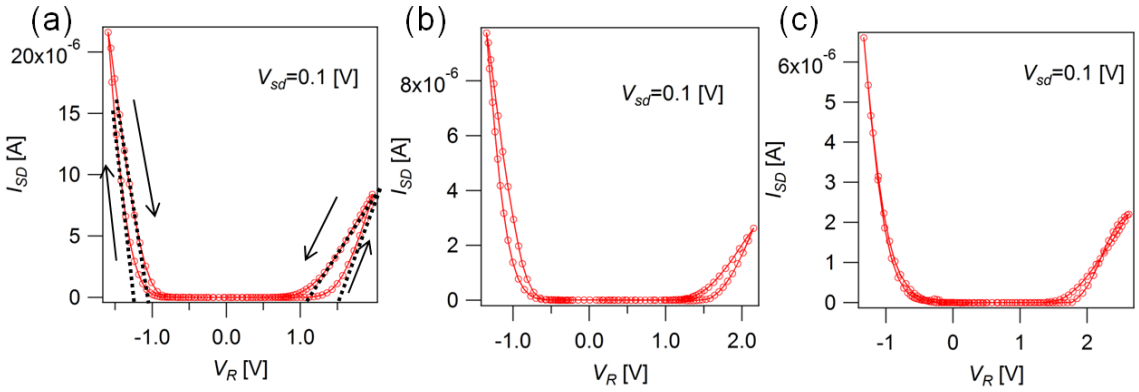

Fig. 5.17 Transfer characteristics of WS_2 NT networks.
(Copyright 2017 The Japan Society of Applied Physics)

5.5 Electrical transport

5.5.1 Variable range hopping model

In disordered systems like an amorphous semiconductor, it has been known that electrical transport mechanisms differ from an ordered system like a single crystal. Mott noted that at a sufficiently low temperature hopping conduction results from localized states concentrated near Fermi level.[112,113] He showed the temperature dependence of resistivity is

$$\rho(T) = \rho_0 \exp\left[\left(\frac{T_0}{T}\right)^{\frac{1}{4}}\right] \tag{5.27}$$

$$T_0 = \frac{\beta}{k_B D(\mu) a^3} \tag{5.28}$$

k_B is Boltzmann constant $D(\mu)$ is density of states at Fermi level, a is the localization radius of states near Fermi level, β is a numerical constant. For three dimensional system $\beta = 21.2$. The derivation is follow.

An electrical resistivity between two states of spatial separation R and energy separation E is given by

$$\rho = \rho_0 \exp\left[\frac{2R}{a} + \frac{E}{k_B T}\right] \tag{5.29}$$

The first term results from a probability of transfer between the two states. Here, consider the localized states within energy E_0 at Fermi level μ. The concentration of states within E_0 is given by

$$N(E_0) = 2D(\mu)E_0 \tag{5.30}$$

The typical separation of the two sites R in the energy band is given by

$$\left[N(E)\right]^{-1/3} \tag{5.31}$$

thus electrical resistivity between the two states in the band is

$$\rho = \rho_0 \exp\left[\frac{1}{N^{1/3}(E_0)a} + \frac{E_0}{k_B T}\right] = \rho_0 \exp\left[\frac{1}{\left[D(\mu)E_0\right]^{1/3} a} + \frac{E_0}{k_B T}\right] \tag{5.32}$$

(5.32) has sharp minimum at

$$E_0 = \frac{(k_B T)^{3/4}}{\left[D(\mu)a^3\right]^{1/4}} \tag{5.33}$$

Substituting (5.33) to (5.32) we can obtain (5.27) and (5.28), but we can't obtain the β in this argument. To generalize (5.27) for the case of an arbitrary spatial dimensionality d, we can replace (5.31) by $\left[N(E)\right]^{-1/d}$, thus (5.27) becomes

$$\rho(T) = \rho_0 \exp\left[\left(\frac{T_0}{T}\right)^{\frac{1}{d+1}}\right] \tag{5.34}$$

$$T_0 = \frac{\beta_d}{k_B D(\mu) a^d} \tag{5.35}$$

$$\beta_{d=2} = 13.8 \tag{5.36}$$

5.5.2 Hall effect

Consider a current-flow in a conductor and magnetic field perpendicular to the current. The magnetic field deflects electrons in the negative y direction by Lorentz force. As they accumulate there, an electric field builds up in the –y direction that opposes the motion of the electrons. In equilibrium state, the field will balance the Lorentz force,

$$\begin{aligned} e v_x H &= e E_y \\ v_x &= \frac{E_y}{H} \end{aligned} \tag{5.37}$$

Here, j_x is,

$$j_x = -nev_x \tag{5.38}$$

Substituting (5.38) to (5.37), we can get

$$-\frac{1}{ne} = \frac{E_y}{Hj_x} \equiv R \tag{5.39}$$

R is called Hall coefficient. Here, we rewrite (5.39) using

$$\begin{aligned} V_y &= wE_y \\ I_x &= wh \cdot j_x \end{aligned} \tag{5.40}$$

Where w is width of the sample, h is thickness of the sample, then we can get Hall voltage,

$$V_y = \frac{HI_x}{neh} \tag{5.41}$$

5.6 Details of crystal template method

5.6.1 Preparation of crystal template

To form the template, crystals of DOC were prepared by a re-crystallization method. A 2 ml solution of 1 % DOC (w/w) was heated in a vial to 100 ºC in an incubator (EOP-300B, ETTAS Co.) for 20 h. Then, needle-like crystals of DOC were formed in the solution as shown in Fig. 5.18. When the concentration of DOC was greater than 5 % (w/w) or less than 0.5 % (w/w), needle-like crystals were not observed. 1-2 % (w/w) DOC was appropriate for production of the crystals.

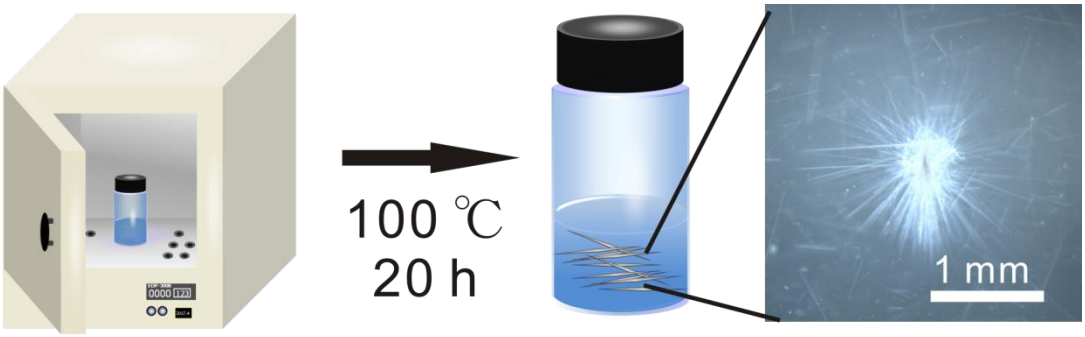

Fig. 5.18 Schematic illustration of re-crystallization method.
(Copyright 2014 AIP Publishing LLC)

5.6.2 Details of procedure of crystal template method

First, substrate (SiO_2 (100 nm)/Si) was washed by acetone reflux process. The substrate was placed on a styrol case. The liquid of the SWCNTs solution were

dispensed onto the substrate and the amount of the solution was 1 - 2 μl as shown in Fig. 5.19 (a). Then, The needle-like crystals of DOC were immediately inserted into the droplet and as shown in Fig. 5.19 (b). Then, the styrol case was sealed by a tape as shown in Fig. 5.19 (c) and put into an incubator at 15 - 20 °C.

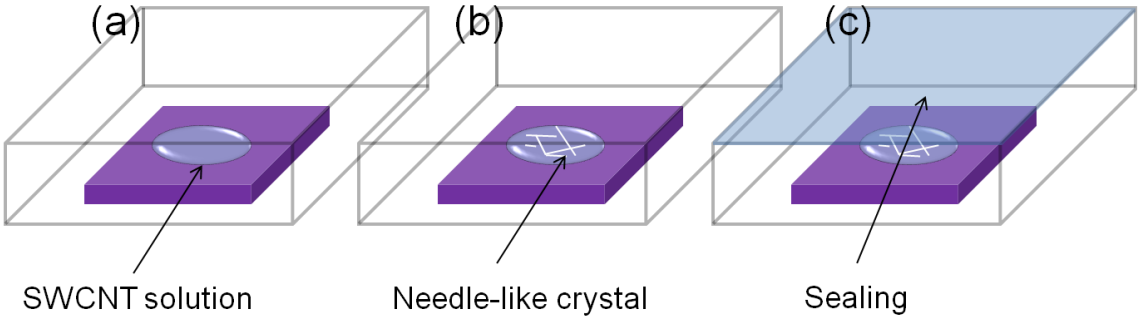

Fig. 5.19 A schematic illustration of experimental procedure

1 – 3 hours later, after evaporation of the solution we performed polarized Raman spectroscopy to find the sample with good alignment. The photograph of the substrate after evaporation of the solution is shown in Fig. 5.20. We can usually find the sample with alignment ratio I_{max} / I_{min} = 7 – 12. If we find a sample with good alignment ratio another samples are carefully removed using wet tissue as shown in Fig. 5.21 (a) and (b). The substrate was soaked in acetone as shown in Fig. 5.21 (c) and the vial was sealed to avoid an evaporation of the acetone solution.

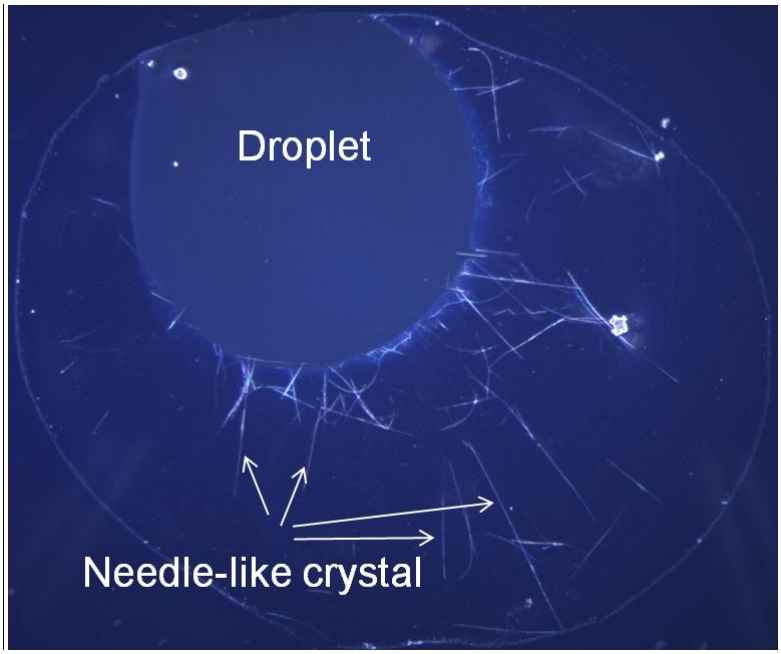

Fig. 5.20 The photograph of the substrate after evaporation of the solution.

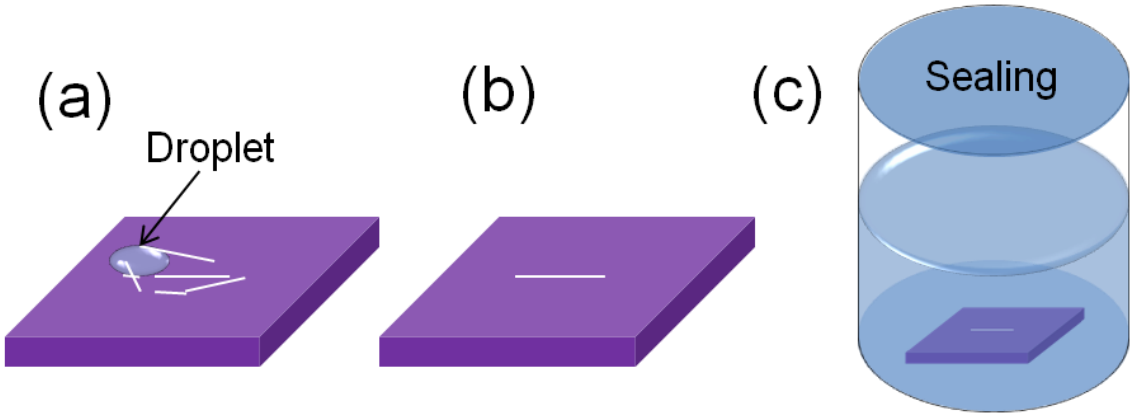

Fig. 5.21 A schematic illustration of acetone washing.

We usually confirm the removal of the DOC using image of the substrate as shown in Fig. 5.22. Before the acetone washing the needle-like DOC crystal looks black in Fig. 5.22. After the acetone washing the crystal looks white.

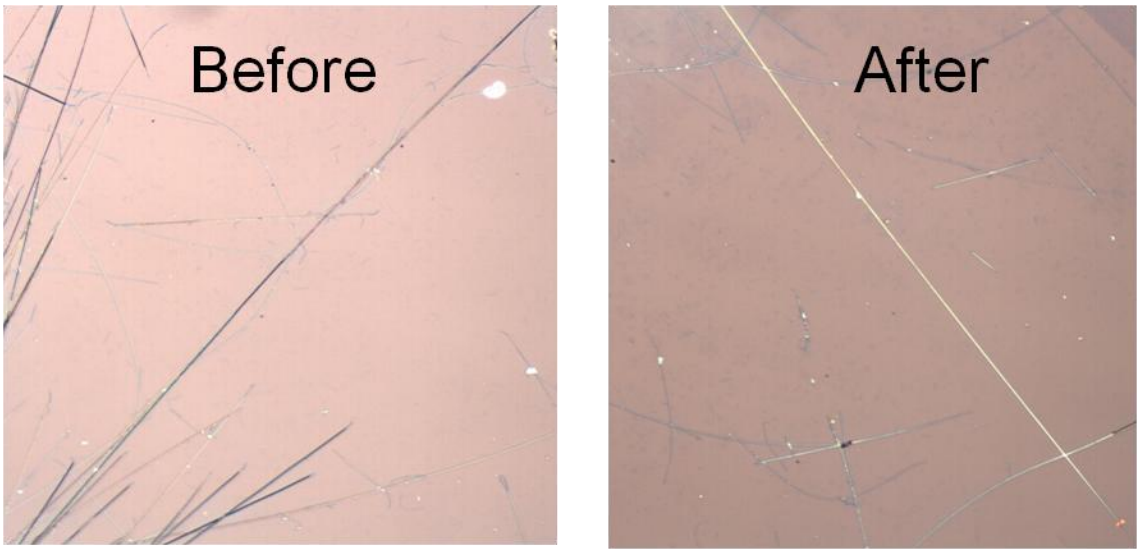

Fig. 5.22 Photograph of needle like DOC crystal before and after acetone washing.

5.6.3 Confirmation of removal of surfactants using SEM-EDX and Auger mapping

Fig. 5.23 shows the results of Scanning Electron Microscope Energy Dispersive X-ray spectroscopy (SEM-EDX). Fig. 5.23 (a) and (b) show the EDX spectra of the aligned SWCNT assemblies before and after washing procedures using acetone, respectively. Before washing, we observed the peak of Na at 1040 eV, which indicates the presence of surfactants. After washing, the signals due to Na could not be detected, less than noise signals. We also performed Auger Electron Spectroscopy measurement. Fig. 5.24 shows SEM image and Scanning Auger Maps of the aligned SWCNT assembly after washing. The bright area indicates the presence of the corresponding elements. As shown in the figure, the signals from Na could not be detected, indicating that the presence of Na was less than 4 atomic percent. These results indicate that the surfactants were well removed by this washing procedure.

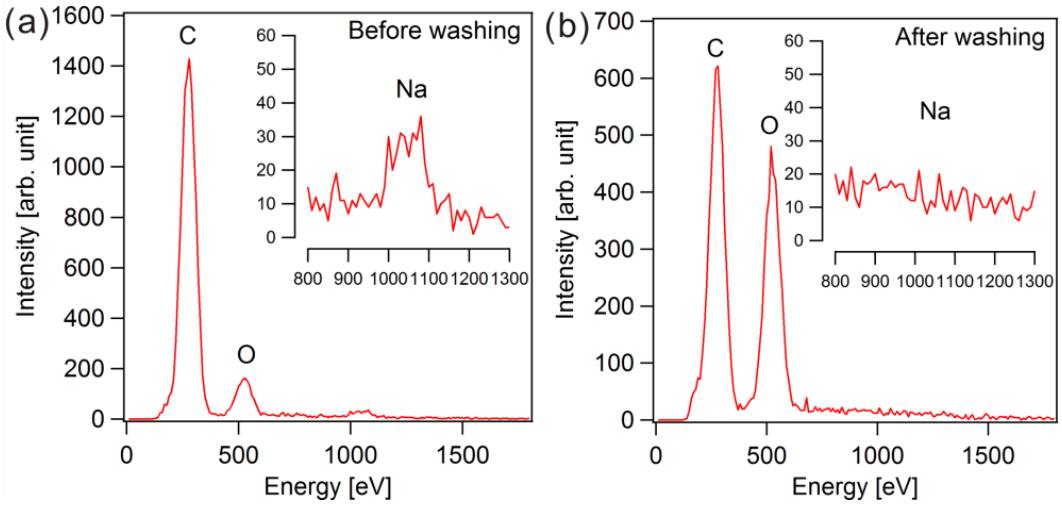

Fig. 5.23 SEM-EDX spectra of aligned SWCNT assemblies (a) before and (b) after washing, respectively. (Copyright 2014 AIP Publishing LLC)

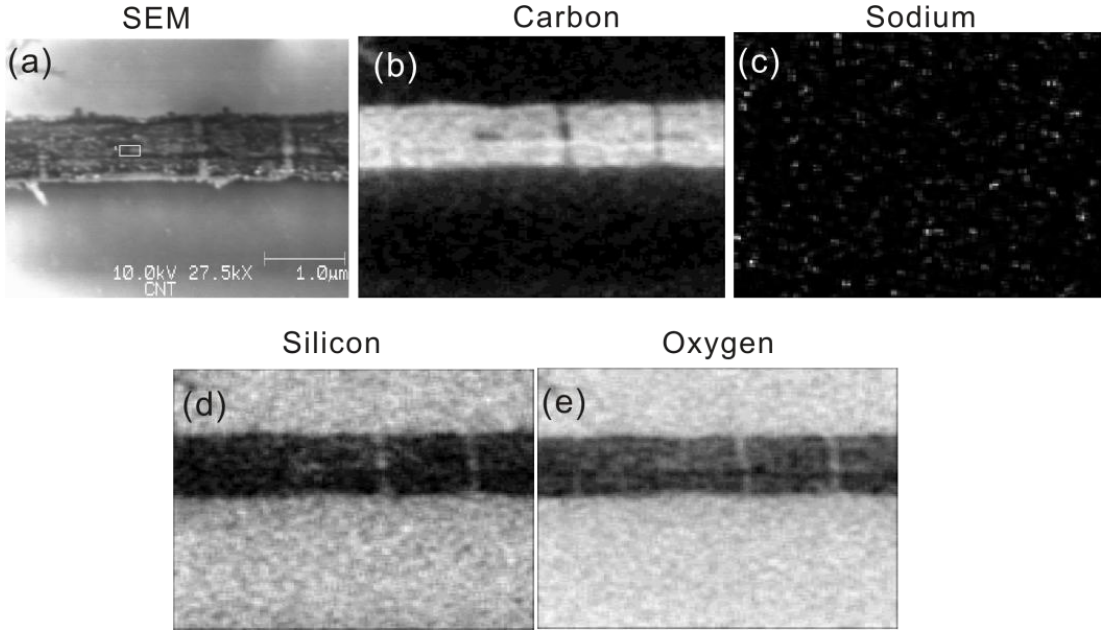

Fig. 5.24 (a) SEM image of after washing sample. Scanning Auger Map images of (b) carbon, (c) Sodium, (d) silicon, and (e) oxygen. The bright area indicates the presence of corresponding elements. (Copyright 2014 AIP Publishing LLC)

5.6.4 Raman spectra of assembly of aligned SWCNTs.

Raman spectra of G band are shown in Fig. 5.25. Those spectra were excited with 561.34 nm laser.

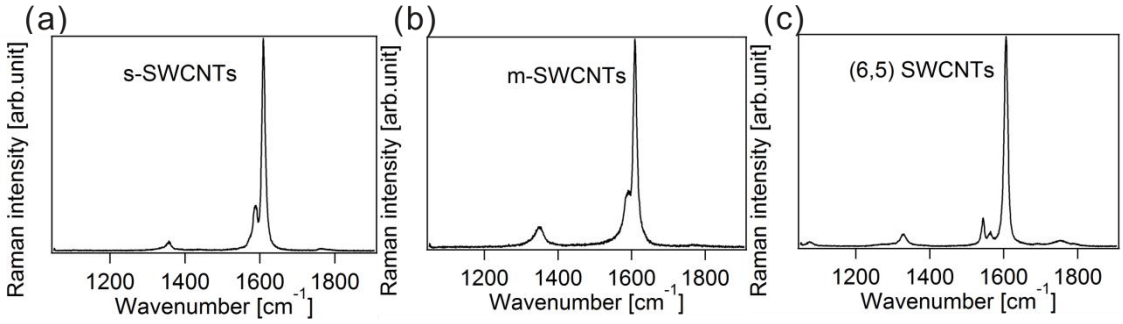

Fig. 5.25 G-band of assemblies of (a) semiconducting (s-SWCNTs), (b) metallic (m-SWCNTs) SWCNTs with diameter of 1.4 nm, and (c) (6,5) SWCNTs. (© 2014 AIP Publishing LLC)

5.6.5 Distribution of the value of I_{max}/I_{min}

To investigate sample dependence of I_{max}/ I_{min} value, we performed polarized micro Raman measurement for 30 samples, which were made from (6,5) SWCNTs. Fig. 5.26 shows a histogram of the I_{max}/ I_{min} value. The mean value is I_{max}/I_{min} = 10 and 70 % of the samples exceed 10.

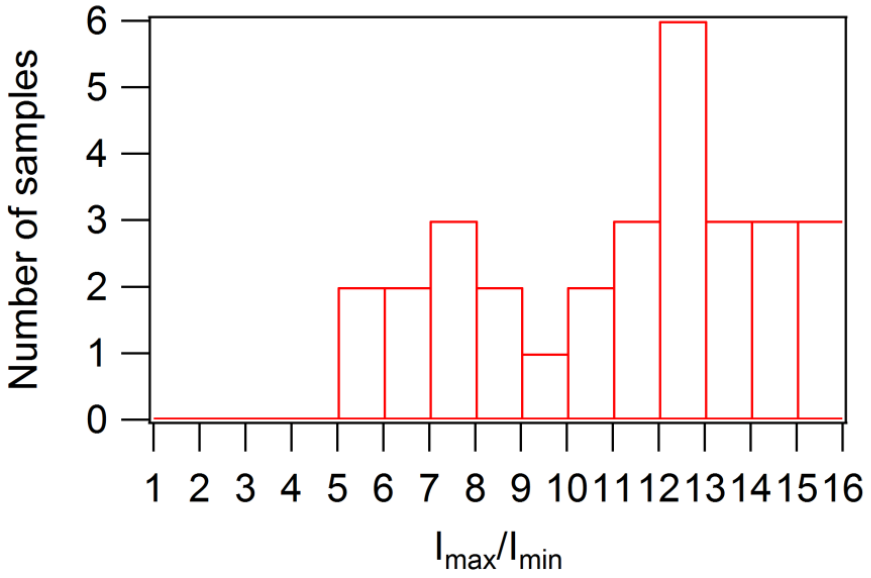

Fig. 5.26 Histogram of the I_{max}/I_{min} value evaluated from 30 samples. (Copyright 2014 AIP Publishing LLC)

5.7 Capacitance measurement

5.7.1 Principle of capacitance measurement

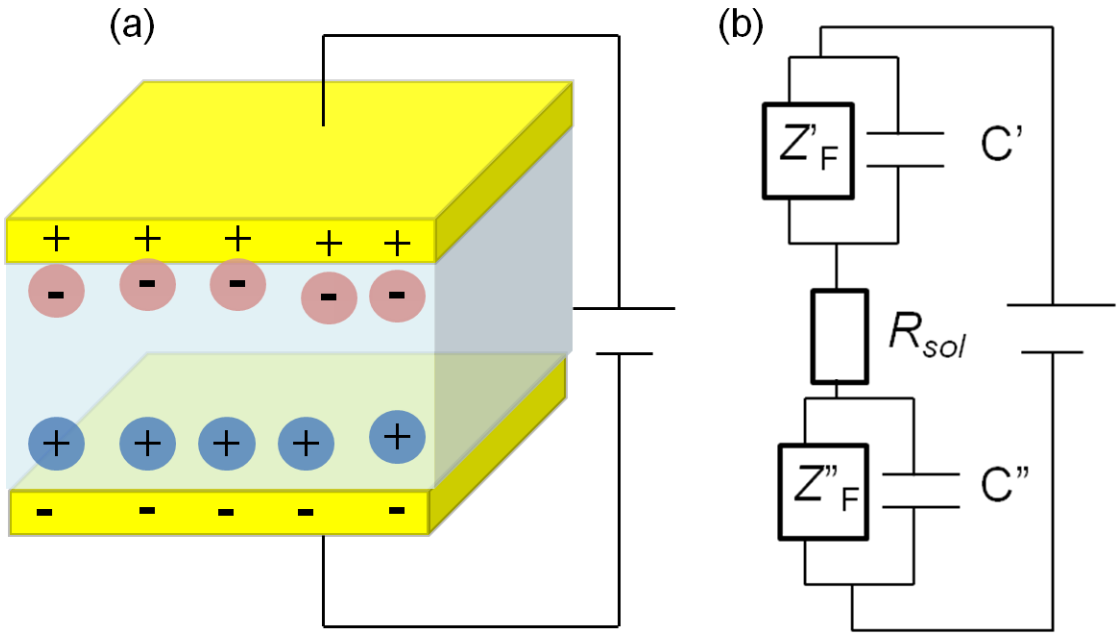

Fig. 5.27 (a) A schematic illustration of electric double layer capacitor. Red and blue ball represents anion and cation, respectively. (b) shows an equivalent circuit model.

Fig. 5.15 (a) and (b) show a schematic illustration of electric double layer capacitor and equivalent circuit model of the capacitor, respectively. Z_F and Z'_F denote the Faradiac impedance at the surface of electrode / electrolyte interface and C and C' denote double layer capacitance. R_{sol} denotes the resistance of solution resistance. To measure the capacitance of electric double layer capacitance we perform A.C. impedance measurement as follows. Fig. 5.28 shows simple model where a resistance and a capacitor are connected in parallel. The total impedance is given by

$$\frac{1}{Z} = \frac{1}{R} + \frac{1}{\frac{1}{j\omega C}} \tag{5.42}$$

$$Z = \frac{R}{1+(\omega RC)^2} - j\frac{\omega R^2 C}{1+(\omega RC)^2} = Z' + jZ'' \tag{5.43}$$

By transforming equation (5.43) we can get

$$C = \frac{-Z''}{\omega(Z'^2 + Z''^2)} \tag{5.44}$$

Therefore, we can obtain the capacitance by measuring the real and imaginary part of impedance. Here, the impedance of the circuit is given by

$$Z = \frac{V}{I} \tag{5.45}$$

As shown in Fig. 5.28 (b) the phase of the current shifts against the voltage. Measuring the phase shift θ and $|Z|$ we can get Z' and Z'':

$$Z' = |Z|\cos\theta$$
$$Z'' = |Z|\sin\theta \qquad (5.46)$$

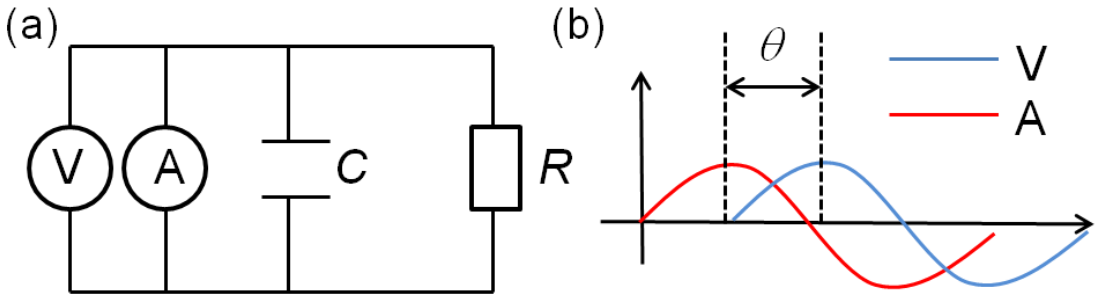

Fig. 5.28 (a) Simple model of electric double layer capacitor. (b) A Phase shift between the current and voltage of the circuit.

5.7.2 Experimental setup

Capacitance of electric double layer, which is formed on surface of a channel was measured using a potentiostat (ALS Model 611 ES, BAS Co.). Device set up was the same as the electrolyte gating set up in Fig. 2.4. We analyzed the capacitance using a model in which capacitor of electric double layer and resistor are connected in parallel. For example, Fig. 5.29 (a) shows phase shift as a function of reference voltage V_R at 1Hz, and the phase shift was close to -90 in all V_R range, which indicate electric double layer well behave as capacitor in the model as described above. Fig. 5.29 (b) shows the specific capacitance of semiconducting SWCNTs as a function of the reference voltage.

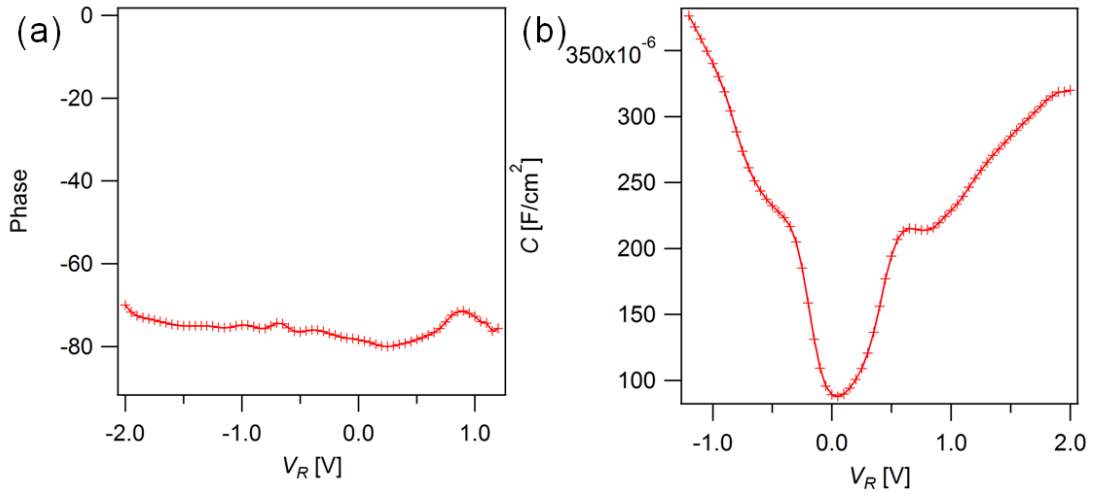

Fig. 5.29 (a) Phase shift as a function of reference voltage. (b) Capacitance of semiconducting SWCNTs as a function of reference voltage.

5.7.3 Capacitance measurement SWCNTs networks

We performed capacitance measurements to evaluate carrier concentrations of SWCNT networks under carrier injection by electrolyte gating technique. Fig. 5.30 (a) ,(c) and (e) show capacitance and carrier concentrations of semiconducting, metallic and (6,5) enriched SWCNT networks, respectively. The total capacitance of the film C_{tot} can be written as $C_{tot} = C_{st} + C_q$. Here, C_{st} is the structural capacitance, and C_q is quantum capacitance of the SWCNTs. C_q represents the density of states, $g(E_F)$, of the SWCNTs,

$$C_q = e^2 g(E_F) \tag{5.47}$$

Therefore, when the Fermi level was located between the band gap of the first van-Hove singularities, the total capacitance was dominated by the quantum capacitance term, reflecting the smallness of the DOS of the SWCNTs. As show in Fig. 5.30 (a),(c) and (e) there was clear dip structure in the capacitance in all the types of SWCNTs, which reflect their band gap. We calculated carrier concentration of the SWCNTs networks using following equation,

$$n = \int_0^V C(V)dV \tag{5.48}$$

In the case of semiconducting SWCNT networks, the carrier concentration was around 1.2 $\times$ 10^{20} cm^{-3} and 0.9 $\times$ 10^{20} cm^{-3} for N-doped and P-doped state, respectively. In metallic SWCNT networks, that was 0.9 $\times$ 10^{20} cm^{-3} (N-doped) and 0.7 $\times$ 10^{20} cm^{-3} (P-doped). In the case of (6,5) enriched SWCNTs, that was 0.6 $\times$ 10^{20} cm^{-3} (N-doped) and 0.7 $\times$ 10^{20} cm^{-3} (P-doped). The values are consistent with previous reports on carrier doping using electrolyte gating technique.[157] We also calculated a field effect mobility of electron and hole in the SWCNT networks using following equation:

$$I_D = C(V_R - V_T - \frac{1}{2}V_D) \times \frac{V_D}{L} \times W \times \mu \tag{5.49}$$

Where V_T and V_D are threshold voltage and vias voltage in the transfer characteristics, respectively. L and W are length and width of the channel, respectively. μ is field effect mobility of carrier. By differentiate I_D with V_R we can get

$$\mu = \frac{L}{CWV_D}\frac{dI_D}{dV_R} \tag{5.50}$$

In Fig. 5.30 (b) and (d) field effect mobility is plotted as a function of the reference voltage In the case of semiconducting SWCNT networks the maximum field effect mobility was 4.5 $cm^2/V \cdot S$ for electron and 6.2 $cm^2/V \cdot S$ for hole, which is consistent with

a conventional FET of SWCNT networks.[85] In the metallic SWCNT networks the maximum field effect mobility was 2.7 $cm^2/V \cdot S$ for electron and 1.9 $cm^2/V \cdot S$ for hole. In the case of (6,5) enriched SWCNTs, that was 30 $cm^2/V \cdot S$ for electron and 34 $cm^2/V \cdot S$ for hole. The values are consistent with previously reported data on field effect transistor of (6,5) enriched SWCNTs[46].

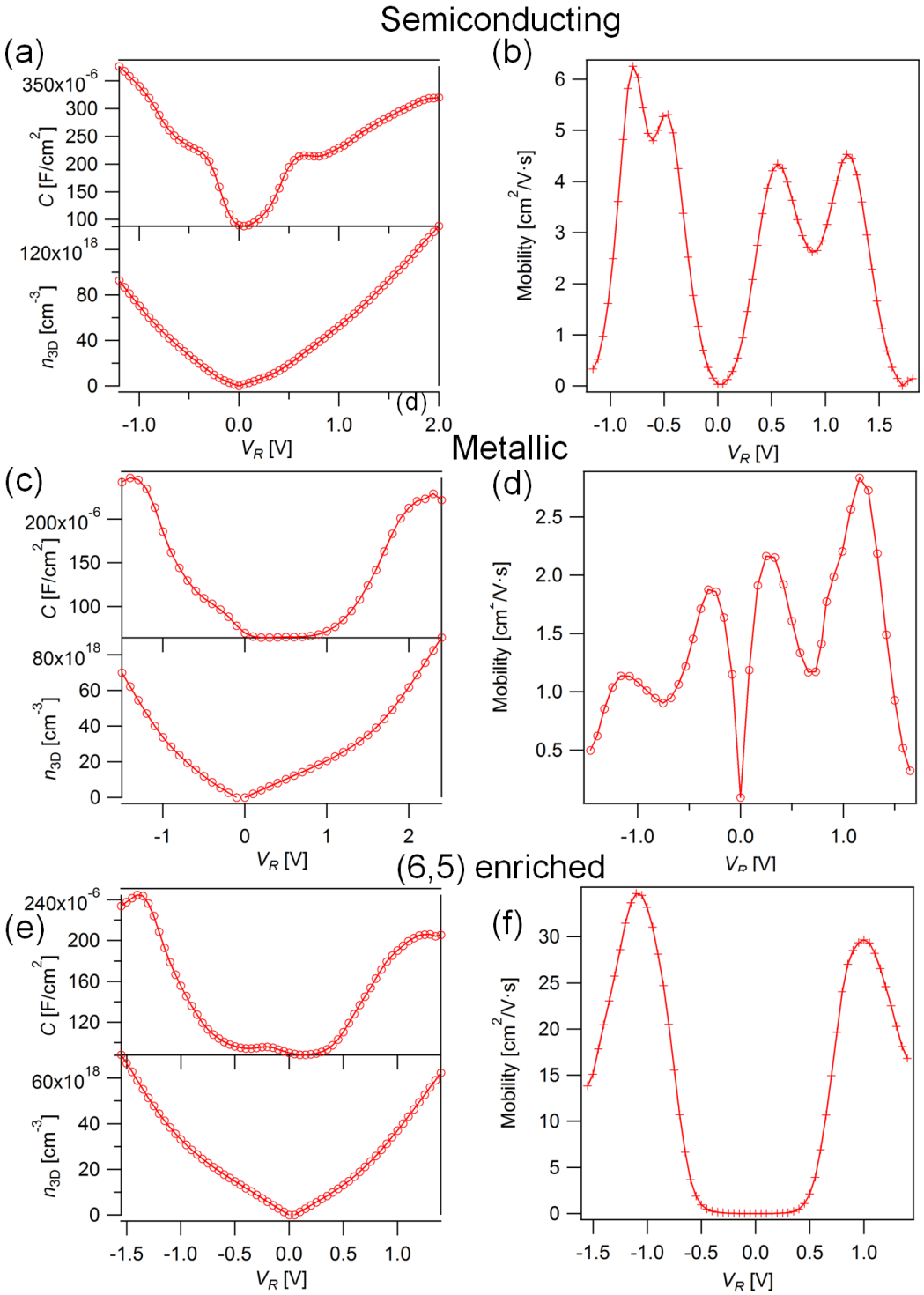

Fig. 5.30 Capacitance and carrier concentration of semiconducting and metallic SWCNT networks are shown in (a) and (c), respectively. Field effect mobility of semiconducting and metallic SWCNT networks are shown in (b) and (d), respectively.

5.7.4 Capacitance measurement of WS_2 NT networks

Capacitance and carrier concentration of WS_2 NT networks are shown in Fig. 5.31 (a). There was a dip structure in the capacitance. The carrier concentration was around 6×10^{18} cm^{-3} for electron and 5×10^{18} for hole. Field effect mobility is also shown in Fig. 5.31 (b). The maximum field effect mobility was 0.37 $cm^2/V\cdot S$ for electron and 3.46 $cm^2/V\cdot S$ for hole region.

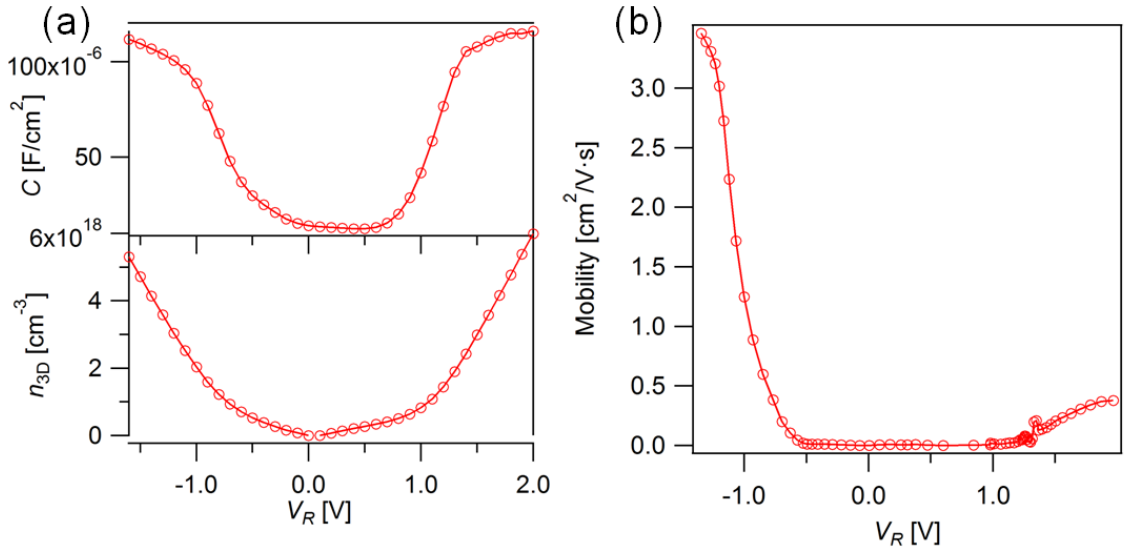

Fig. 5.31 (a) Capacitance and carrier concentration of WS_2 NT networks. (b) Field effect mobility of WS_2 NT networks.

5.8 Analysis of transport mechanisms in SWCNT networks

Fig. 2.10 shows analysis results of semiconducting, metallic and (6,5) enriched SWCNT networks. Fig. 2.10 (a), (c) and (e) show logarithmic derivative methods for semiconducting, metallic and (6,5) enriched SWCNT networks, respectively. In Fig. 2.10 (b), (d) and (f) we plotted ln$R$ against $T^{-1/(1+d)}$ with deduced d. We evaluated the T_0 from the slope as shown in Fig. 2.10 (b), (d) and (f) for semiconducting, metallic and (6,5) SWCNT networks.

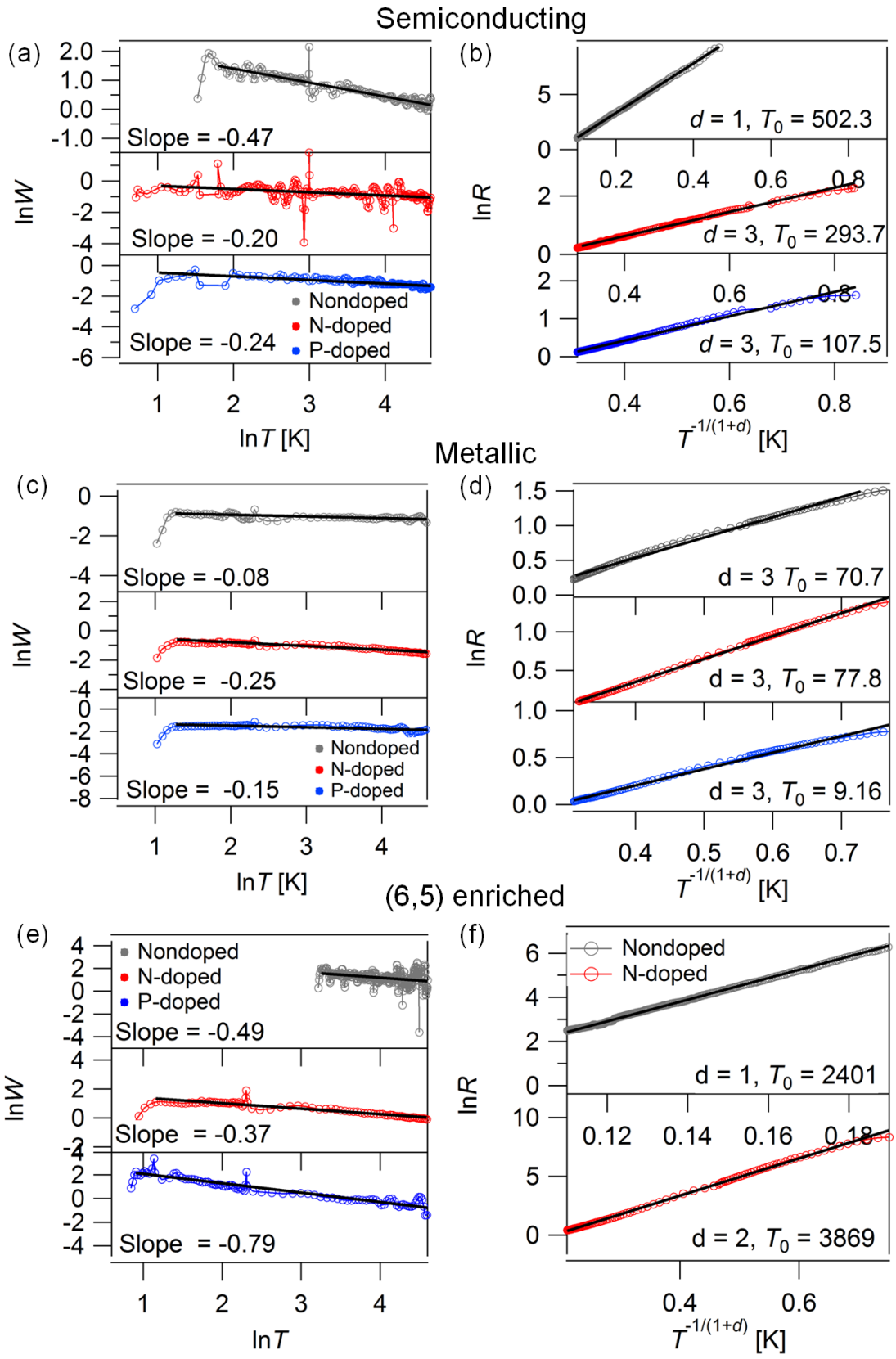

Fig. 5.32 Analysis results of transport mechanisms of SWCNT networks using VRH

model. (a) , (c) and (e) show ln$W$ versus ln$T$ for semiconducting, metallic and (6,5) enriched SWCNT networks, respectively. Grey line shows nondoped state. red line and blue line show N-doped and P-doped state, respectively. (b), (d) and (f) shows ln$R$ versus $T^{-1/(1+d)}$ for semiconducting, metallic, (6,5) SWCNT networks, respectively. Black lines show their loner fitting.

We summarized relationship between type of SWCNTs, d, and T_0 in Table 5.1.

Table 5.1 relationship between type of SWCNTs, d, and T_0

Doped carrier	Semiconducting	Metallic	(6,5)
Non-doped	$d=3, T_0=85.0$	$d=3, T_0=70.7$	$d=1, T_0=2401$
N-doped	$d=3, T_0=199.8$	$d=3, T_0=77.8$	$d=2, T_0=3869$
P-doped	$d=3, T_0=15.6$	$d=3, T_0=9.1$	Could not fitted by VRH model

5.9 Thermoelectric measurement

5.9.1 Attachment of thermo-couples

As shown in Fig. 5.33 an attachment of thermo-couples is performed by following procedure. (a) The parylene substrate is placed on another substrate and the rubber is also placed on the substrate. (b) Epoxy adhesive is attached on the film where a thermo-couple will be attached in order to protect the film from damage by thermo-couple. (c) After the epoxy adhesive become hard the thermo-couple is attached on the epoxy adhesive. (d) A silver paste is painted on the contact point of thermo-couple and the epoxy adhesive. (e) After the silver paste becomes hard the silver paste is coated by epoxy adhesive. (f) We wait until the epoxy become hard.

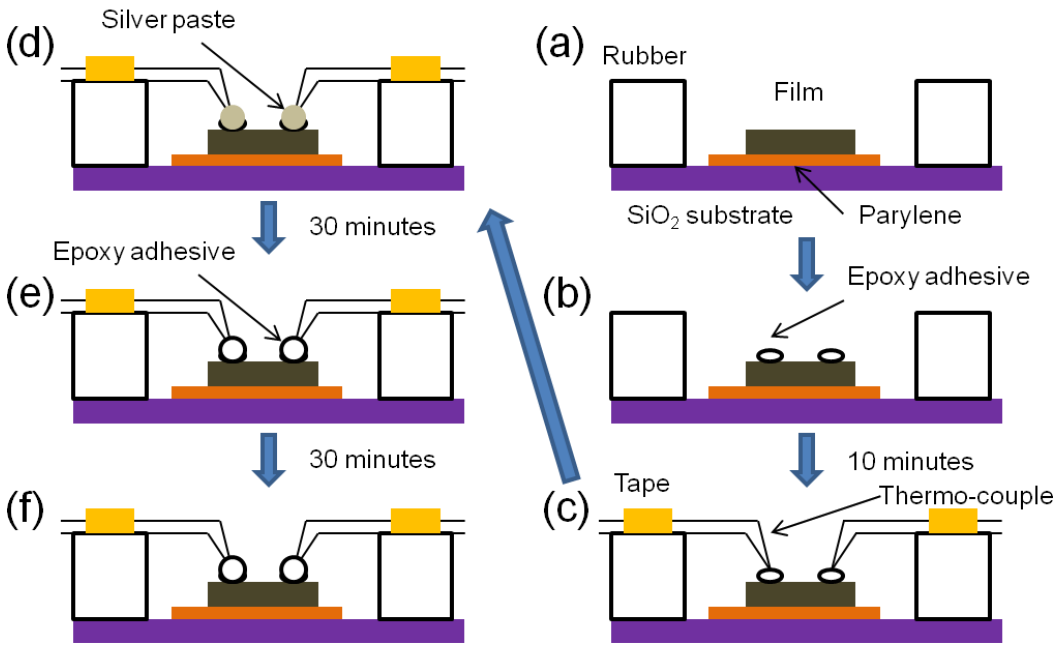

Fig. 5.33 A procedure of attachment of epoxy adhesive.

5.9.2 Confirmation of linearity of ΔV against ΔT

Fig. 5.34 shows thermoelectric voltage ΔV as a function of temprature gradient ΔT. ΔT was controlled by changing power of laser irradiation, and ΔV linearly behaved against ΔT in all V_G region where we could measure the Seebeck coefficient by electrolyate gating technique.

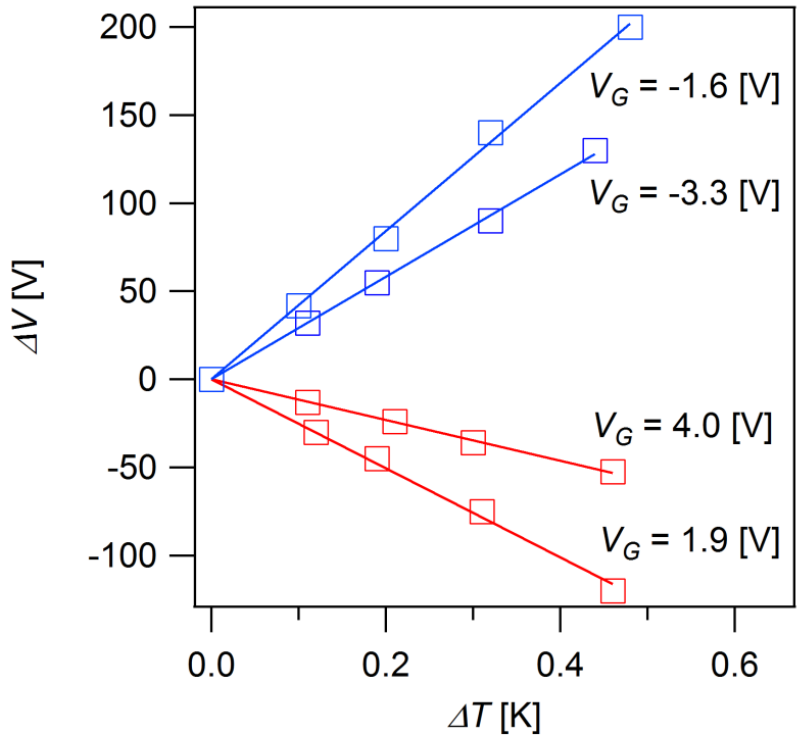

Fig. 5.34 Relationships between thermoelectric voltage ΔV and temperature gradient ΔT with reference voltage (V_R) applications. The square symbols represent the measured data, and the solid lines exhibit linear fitting results.(Copyright 2017 The Japan Society of Applied Physics)

6 List of publications and presentations

6.1 Scientific publications

6.1 H. Kawai, K. Hasegawa, R. Nakatsu, Y. Naitou, Y. Takagi, Y. Wada, T. Takenobu, K. Yanagi, String-like Assembly of Aligned Single-Wall Carbon Nanotubes in a Single-Chiral State,
Applied Physics Express 6, 065103(2013).

6.2 H. Kawai, K. Hasegawa, A. Oyane, Y. Naitou, K. Yanagi, Self-formation of highly aligned metallic semiconducting and single chiral single-walled carbon nanotubes via a crystal template method,
Applied Physics Letters 105, 093102(2014).

6.3 H. Kawai, M. Sugahara, R. Okada, Y. Maniwa, Y. Yomogida, K. Yanagi, Thermoelectric Properties of WS_2 nanotube networks,
Applied Physics Express, 10, 015001(2017).
Selected as spot light

6.4 K. Yanagi, S. Kanda, Y. Oshima, Y. Kitamura, H. Kawai, T. Yamamoto, T. Takenobu, Y. Nakai, Y. Maniwa, Tuning of the Thermoelectric Properties of One-Dimensional Material Networks by Electric Double layer Techniques using ionic liquids,
Nano Letters. 14, 6437-6442(2014).

6.5 T. Igarashi, H. Kawai, C. Nguyen, S. Okada, T. Pichler, K. Yanagi, Tuning Localized Transverse Surface Plasmon Resonance in Electricity-Selected Single-Wall Carbon Nanotube by Electrochemical Doping,
Physical Review Letters 114, 176807(2015).

6.6 M. Sugahara, H. Kawai, Y. Yomogida, Y. Maniwa, S. Okada and K. Yanagi, Ambipolar transistors based on random networks of WS_2 nanotubes,
Applied Physics Express 9, 075001(2016).

6.2 Presentations in international conferences

6.7 H. Kawai, K. Hasegawa, T. Nakatsu, T. Takenobu, K. Yanagi, String-like

Assembly of Aligned Single-Wall Carbon Nanotubes in a Single-Chiral State, NT13, Helsink, June 2013.

6.8 H. Kawai, K. Hasegawa, K. Yanagi, Electrical property of highly aligned metallic single-walled carbon nanotubes assembly,
IWEPNM2015, Kirchberg, March 2015.

6.9 H. Kawai, K. Hasegawa, K. Yanagi, Transport property of highly aligned and chirality selected SWCNTs,
NT15, Nagoya, June 2015.

6.10 H. Kawai, K. Hasegawa, K. Yanagi, Hall measurements in metallic single walled carbon nanotubes networks with ionic liquid gating,
IWEPNM2016, Kirchberg, March 2016.

6.3 Presentations in domestic meetings [in Japanese]

6.11 H. Kawai, K. Hasegawa, T. Takenobu, K. Yanagi, Chirality purification of single wall carbon nanotube by control of alcohol concentration,
FNTG, Miyagi pref., Sep., 2012.

6.12 H. Kawai, K. Hasegawa, T. Takenobu, K. Yanagi, String-like Aggregates of Aligned (6,5) Single Wall Carbon Nanotubes,
FNTG, Tokyo, March, 2013.

6.13 H. Kawai, K. Hasegawa, T. Takenobu, String-like Assembly of Aligned Single-Wall Carbon Nanotubes in a Single-Chiral State,
FNTG, Osaka, August, 2013.

6.14 H. Kawai, K. Hasegawa, T. Takenobu, K. Yanagi, Fabrication of highly aligned metallic/semiconducting SWCNTs assembly and its electrical properties,
JSAP Meeting, Kyoto, Sep., 2013.

6.15 H. Kawai, K. Hasegawa, T. Takenobu, K. Yanagi, Fabrication of highly aligned metallic/semiconducting SWCNTs assembly and its electrical properties,
JPS Meeting, Hiroshima pref., Sep., 2013.

6.16 H. Kawai, K. Hasegawa, T. Takenobu, K. Yanagi, Self-assembly of Highly Aligned Metallic/Semiconducting SWCNTs using Crystal Templates,
FNTG, Tokyo, March, 2014.

6.17 K. Yanagi, H. Kawai, S. Kanda, Y. Oshima, Y. Kitamura, T. Yamamoto, Y. Nakai, Y. Maniwa, Tuning of the Thermoelectric Properties of semiconducting SWCNT networks by Electric Double layer Techniques using ionic liquids,
JPS Meeting, Nagoya, Sep., 2014.

6.18 H. Kawai, K. Hasegawa, K. Yanagi, Self-formation of highly aligned metallic semiconducting and single chiral single-walled carbon nanotubes via a crystal template method,
JSAP Meeting, Hokkaido pref., Sep., 2014.

6.19 H. Kawai, K. Hasegawa, T. Takenobu, K. Yanagi, Thermoelectric properties of chirality selected SWCNTs,
JPS Meeting, Miyagi pref., March, 2016.

7 Acknowledgments

First of all, I would like to thank my supervisor, Assoc. Prof. Dr. Kazuhiro Yanagi for his 5-year guidance of my doctoral work. He gave me the greatest working place to study a lot of things. He showed me how to advance scientific research, i.e. what topic is important in science, how to manage laboratory, how to write a paper. Scientific discussion with him was most important thing for me. He gave me a chance to go Vienne univ. and he supported my research during the stay in Vienna. I believe that all that he gave me in these 6 years will be firm foundation for my future life.

I would like to thank to Assist. Prof. Dr Yohei Yomogida. He supported me with scientific suggestion and discussion. His scientific suggestions are always very good points, so that I have really enjoyed a scientific talk with him. I would like to emphasize that his suggestion greatly supported my scientific paper. The quality of the paper would have never been accomplished without his support.

I appreciate the generous support of Prof. Dr. Thomas Pichler, and Prof. Dr. Paola in Vienna Univ. during my stay in Vienna. In their labs, I studied a lot of things, e.g. scientific discussion using English, fascinating laboratory equipment, conference in Kirchberg. They also supported my stay in Vienna and it was greatly helpful for me. I believe that stay in their labs became my life asset.

I would like to thank Dr Hidekazu Shiozawa in Vienna Univ. He totally supported my stay in Vienna. He gave me a lot of suggestion in my research in Vienna. I emphasize that my work in Vienne have never accomplished without his support. I also thanks to member of labs in Vienna Univ. They supported my stay and research. Especially, I would like to thank to Dr. Lei Shi, Mr. Carlos Reinoso, Mr. Filippo Fedi, Mr. Oleg Domanov, Mr. Philip Rohringer, Mr. Markus Sauer.

For the contribution of the SWCNTs research, I appreciate the contributions of Prof. Dr. Taishi Takenobu at Nagoya Univ. and member of his labs, Mr. Yuki Takagi, Mr. Yoshifumi Wada. They provided me with several experimental results and fruitful discussion related to electrical properties of SWCNTs. I would like to thank to Dr. Yasuhisa Naitoh at National Institute of Advanced Industrial Science and Technology, Tsukuba. He gave me several experimental results and good suggestion related to Scanning Electron Microscope. For contribution of thermoelectric research, I appreciate the contribution of Prof. Dr. Yutaka Maniwa, and Assist. Prof. Yusuke Nakai. They provided me with several experimental results and discussion.

Many thanks should be given to Mr. Hikaru Kudo, Mr. Kai Hasegawa, Mr. Junji Nozaki, Mr. Yoshimasa Kitamura, Mr. Kotaro Honma Mr. Yuki Oshima, Mr. Yoshida

Minehito, Mr. Musashi Fukumura, Mitsunari Sugawara, Ryotaro Okada. We have shared a grateful time. Especially I thank to Kai Hasegawa, Mitsunari Sugahara, and Ryotaro Okada. They supported my works.

Finally I would to very thank to my family. They financially supported and encouraged during my doctoral course.

8 Reference

[1] S. Frank, P. Poncharal, Z. L. Wang, and W. A. de Heer, "Carbon nanotube quantum resistors," Science **280** (5370), 1744 (1998).

[2] J. Park, A. N. Pasupathy, J. I. Goldsmith, C. Chang, Y. Yaish, J. R. Petta, M. Rinkoski, J. P. Sethna, H. D. Abruna, P. L. McEuen, and D. C. Ralph, "Coulomb blockade and the Kondo effect in single-atom transistors," Nature **417** (6890), 722 (2002).

[3] M. Nirmal, B. O. Dabbousi, M. G. Bawendi, J. J. Macklin, J. K. Trautman, T. D. Harris, and L. E. Brus, "Fluorescence intermittency in single cadmium selenide nanocrystals," Nature **383** (6603), 802 (1996).

[4] L. L. Chang, L. Esaki, and R. Tsu, "Resonant Tunneling in Semiconductor Double Barriers," Applied Physics Letters **24** (12), 593 (1974).

[5] K. Vonklitzing, G. Dorda, and M. Pepper, "New Method for High-Accuracy Determination of the Fine-Structure Constant Based on Quantized Hall Resistance," Physical Review Letters **45** (6), 494 (1980).

[6] M. A. Reed, J. N. Randall, R. J. Aggarwal, R. J. Matyi, T. M. Moore, and A. E. Wetsel, "Observation of Discrete Electronic States in a Zero-Dimensional Semiconductor Nanostructure," Physical Review Letters **60** (6), 535 (1988).

[7] H. Shirakawa, "The discovery of polyacetylene film: The dawning of an era of conducting polymers (Nobel lecture)," Angewandte Chemie-International Edition **40** (14), 2575 (2001).

[8] A. G. MacDiarmid, ""Synthetic metals": A novel role for organic polymers (Nobel lecture)," Angewandte Chemie-International Edition **40** (14), 2581 (2001).

[9] A. J. Heeger, "Semiconducting and metallic polymers: The fourth generation of polymeric materials (Nobel lecture)," Angewandte Chemie-International Edition **40** (14), 2591 (2001).

[10] S. Iijima, "Helical Microtubules of Graphitic Carbon," Nature **354** (6348), 56 (1991).

[11] S. Iijima and T. Ichihashi, "Single-Shell Carbon Nanotubes of 1-Nm Diameter," Nature **363** (6430), 603 (1993).

[12] R. Tenne, L. Margulis, M. Genut, and G. Hodes, "Polyhedral and Cylindrical Structures of Tungsten Disulfide," Nature **360** (6403), 444 (1992).

[13] M. M. J. Treacy, T. W. Ebbesen, and J. M. Gibson, "Exceptionally high Young's modulus observed for individual carbon nanotubes," Nature **381** (6584), 678 (1996).

[14] I. Kaplan-Ashiri, S. R. Cohen, K. Gartsman, V. Ivanovskaya, T. Heine, G. Seifert, I. Wiesel, H. D. Wagner, and R. Tenne, "On the mechanical behavior of WS2

nanotubes under axial tension and compression," Proceedings of the National Academy of Sciences of the United States of America **103** (3), 523 (2006).

[15] L. Guimaraes, A. N. Enyashin, J. Frenzel, T. Heine, H. A. Duarte, and G. Seifert, "Imogolite nanotubes: Stability, electronic, and mechanical properties," Acs Nano **1** (4), 362 (2007).

[16] R. Saito, *Physical Properties of Carbon Nanotubes*. (Imperial College Press, 1998).

[17] I. Milosevic, B. Nikolic, E. Dobardzic, M. Damnjanovic, I. Popov, and G. Seifert, "Electronic properties and optical spectra of MoS(2) and WS(2) nanotubes," Phys. Rev. B **76** (23), 233414 (2007).

[18] M. Bockrath, D. H. Cobden, J. Lu, A. G. Rinzler, R. E. Smalley, L. Balents, and P. L. McEuen, "Luttinger-liquid behaviour in carbon nanotubes," Nature **397** (6720), 598 (1999).

[19] J. Kong, E. Yenilmez, T. W. Tombler, W. Kim, H. J. Dai, R. B. Laughlin, L. Liu, C. S. Jayanthi, and S. Y. Wu, "Quantum interference and ballistic transmission in nanotube electron waveguides," Physical Review Letters **87** (10), 106801 (2001).

[20] A. Javey, J. Guo, Q. Wang, M. Lundstrom, and H. J. Dai, "Ballistic carbon nanotube field-effect transistors," Nature **424** (6949), 654 (2003).

[21] D. Mann, A. Javey, J. Kong, Q. Wang, and H. J. Dai, "Ballistic transport in metallic nanotubes with reliable Pd ohmic contacts," Nano Letters **3** (11), 1541 (2003).

[22] L. Hu, D. S. Hecht, and G. Gruner, "Percolation in transparent and conducting carbon nanotube networks," Nano Letters **4** (12), 2513 (2004).

[23] E. Bekyarova, M. E. Itkis, N. Cabrera, B. Zhao, A. P. Yu, J. B. Gao, and R. C. Haddon, "Electronic properties of single-walled carbon nanotube networks," Journal of the American Chemical Society **127** (16), 5990 (2005).

[24] V. Skakalova, A. B. Kaiser, Y. S. Woo, and S. Roth, "Electronic transport in carbon nanotubes: From individual nanotubes to thin and thick networks," Physical Review B **74** (8), 085403 (2006).

[25] P. E. Lyons, S. De, F. Blighe, V. Nicolosi, L. F. C. Pereira, M. S. Ferreira, and J. N. Coleman, "The relationship between network morphology and conductivity in nanotube films," Journal of Applied Physics **104** (4), 044302 (2008).

[26] P. N. Nirmalraj, P. E. Lyons, S. De, J. N. Coleman, and J. J. Boland, "Electrical Connectivity in Single-Walled Carbon Nanotube Networks," Nano Letters **9** (11), 3890 (2009).

[27] J. Vavro, J. M. Kikkawa, and J. E. Fischer, "Metal-insulator transition in doped single-wall carbon nanotubes," Physical Review B **71** (15), 155410 (2005).

[28] M. Kociak, A. Y. Kasumov, S. Gueron, B. Reulet, Khodos, II, Y. B. Gorbatov, V. T.

Volkov, L. Vaccarini, and H. Bouchiat, "Superconductivity in ropes of single-walled carbon nanotubes," Physical Review Letters **86** (11), 2416 (2001).

[29] Z. K. Tang, L. Y. Zhang, N. Wang, X. X. Zhang, G. H. Wen, G. D. Li, J. N. Wang, C. T. Chan, and P. Sheng, "Superconductivity in 4 angstrom single-walled carbon nanotubes," Science **292** (5526), 2462 (2001).

[30] R. Lortza, Q. C. Zhang, W. Shi, J. T. Ye, C. Y. Qiu, Z. Wang, H. T. He, P. Sheng, T. Z. Qian, Z. K. Tang, N. Wang, X. X. Zhang, J. N. Wang, and C. T. Chan, "Superconducting characteristics of 4-angstrom carbon nanotube-zeolite composite," Proceedings of the National Academy of Sciences of the United States of America **106** (18), 7299 (2009).

[31] X. J. Tan, H. J. Liu, Y. W. Wen, H. Y. Lv, L. Pan, J. Shi, and X. F. Tang, "Optimizing the thermoelectric performance of zigzag and chiral carbon nanotubes," Nanoscale Research Letters **7**, 116 (2012).

[32] N. T. Hung, A. R. T. Nugraha, E. H. Hasdeo, M. S. Dresselhaus, and R. Saito, "Diameter dependence of thermoelectric power of semiconducting carbon nanotubes," Physical Review B **92** (16), 165426 (2015).

[33] D. Hayashi, Y. Nakai, H. Kyakuno, T. Yamamoto, Y. Miyata, K. Yanagi, and Y. Maniwa, "Improvement of thermoelectric performance of single-wall carbon nanotubes by heavy doping: Effect of one-dimensional band multiplicity," Applied Physics Express **9** (12), 125103 (2016).

[34] M. J. Buehler, "Mesoscale modeling of mechanics of carbon nanotubes: Self-assembly, self-folding, and fracture," Journal of Materials Research **21** (11), 2855 (2006).

[35] S. Cranford, H. M. Yao, C. Ortiz, and M. J. Buehler, "A single degree of freedom 'lollipop' model for carbon nanotube bundle formation," Journal of the Mechanics and Physics of Solids **58** (3), 409 (2010).

[36] S. Kang, Kocabas, C., Ozel, T., Shim, M., Pimparkar, N., Alam, M., Rotkin, S. & Rogers, J. , "High-performance electronics usind dense, perfectly aligned arrays of single-walled carbon nanotubes," Nat. Nanotech. **2**, 230 (2007).

[37] S. Hong, Banks, T. and Rogers, J. , "Improved Density in Aligned Arrays of Single-Walled Carbon Nanotubes by Sequential Chemical Vapor Deposition on Quartz," Adv. Mater. **22** (16), 1826 (2010).

[38] Y. Maniwa, H. Kataura, and A. Fujiwara, "Structural Studies of Carbon Nanotubes by Powder

X-ray Diffraction at SPring-8 and KEK PF," Journal of the Japanese Society for Synchrotron Radiation Research **16** (5) (2003).

[39] S. M. Bachilo, L. Balzano, J. E. Herrera, F. Pompeo, D. E. Resasco, and R. B. Weisman, "Narrow (n,m)-distribution of single-walled carbon nanotubes grown using a solid supported catalyst," Journal of the American Chemical Society **125** (37), 11186 (2003).

[40] F. Yang, X. Wang, D. Q. Zhang, J. Yang, D. Luo, Z. W. Xu, J. K. Wei, J. Q. Wang, Z. Xu, F. Peng, X. M. Li, R. M. Li, Y. L. Li, M. H. Li, X. D. Bai, F. Ding, and Y. Li, "Chirality-specific growth of single-walled carbon nanotubes on solid alloy catalysts," Nature **510** (7506), 522 (2014).

[41] M. S. Arnold, A. A. Green, J. F. Hulvat, S. I. Stupp, and M. C. Hersam, "Sorting carbon nanotubes by electronic structure using density differentiation," Nature Nanotechnology **1** (1), 60 (2006).

[42] K. Yanagi, Y. Miyata, and H. Kataura, "Optical and conductive characteristics of metallic single-wall carbon nanotubes with three basic colors; Cyan, magenta, and yellow," Applied Physics Express **1** (3), 034003 (2008).

[43] H. P. Liu, D. Nishide, T. Tanaka, and H. Kataura, "Large-scale single-chirality separation of single-wall carbon nanotubes by simple gel chromatography," Nature Communications **2** (2011).

[44] H. P. Liu, T. Tanaka, and H. Kataura, "One-step separation of high-purity (6,5) carbon nanotubes by multicolumn gel chromatography," Physica Status Solidi B-Basic Solid State Physics **248** (11), 2524 (2011).

[45] M. Engel, J. P. Small, M. Steiner, M. Freitag, A. A. Green, M. C. Hersam, and P. Avouris, "Thin Film Nanotube Transistors Based on Self-Assembled, Aligned, Semiconducting Carbon Nanotube Arrays," Acs Nano **2** (12), 2445 (2008).

[46] Alexander A. Green and Mark C. Hersam, "Nearly Single-Chirality Single-Walled Carbon Nanotubes Produced via Orthogonal Iterative Density Gradient Ultracentrifugation," Advanced Materials **23** (19), 2185 (2011).

[47] Y. Miyata, K. Shiozawa, Y. Asada, Y. Ohno, R. Kitaura, T. Mizutani, and H. Shinohara, "Length-Sorted Semiconducting Carbon Nanotubes for High-Mobility Thin Film Transistors," Nano Research **4** (10), 963 (2011).

[48] K. Yanagi, H. Udoguchi, S. Sagitani, Y. Oshima, T. Takenobu, H. Kataura, T. Ishida, K. Matsuda, and Y. Maniwa, "Transport Mechanisms in Metallic and Semiconducting Single-Wall Carbon Nanotube Networks," Acs Nano **4** (7), 4027 (2010).

[49] H. Ago, Uehara, N., Ikeda, K., Ohdo, R., Nakamura, K., Tsuji, M. , "Synthesis of horizontally-aligned single-walled carbon nanotubes with controllable density on sapphire surface and polarized Raman spectroscopy," Chem. Phys. Lett. **421** (4-6),

399 (2006).

[50] E. A. Ekimov, V. A. Sidorov, E. D. Bauer, N. N. Mel'nik, N. J. Curro, J. D. Thompson, and S. M. Stishov, "Superconductivity in diamond," Nature **428** (6982), 542 (2004).

[51] T. E. Weller, M. Ellerby, S. S. Saxena, R. P. Smith, and N. T. Skipper, "Superconductivity in the intercalated graphite compounds C(6)Yb and C(6)Ca," Nature Physics **1** (1), 39 (2005).

[52] A. Y. Ganin, Y. Takabayashi, Y. Z. Khimyak, S. Margadonna, A. Tamai, M. J. Rosseinsky, and K. Prassides, "Bulk superconductivity at 38K in a molecular system," Nature Materials **7** (5), 367 (2008).

[53] A. Kasumov, M. Kociak, M. Ferrier, R. Deblock, S. Gueron, B. Reulet, I. Khodos, O. Stephan, and H. Bouchiat, "Quantum transport through carbon nanotubes: Proximity-induced and intrinsic superconductivity," Physical Review B **68** (21), 214521 (2003).

[54] L. X. Benedict, V. H. Crespi, S. G. Louie, and M. L. Cohen, "Static Conductivity and Superconductivity of Carbon Nanotubes - Relations between Tubes and Sheets," Physical Review B **52** (20), 14935 (1995).

[55] R. Barnett, E. Demler, and E. Kaxiras, "Electron-phonon interaction in ultrasmall-radius carbon nanotubes," Physical Review B **71** (3), 035429 (2005).

[56] D. Connetable, G. M. Rignanese, J. C. Charlier, and X. Blase, "Room temperature Peierls distortion in small diameter nanotubes," Physical Review Letters **94** (1), 015503 (2005).

[57] J. Gonzalez, "Microscopic model of superconductivity in carbon nanotubes," Physical Review Letters **88** (7), 076403 (2002).

[58] N. Murata, J. Haruyama, J. Reppert, A. M. Rao, T. Koretsune, S. Saito, M. Matsudaira, and Y. Yagi, "Superconductivity in thin films of boron-doped carbon nanotubes," Physical Review Letters **101** (2), 027002 (2008).

[59] T. Koretsune and S. Saito, "Electronic structures and three-dimensional effects of boron-doped carbon nanotubes," Science and Technology of Advanced Materials **9** (4), 044203 (2008).

[60] T. Koretsune and S. Saito, "Electronic structure of boron-doped carbon nanotubes," Physical Review B **77** (16), 165417 (2008).

[61] X. Shi, J. Yang, J. R. Salvador, M. F. Chi, J. Y. Cho, H. Wang, S. Q. Bai, J. H. Yang, W. Q. Zhang, and L. D. Chen, "Multiple-Filled Skutterudites: High Thermoelectric Figure of Merit through Separately Optimizing Electrical and Thermal Transports," J. Am. Chem. Soc. **133** (20), 7837 (2011).

[62] T. C. Harman, M. P. Walsh, B. E. Laforge, and G. W. Turner, "Nanostructured

thermoelectric materials," Journal of Electronic Materials **34** (5), L19 (2005).

63 L. D. Hicks and M. S. Dresselhaus, "Thermoelectric Figure of Merit of a One-Dimensional Conductor," Phys. Rev. B **47** (24), 16631 (1993).

64 A. I. Boukai, Y. Bunimovich, J. Tahir-Kheli, J. K. Yu, W. A. Goddard, and J. R. Heath, "Silicon nanowires as efficient thermoelectric materials," Nature **451** (7175), 168 (2008).

65 Joseph P. Heremans, Bartlomiej Wiendlocha, and Audrey M. Chamoire, "Resonant levels in bulk thermoelectric semiconductors," Energy & Environmental Science **5** (2), 5510 (2012).

66 K. X. Chen, X. M. Wang, D. C. Mo, and S. S. Lyu, "Thermoelectric Properties of Transition Metal Dichalcogenides: From Monolayers to Nanotubes," J. Phys. Chem. C **119** (47), 26706 (2015).

67 R. G. Yang, G. Chen, and M. S. Dresselhaus, "Thermal conductivity of simple and tubular nanowire composites in the longitudinal direction," Phys. Rev. B **72** (12), 125418 (2005).

68 R. G. Yang, G. Chen, and M. S. Dresselhaus, "Thermal conductivity modeling of core-shell and tubular nanowires," Nano Lett. **5** (6), 1111 (2005).

69 J. Hone, I. Ellwood, M. Muno, A. Mizel, M. L. Cohen, A. Zettl, A. G. Rinzler, and R. E. Smalley, "Thermoelectric power of single-walled carbon nanotubes," Physical Review Letters **80** (5), 1042 (1998).

70 G. U. Sumanasekera, B. K. Pradhan, H. E. Romero, K. W. Adu, and P. C. Eklund, "Giant thermopower effects from molecular physisorption on carbon nanotubes," Physical Review Letters **89** (16), 166801 (2002).

71 J. Vavro, M. C. Llaguno, J. E. Fischer, S. Ramesh, R. K. Saini, L. M. Ericson, V. A. Davis, R. H. Hauge, M. Pasquali, and R. E. Smalley, "Thermoelectric power of p-doped single-wall carbon nanotubes and the role of phonon drag," Physical Review Letters **90** (6), 065503 (2003).

72 Y. Nonoguchi, K. Ohashi, R. Kanazawa, K. Ashiba, K. Hata, T. Nakagawa, C. Adachi, T. Tanase, and T. Kawai, "Systematic Conversion of Single Walled Carbon Nanotubes into n-type Thermoelectric Materials by Molecular Dopants," Scientific Reports **3**, 3344 (2013).

73 K. Yanagi, S. Kanda, Y. Oshima, Y. Kitamura, H. Kawai, T. Yamamoto, T. Takenobu, Y. Nakai, and Y. Maniwa, "Tuning of the Thermoelectric Properties of One-Dimensional Material Networks by Electric Double Layer Techniques Using Ionic Liquids," Nano Letters **14** (11), 6437 (2014).

74 Y. Oshima, Y. Kitamura, Y. Maniwa, and K. Yanagi, "Fabrication of thermoelectric

devices using precisely Fermi level-tuned semiconducting single-wall carbon nanotubes," Appl. Phys. Lett. **107** (4), 043106 (2015).

[75] T. Fujimoto and K. Awaga, "Electric-double-layer field-effect transistors with ionic liquids," Physical Chemistry Chemical Physics **15** (23), 8983 (2013).

[76] K. Ueno, H. Shimotani, H. T. Yuan, J. T. Ye, M. Kawasaki, and Y. Iwasa, "Field-Induced Superconductivity in Electric Double Layer Transistors," Journal of the Physical Society of Japan **83** (3), 032001 (2014).

[77] M. Sugahara, H. Kawai, Y. Yomogida, Y. Maniwa, S. Okada, and K. Yanagi, "Ambipolar transistors based on random networks of WS2 nanotubes," Appl. Phys. Express **9** (7), 075001 (2016).

[78] H. Kawai, S. Mitsunari, O. Ryotaro, Y. Maniwa, Y. Yomogida, and K. Yanagi, "Thermoelectric properties of WS2 nanotube networks," Applied Physics Express **10**, 015001 (2017).

[79] H. Shitomi, Ibuki, T., Matsumoto, S., Onuki, H. , "Optically Controlled Alignment of Liquid Crystal on Polyimide Films Exposed to Undulator Radiation," Jpn. J. Appl. Phys. **38** (176) (1999).

[80] H. Nakashima, Furukawa, K., Kashimura, Y., Torimitsu, K. , "Self-Assembly of Gold Nanorods Induced by Intermolecular Interactions of Surface-Anchored Lipids," Langmuir **24** (11), 5654 (2008).

[81] M. R. Falvo, G. J. Clary, R. M. Taylor, V. Chi, F. P. Brooks, S. Washburn, and R. Superfine, "Bending and buckling of carbon nanotubes under large strain," Nature **389** (6651), 582 (1997).

[82] J. P. Salvetat, J. M. Bonard, N. H. Thomson, A. J. Kulik, L. Forro, W. Benoit, and L. Zuppiroli, "Mechanical properties of carbon nanotubes," Applied Physics a-Materials Science & Processing **69** (3), 255 (1999).

[83] M. F. Yu, B. S. Files, S. Arepalli, and R. S. Ruoff, "Tensile loading of ropes of single wall carbon nanotubes and their mechanical properties," Physical Review Letters **84** (24), 5552 (2000).

[84] J. Vaillancourt, H. Y. Zhang, P. Vasinajindakaw, H. T. Xia, X. J. Lu, X. L. Han, D. C. Janzen, W. S. Shih, C. S. Jones, M. Stroder, M. Y. H. Chen, H. Subbaraman, R. T. Chen, U. Berger, and M. Renn, "All ink-jet-printed carbon nanotube thin-film transistor on a polyimide substrate with an ultrahigh operating frequency of over 5 GHz," Applied Physics Letters **93** (24), 243301 (2008).

[85] B. Chandra, H. Park, A. Maarouf, G. J. Martyna, and G. S. Tulevski, "Carbon nanotube thin film transistors on flexible substrates," Applied Physics Letters **99** (7), 072110 (2011).

[86] J. S. Shi, C. X. Guo, M. B. Chan-Park, and C. M. Li, "All-Printed Carbon Nanotube finFETs on Plastic Substrates for High-Performance Flexible Electronics," Advanced Materials **24** (3), 358 (2012).

[87] Chuan Wang, Jun-Chau Chien, Kuniharu Takei, Toshitake Takahashi, Junghyo Nah, Ali M. Niknejad, and Ali Javey, "Extremely Bendable, High-Performance Integrated Circuits Using Semiconducting Carbon Nanotube Networks for Digital, Analog, and Radio-Frequency Applications," Nano Letters **12** (3), 1527 (2012).

[88] F. Xu, M. Y. Wu, N. S. Safron, S. S. Roy, R. M. Jacobberger, D. J. Bindl, J. H. Seo, T. H. Chang, Z. Q. Ma, and M. S. Arnold, "Highly Stretchable Carbon Nanotube Transistors with Ion Gel Gate Dielectrics," Nano Letters **14** (2), 682 (2014).

[89] K. Yanagi, R. Moriya, Y. Yomogida, T. Takenobu, Y. Naitoh, T. Ishida, H. Kataura, K. Matsuda, and Y. Maniwa, "Electrochromic Carbon Electrodes: Controllable Visible Color Changes in Metallic Single-Wall Carbon Nanotubes," Advanced Materials **23** (25), 2811 (2011).

[90] Y. Nakai, Honda, K., Yanagi, K., Kataura, H., Kato, T., Yamamoto, T. and Maniwa, Y., "Giant Seebeck coefficient in semiconducting single-wall carbon nanotube film," Appl. Phys. Express **7** (025103) (2014).

[91] P. C. Collins, M. S. Arnold, and P. Avouris, "Engineering carbon nanotubes and nanotube circuits using electrical breakdown," Science **292** (5517), 706 (2001).

[92] P. G. Collins, M. Hersam, M. Arnold, R. Martel, and P. Avouris, "Current saturation and electrical breakdown in multiwalled carbon nanotubes," Physical Review Letters **86** (14), 3128 (2001).

[93] M. Zheng, A. Jagota, M. S. Strano, A. P. Santos, P. Barone, S. G. Chou, B. A. Diner, M. S. Dresselhaus, R. S. McLean, G. B. Onoa, G. G. Samsonidze, E. D. Semke, M. Usrey, and D. J. Walls, "Structure-based carbon nanotube sorting by sequence-dependent DNA assembly," Science **302** (5650), 1545 (2003).

[94] X. Y. Huang, R. S. McLean, and M. Zheng, "High-resolution length sorting and purification of DNA-wrapped carbon nanotubes by size-exclusion chromatography," Analytical Chemistry **77** (19), 6225 (2005).

[95] X. M. Tu, S. Manohar, A. Jagota, and M. Zheng, "DNA sequence motifs for structure-specific recognition and separation of carbon nanotubes," Nature **460** (7252), 250 (2009).

[96] P. Beecher, P. Servati, A. Rozhin, A. Colli, V. Scardaci, S. Pisana, T. Hasan, A. J. Flewitt, J. Robertson, G. W. Hsieh, F. M. Li, A. Nathan, A. C. Ferrari, and W. I. Milne, "Ink-jet printing of carbon nanotube thin film transistors," Journal of Applied Physics **102** (4), 043710 (2007).

[97] J. Hone, M. C. Llaguno, N. M. Nemes, A. T. Johnson, J. E. Fischer, D. A. Walters, M. J. Casavant, J. Schmidt, and R. E. Smalley, "Electrical and thermal transport properties of magnetically aligned single walled carbon nanotube films," Applied Physics Letters **77** (5), 666 (2000).

[98] B. W. Smith, Z. Benes, D. E. Luzzi, J. E. Fischer, D. A. Walters, M. J. Casavant, J. Schmidt, and R. E. Smalley, "Structural anisotropy of magnetically aligned single wall carbon nanotube films," Applied Physics Letters **77** (5), 663 (2000).

[99] X. Q. Chen, T. Saito, H. Yamada, and K. Matsushige, "Aligning single-wall carbon nanotubes with an alternating-current electric field," Applied Physics Letters **78** (23), 3714 (2001).

[100] C. Park, J. Wilkinson, S. Banda, Z. Ounaies, K. E. Wise, G. Sauti, P. T. Lillehei, and J. S. Harrison, "Aligned single-wall carbon nanotube polymer composites using an electric field," Journal of Polymer Science Part B-Polymer Physics **44** (12), 1751 (2006).

[101] M. C. LeMieux, M. Roberts, S. Barman, Y. W. Jin, J. M. Kim, and Z. N. Bao, "Self-sorted, aligned nanotube networks for thin-film transistors," Science **321** (5885), 101 (2008).

[102] Qing Cao, Shu-jen Han, George S. Tulevski, Yu Zhu, Darsen D. Lu, and Wilfried Haensch, "Arrays of single-walled carbon nanotubes with full surface coverage for high-performance electronics," Nature Nanotechnology **8** (3), 180 (2013).

[103] X. Li, Zhang, L., Wang, X., Shimoyama, I., Sun, X., Seo, W. and Dai, H. , "Langmuir−Blodgett Assembly of Densely Aligned Single-Walled Carbon Nanotubes from Bulk Materials," J. Am. Chem. Sci. **129** (16), 4890–4891 (2007).

[104] H. Park, Afzali, A., Han, S., Tulevski, G., Franklin, A., Tersoff, J., Hannon, J. & Haensch, W. , "High-density integration of carbon nanotubes via chemical self-assembly," Nat. Nanotech. **7**, 787 (2012).

[105] Y. Takagi, Y. Nobusa, S. Gocho, H. Kudou, K. Yanagi, H. Kataura, and T. Takenobu, "Inkjet printing of aligned single-walled carbon-nanotube thin films," Applied Physics Letters **102** (14), 143107 (2013).

[106] L. Jaber-Ansari, M. G. Hahm, S. Somu, Y. E. Sanz, A. Busnaina, and Y. J. Jung, "Mechanism of Very Large Scale Assembly of SWNTs in Template Guided Fluidic Assembly Process," Journal of the American Chemical Society **131** (2), 804 (2009).

[107] H. Kawai, Hasegawa, K., Nakatsu, T., Naitoh, Y., Takagi, Y., Wada, Y., Takenobu, T. and Yanagi, K. , "String like Assembly of Aligned Single-Wall Carbon Nanotubes in a Single-Chiral State," Appl. Phys. Express **6** (6), 065103 (2013).

[108] L. Ren, C. L. Pint, L. G. Booshenri, W. D. Rice, X. F. Wang, D. J. Hilton, K. Takeya, I.

Kawayama, M. Tonouchi, R. H. Hauge, and J. Kono, "Carbon Nanotube Terahertz Polarizer," Nano Letters **9** (7), 2610 (2009).

109 Q. Cao, Han, S., Tulevski, G. , Zhu, Y., Lu, D. & Haensch, W. , "Arrays of single-walled carbon nanotubes with full surface coverage for high-performance electronics," Nat. Nanotech. **8**, 180 (2013).

110 Z. and Brus Yu, L. , "Rayleigh and Raman Scattering from Individual Carbon Nanotube Bundles," J. Phys. Chem. B **105** (6), 1123 (2001).

111 J. E. Fischer, H. Dai, A. Thess, R. Lee, N. M. Hanjani, D. L. Dehaas, and R. E. Smalley, "Metallic resistivity in crystalline ropes of single-wall carbon nanotubes," Physical Review B **55** (8), R4921 (1997).

112 A.L. Efros B.I. Shklovskii, *Electronic properties of doped semiconductors*. (1984).

113 N. Mott, *Conduction in non-crystalline materials*. (Clarendon Press, 1987).

114 J. P. Small, K. M. Perez, and P. Kim, "Modulation of thermoelectric power of individual carbon nanotubes," Physical Review Letters **91** (25), 256801 (2003).

115 Y. Nakai, K. Honda, K. Yanagi, H. Kataura, T. Kato, T. Yamamoto, and Y. Maniwa, "Giant Seebeck coefficient in semiconducting single-wall carbon nanotube film," Applied Physics Express **7** (2), 025103 (2014).

116 N. Zibouche, A. Kuc, and T. Heine, "From layers to nanotubes: Transition metal disulfides TMS2," Eur. Phys. J. B **85** (1), 49 (2012).

117 C. Y. Zhang, Z. Y. Ning, Y. Liu, T. T. Xu, Y. Guo, A. Zak, Z. Y. Zhang, S. Wang, R. Tenne, and Q. Chen, "Electrical transport properties of individual WS2 nanotubes and their dependence on water and oxygen absorption," Appl. Phys. Lett. **101** (11), 113112 (2012).

118 R. Levi, O. Bitton, G. Leitus, R. Tenne, and E. Joselevich, "Field-Effect Transistors Based on WS2 Nanotubes with High Current-Carrying Capacity," Nano Lett. **13** (8), 3736 (2013).

119 C. Y. Zhang, S. Wang, L. Yang, Y. Liu, T. T. Xu, Z. Y. Ning, A. Zak, Z. Y. Zhang, R. Tenne, and Q. Chen, "High-performance photodetectors for visible and near-infrared lights based on individual WS2 nanotubes," Appl. Phys. Lett. **100** (24), 243101 (2012).

120 Y. Q. Zhu, T. Sekine, Y. H. Li, M. W. Fay, Y. M. Zhao, C. H. P. Poa, W. X. Wang, M. J. Roe, P. D. Brown, N. Fleischer, and R. Tenne, "Shock-absorbing and failure mechanisms of WS2 and MoS2 nanoparticles with fullerene-like structures under shock wave pressure," J. Am. Chem. Soc. **127** (46), 16263 (2005).

121 E. Kalfon-Cohen, O. Goldbart, R. Schreiber, S. R. Cohen, D. Barlam, T. Lorenz, J. O. Joswig, and G. Seifert, "Experimental, finite element, and density-functional

theory study of inorganic nanotube compression," Appl. Phys. Lett. **98** (8), 081908 (2011).

[122] R. Rosentsveig, A. Margolin, Y. Feldman, R. Popovitz-Biro, and R. Tenne, "Bundles and foils of WS2 nanotubes," Appl. Phys. A **74** (3), 367 (2002).

[123] R. Rosentsveig, A. Margolin, Y. Feldman, R. Popovitz-Biro, and R. Tenne, "WS2 nanotube bundles and foils," Chem. Mater. **14** (2), 471 (2002).

[124] T. Ozel, A. Gaur, J. A. Rogers, and M. Shim, "Polymer electrolyte gating of carbon nanotube network transistors," Nano Letters **5** (5), 905 (2005).

[125] Hidekazu Shimotani, Satoshi Tsuda, Hongtao Yuan, Yohei Yomogida, Rieko Moriya, Taishi Takenobu, Kazuhiro Yanagi, and Yoshihiro Iwasa, "Continuous Band-Filling Control and One-Dimensional Transport in Metallic and Semiconducting Carbon Nanotube Tangled Films," Advanced Functional Materials **24** (22), 3305 (2014).

[126] F. Jakubka, C. Backes, F. Gannott, U. Mundloch, F. Hauke, A. Hirsch, and J. Zaumseil, "Mapping Charge Transport by Electroluminescence in Chirality-Selected Carbon Nanotube Networks," Acs Nano **7** (8), 7428 (2013).

[127] K. Yanagi, Y. Miyata, and H. Kataura, "Optical and Conductive Characteristics of Metallic Single-Wall Carbon Nanotubes with Three Basic Colors; Cyan, Magenta, and Yellow," Applied Physics Express **1**, 034003 (2008).

[128] K. Yanagi, H. Udoguchi, S. Sagitani, Y. Oshima, T. Takenobu, H. Kataura, T. Ishida, K. Matsuda, and Y. Maniwa, "Transport Mechanisms in Metallic and Semiconducting Single-Wall Carbon Nanotube Networks," ACS Nano **4**, 4027 (2010).

[129] M. Arnold, A. Green, J. Hulvat, S. Stupp, and M. Hersam, "Sorting carbon nanotubes by electronic structure using density differentiation," Nature Nanotechnology **1**, 60 (2006).

[130] D. Hayashi, T. Ueda, Y. Nakai, H. Kyakuno, Y. Miyata, T. Yamamoto, T. Saito, K. Hata, and Y. Maniwa, "Thermoelectric properties of single-wall carbon nanotube films: Effects of diameter and wet environment," Applied Physics Express **9** (2), 025102 (2016).

[131] S. Ilani, L. A. K. Donev, M. Kindermann, and P. L. McEuen, "Measurement of the quantum capacitance of interacting electrons in carbon nanotubes," Nature Phys. **2** (10), 687 (2006).

[132] T. Igarashi, H. Kawai, K. Yanagi, N. T. Cuong, S. Okada, and T. Pichler, "Tuning Localized Transverse Surface Plasmon Resonance in Electricity-Selected Single-Wall Carbon Nanotubes by Electrochemical Doping," Phys. Rev. Lett. **114** (17), 176807 (2015).

[133] J. Pu, K. Kanahashi, N. T. Cuong, C. H. Chen, L. J. Li, S. Okada, H. Ohta, and T. Takenobu, "Enhanced thermoelectric power in two-dimensional transition metal dichalcogenide monolayers," Phys. Rev. B **94** (1), 014312 (2016).

[134] D. Braga, I. G. Lezama, H. Berger, and A. F. Morpurgo, "Quantitative Determination of the Band Gap of WS2 with Ambipolar Ionic Liquid-Gated Transistors," Nano Lett. **12** (10), 5218 (2012).

[135] K. P. Pernstich, S. Haas, D. Oberhoff, C. Goldmann, D. J. Gundlach, B. Batlogg, A. N. Rashid, and G. Schitter, "Threshold voltage shift in organic field effect transistors by dipole monolayers on the gate insulator," J. Appl. Phys. **96** (11), 6431 (2004).

[136] C. S. S. Sangeeth, P. Stadler, S. Schaur, N. S. Sariciftci, and R. Menon, "Interfaces and traps in pentacene field-effect transistor," J. Appl. Phys. **108** (11), 113703 (2010).

[137] W. Zhou, X. L. Zou, S. Najmaei, Z. Liu, Y. M. Shi, J. Kong, J. Lou, P. M. Ajayan, B. I. Yakobson, and J. C. Idrobo, "Intrinsic Structural Defects in Monolayer Molybdenum Disulfide," Nano Lett. **13** (6), 2615 (2013).

[138] S. K. Srivastava and B. N. Avasthi, "Synthesis and Characterization of Indium Intercalation Compounds of Tungsten Disulfide - Inxws2 (0-Less-Than-or-Equal-to-1)," Synth. Met. **10** (3), 213 (1985).

[139] G. K. Solanki, D. N. Gujarathi, M. P. Deshpande, D. Lakshminarayana, and M. K. Agarwal, "Transport property measurements in tungsten sulphoselenide single crystals grown by a CVT technique," Cryst. Res. Technol. **43** (2), 179 (2008).

[140] A. Pisoni, J. Jacimovic, R. Gaal, B. Nafradi, H. Berger, Z. Revay, and L. Forro, "Anisotropic transport properties of tungsten disulfide," Scr. Mater. **114**, 48 (2016).

[141] J. Y. Kim, S. M. Choi, W. S. Seo, and W. S. Cho, "Thermal and Electronic Properties of Exfoliated Metal Chalcogenides," Bull. Korean Chem. Soc. **31** (11), 3225 (2010).

[142] J. H. Kim, J. Y. Choi, J. M. Bae, M. Y. Kim, and T. S. Oh, "Thermoelectric Characteristics of n-Type Bi2Te3 and p-Type Sb2Te3 Thin Films Prepared by Co-Evaporation and Annealing for Thermopile Sensor Applications," Materials Transactions **54** (4), 618 (2013).

[143] W. B. Zhou, Q. X. Fan, Q. Zhang, K. W. Li, L. Cai, X. G. Gu, F. Yang, N. Zhang, Z. J. Xiao, H. L. Chen, S. Q. Xiao, Y. C. Wang, H. P. Liu, W. Y. Zhou, and S. S. Xie, "Ultrahigh-Power-Factor Carbon Nanotubes and an Ingenious Strategy for Thermoelectric Performance Evaluation," Small **12** (25), 3407 (2016).

[144] Z. Yao, C. L. Kane, and C. Dekker, "High-field electrical transport in single-wall carbon nanotubes," Physical Review Letters **84** (13), 2941 (2000).

145 S. H. Jin, S. N. Dunham, J. Z. Song, X. Xie, J. H. Kim, C. F. Lu, A. Islam, F. Du, J. Kim, J. Felts, Y. H. Li, F. Xiong, M. A. Wahab, M. Menon, E. Cho, K. L. Grosse, D. J. Lee, H. U. Chung, E. Pop, M. A. Alam, W. P. King, Y. G. Huang, and J. A. Rogers, "Using nanoscale thermocapillary flows to create arrays of purely semiconducting single-walled carbon nanotubes," Nature Nanotechnology **8** (5), 347 (2013).

146 A. E. Islam, J. A. Rogers, and M. A. Alam, "Recent Progress in Obtaining Semiconducting Single-Walled Carbon Nanotubes for Transistor Applications," Advanced Materials **27** (48), 7908 (2015).

147 J. R. Sanchez-Valencia, T. Dienel, O. Groning, I. Shorubalko, A. Mueller, M. Jansen, K. Amsharov, P. Ruffieux, and R. Fasel, "Controlled synthesis of single-chirality carbon nanotubes," Nature **512** (7512), 61 (2014).

148 A. I. Persson, Y. K. Koh, D. G. Cahill, L. Samuelson, and H. Linke, "Thermal Conductance of InAs Nanowire Composites," Nano Letters **9** (12), 4484 (2009).

149 A. Mavrokefalos, A. L. Moore, M. T. Pettes, L. Shi, W. Wang, and X. G. Li, "Thermoelectric and structural characterizations of individual electrodeposited bismuth telluride nanowires," Journal of Applied Physics **105** (10), 104318 (2009).

150 F. Zhou, J. H. Seol, A. L. Moore, L. Shi, Q. L. Ye, and R. Scheffler, "One-dimensional electron transport and thermopower in an individual InSb nanowire," Journal of Physics-Condensed Matter **18** (42), 9651 (2006).

151 X. W. He, W. L. Gao, L. J. Xie, B. Li, Q. Zhang, S. D. Lei, J. M. Robinson, E. H. Haroz, S. K. Doorn, W. P. Wang, R. Vajtai, P. M. Ajayan, W. W. Adams, R. H. Hauge, and J. Kono, "Wafer-scale monodomain films of spontaneously aligned single-walled carbon nanotubes," Nature Nanotechnology **11** (7), 633 (2016).

152 J. P. Heremans, M. S. Dresselhaus, L. E. Bell, and D. T. Morelli, "When thermoelectrics reached the nanoscale," Nature Nanotechnology **8** (7), 471 (2013).

153 M. Nakano, K. Shibuya, D. Okuyama, T. Hatano, S. Ono, M. Kawasaki, Y. Iwasa, and Y. Tokura, "Collective bulk carrier delocalization driven by electrostatic surface charge accumulation," Nature **487** (7408), 459 (2012).

154 J. T. Ye, S. Inoue, K. Kobayashi, Y. Kasahara, H. T. Yuan, H. Shimotani, and Y. Iwasa, "Liquid-gated interface superconductivity on an atomically flat film," Nature Materials **9** (2), 125 (2010).

155 K. Ueno, S. Nakamura, H. Shimotani, H. T. Yuan, N. Kimura, T. Nojima, H. Aoki, Y. Iwasa, and M. Kawasaki, "Discovery of superconductivity in KTaO3 by electrostatic carrier doping," Nature Nanotechnology **6** (7), 408 (2011).

156 J. T. Ye, Y. J. Zhang, R. Akashi, M. S. Bahramy, R. Arita, and Y. Iwasa, "Superconducting Dome in a Gate-Tuned Band Insulator," Science **338** (6111), 1193

(2012).

157 M. Yoshida, T. Iizuka, Y. Saito, M. Onga, R. Suzuki, Y. J. Zhang, Y. Iwasa, and S. Shimizu, "Gate-Optimized Thermoelectric Power Factor in Ultrathin WSe2 Single Crystals," Nano Lett. **16** (3), 2061 (2016).